POLITECNICO DI TORINO

Dottorato di Ricerca in Progettazione Meccanica e
Costruzione di Macchine
XX Ciclo
Settore Scientifico Disciplinare ING/IND 14

Alessandro Dallocchio

TESI DI DOTTORATO

STUDY OF THERMO-MECHANICAL EFFECTS INDUCED IN SOLIDS BY HIGH ENERGY PARTICLE BEAMS: ANALYTICAL AND NUMERICAL METHODS

Tutor: Prof. Giovanni Belingardi

Supervisor: Dr. Tadeusz Kurtyka
Alessandro Bertarelli

April 2008

A mamma e papà e a Serena

Acknowledgements

Acknowledgments require a feeling that I am able to convey only in my mother tongue…quindi:
Desidero ringraziare in primo luogo l'Ing. Alessandro Bertarelli che ha supervisionato la mia attività di ricerca al CERN, a lui devo gran parte di ciò che ho imparato durante la mia esperienza come ricercatore ed ingegnere. Grazie al Dr. Tadeusz Kurtyka per i preziosi consigli e l'esperienza messami a disposizione. Ringrazio il Prof. Belingardi, che ha seguito il mio percorso di formazione fino al dottorato ed il Dr. Peroni che mi ha trasmesso la passione per la ricerca, grazie a lui ho intrapreso questa straordinaria esperienza al CERN. Importante è stato l'esempio di Roger Perret e di Luca Gentini, che mi hanno insegnato la meccanica...quella vera, quella dei progettisti!
Ringrazio mia madre, mio padre e Serena, che mi hanno seguito e supportato in questa avventura, perdonando la mia lontananza. A loro devo il raggiungimento di questo importante obiettivo.
Vorrei abbracciare tutti gli "amici miei": Andrea, Timothy, Bocca, Dany, Chicco, Gigi, Page, Cri, Lello e Piotta per la straordinaria amicizia che ci lega ormai da piu' di vent'anni.
Per finire, un ringraziamento particolare va ai miei "nuovi amici", persone speciali, che mi hanno accolto a Ginevra facendomi sentire come a casa; è stato un onore ed un privilegio condividere con voi questi quattro anni: Dr. Bellesia, Dr. Barbero Soto, Dr. Laface, Dr. Sterbini, Dr. Bordini, Dr. Previtali, Dr. Vergara Fernandez, Dr. Roncarolo, Dr. Regis, Dr. Redaelli, Dr. Pieloni.

Contents

Part I

INTRODUCTION

Chapter 1

Introduction

The understanding of the infinitely big universe depends indissolubly on the investigation of the infinitely small sub-atomic components of matter and on their fundamental interaction forces (electromagnetic, gravitational, strong nuclear and weak nuclear). Particle accelerators [1.1] act as microscopes for such a complex research; these large machines accelerate charged elementary particles (electrons, protons or ionized atoms) to high kinetic energies.

A high energy particle beam can be brought into collision against a fixed target or against another beam and from this encounter a multitude of short life sub-atomic particles is originated. The investigation of matter in these extreme conditions can be compared with the status of the Universe in the first moments after the so-called `Big Bang'. The higher the energy of the colliding beams and the event rate, the wider the spectrum of the generable sub-atomic particles.

It is in this perspective that the project of building the Large Hadron Collider (LHC) [1.2] at the European Organization for Nuclear Research (CERN, Geneva) was approved in December 1994 and in August 2008 the machine will be finally "turned on". The LHC [1.3] is a circular accelerator with a 26.659 km circumference situated at the border between Switzerland and France at an average depth of 100 m underground. This machine will mainly provide proton-proton collisions with a centre-of-mass energy of 14 TeV. The particles will be pre-accelerated by the injection chain [1.4] constituted by a linear accelerator (LINAC-2) and two circular machines: the Proton Synchrotron (PS) and the Super Proton Synchrotron (SPS). Two 450 GeV beams of $3.2 \cdot 10^{14}$ protons will be finally injected in the LHC and accelerated up-to 7 TeV each. This corresponds to a stored energy of 360 MJ in each beam, a factor 200 above TEVATRON (USA) and HERA (Germany), present state of the art in particle accelerator technology.

In the LHC the hadronic particle beams will be accelerated inside ultra-high vacuum pipes till relativistic velocity thanks to radio-frequency accelerating cavities. High energy particles will be kept in circular orbit by superconducting magnets inducing a Lorentz force on the charged particles. The collisions between particle beams will occur in four interaction points where the detectors are placed: ATLAS [1.5], CMS [1.6], ALICE [1.7] and LHC-b [1.8]. The detectors recognize and measure properties of sub-atomic particles produced during the collisions.

1.1 Problem definition

Requirements of modern nuclear physics entail big efforts in the field of particle accelerator technology in order to build powerful machines providing particle beams at higher and higher energies; in this context, the Large Hadron Collider represents the future for particle physics. The LHC stores 360 MJ for each circulating beam; this large amount of energy is potentially destructive for accelerator equipments having direct interaction with particles; the need to handle high thermal loads bestows strategic importance to the study of thermo-mechanical problems in accelerator devices.

Interaction between high energy particle beams and solids can be considered from a structural point of view as a volumic energy deposition inducing a non uniform temperature increase. Different thermal loads must be taken into account depending on the interaction conditions: in normal situations, a continuous interaction provokes a constant energy-rate deposition over a long period (from some seconds up to few hours). Otherwise, in case of abnormal beam impacts, energy is rapidly deposited in time-scales of the order of microseconds or nanoseconds. This load condition typically entails a dynamic response of the structure. The resulting thermal stresses and deformations may affect the integrity or the proper functionality of the hit equipments (see Figure 1.1 and Figure 1.2).

High energetic beams may interact with several components present in particle accelerators, the most critical, from the thermo-structural point of view, are the following:

- *Beam dumps*. These are structures, usually of large dimensions, used to stop a particle beam and absorb its energy when it is necessary to abort it.

- *Windows*. These are thin plate structures that physically separate two different environments traversed by the beam.
- *Beam targets*. These are beam-like structures used to produce secondary particles from the interaction of a primary beam with the material of the target.
- *Collimators*. These devices are essential for the beam cleaning: in fact they are used to intercept those particles unavoidably escaping from the correct trajectory during normal operations. Moreover, collimators play the role of machine protection, to catch anomalous particle losses following equipment failures or wrong operation of the machine. In case of LHC, given the high energy stored, the collimation system is of crucial importance for the protection of all other equipments; LHC collimators are the closest elements to the particle beam, thus an in-depth thermo-mechanical analysis is strongly necessary.

Figure 1.1: CERN archive picture. Beryllium target rod bent and broken under the effect of particle beam impact.

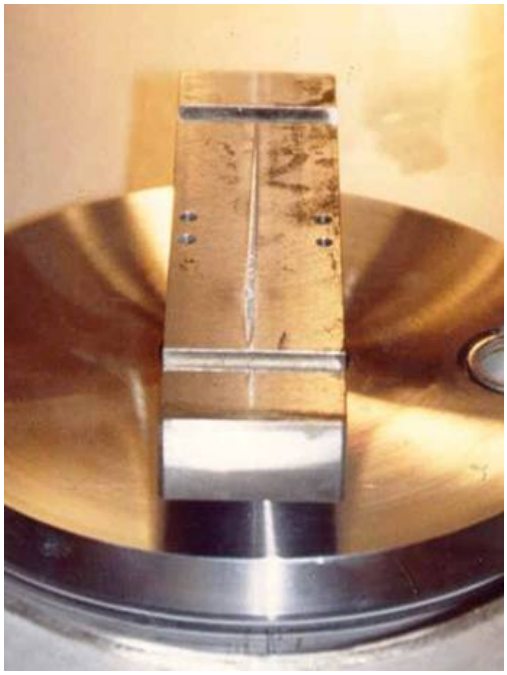

Figure 1.2: CERN archive picture. Tungsten collimator melted by particle beam. The resulting longitudinal groove can be observed.

1.2 Aim of the work and tools

The aim of this work is the study of thermo-mechanical effects induced in solids by high energy particle beams. These phenomena can be classified depending on different energy deposition patterns, which in turn are determined by the interaction parameters of the beam. In case of particle beam impact, the rapid energy deposition provokes a dynamic response of the structure entailing thermal stress waves and thermally induced vibrations or even the failure of the component; in case of steady-state or slow transient thermal loads, thermal stresses and deformations take place but no dynamic response can usually be observed.

Development of facilities devoted to the experimental test of accelerator equipments in real working conditions presents several technical difficulties and high cost; the importance of developing reliable methods and accurate models that could be efficiently applied during the design phase of the most critical particle accelerator devices is therefore evident.

From a methodological point of view, thermo-mechanical problems have been studied in this thesis with two different approaches: analytical and numerical. Analytical methods allowed to build a good theoretical background in order to gain thorough understanding of dynamic thermo-structural phenomena occurring in case of

particle beam impacts. Numerical approach, based on the Finite Element Method (FEM), is essential for the study of complex structures including multi-components systems with contact interfaces as well as material non-linearities.

An important aspect that has been treated in this thesis is the comparison between results obtained from analytical and numerical analyses with experimental measurements performed at CERN; this led to the validation of the developed methods ensuring a good level of confidence in the results obtained.

1.3 Contribution of the work

As said above, the work carried out in this thesis was strongly motivated by the need of building a systematic approach to the analysis of thermo-mechanical phenomena induced in solids by high energy particle beams. It is believed that the following results of the thesis contribute to the development of this research field:

- Starting with the analytical approach, the problem of rapid internal heating of beam-like structures, provoked by particle beam impacts, was completely solved. Effective solutions for the temperature field, quasi-static and dynamic thermal stresses were obtained.
- Dynamic structural response given by the analytical model were compared with experimental measurements; results are in very good agreement confirming the validity of the proposed solutions.
- Fundamental parameters governing the problem of thermally induced vibrations were clearly identified. This allowed a precise classification of thermal loads into quasi-static and dynamic depending on the response of the structure.
- Thermo-mechanical studies were extended to more complex structures by means of numerical approach based on the Finite Element Method. The results achieved with the analytical models were used as reference solutions to qualify numerical tools; several numerical algorithms (both implicit and explicit) were considered: the commercial implicit code ANSYS was found compliant with the needs of this work.

- Several FEM models have been implemented leading to a systematic approach to the problem. Steady-state and slow transient thermal loads as well as particle beam impacts were considered.
- Numerical results have been successfully validated by experimental tests.

This research work provides efficient tools that can be used in the design phase of accelerator devices critically exposed to particle beam interaction. Some results presented in this thesis have been published in a journal article [1.9] or in conference proceedings on particle accelerators and structural mechanics (see [1.10], [1.11] and [1.12]).

1.4 Contents of the thesis

The main results of the thesis listed in the previous paragraph, are now discussed in a more detailed way.

In order to develop analytical solutions for the dynamic thermo-mechanical response of rapidly heated structures, this research work started from the theoretical study of thermo-elasticity. It was demonstrated that in case of particle beam impacts, under some simplifying assumptions, thermal and structural analyses can be separated. Thermal problem was solved for structures of simple geometry like beams with circular and rectangular cross-section: once the heat load is known, temperature distribution as a function of time can be evaluated solving the heat conduction equation. The analytical model for thermal analysis was also extended to the case of slow energy deposition.

Dynamic structural response provoked by particle beam impact was studied in case of beam-like structures considering an isotropic material within its linear elastic domain: results of thermal analyses were used as input loads to evaluate quasi-static thermal stresses; from these, with an original approach, dynamic thermal stresses and thermally induced vibrations were obtained. Analytical models were directly applied to the thermo-structural analysis of beam targets for the CNGS experiment [1.13] while thermal analysis was carried out for an SPS collimator [1.14].

The need of extending thermo-mechanical analysis to more complex structures gave the impulse for the development of a numerical approach based on the Finite Element Method. Through the implementation of FEM models the study was widened

to multi-component systems with complex geometry and contact interfaces; material non-linearity was also included in the analyses. Numerical models allow to simulate several conditions of interaction with particle beams. In case of steady-state or slow transient energy deposition, the attention focused on thermo-mechanical contact algorithm governing the heat flow throughout contact interfaces; this situation entails a coupled thermal/structural analysis. In case of particle beam impact, thermal and structural problems can be separated and sequentially solved: thermally induced vibrations have been studied in the elastic-plastic domain of materials allowing to evaluate potential permanent damages provoked by thermal shocks.

Numerical FEM approach found direct application in the frame of the LHC collimation project; as mentioned above, LHC collimators are critically exposed to the effects of particle beams, thus an in dept thermo-mechanical analysis was carried out on these structures.

Finally, an important aspect presented in this thesis is the experimental validation of the analytical and numerical methods developed. Results of analytical calculations performed for the beam targets of the CNGS experiment were compared with experimental measurements carried out in CERN laboratories (see [1.15]): thermally induced flexural vibrations provoked by particle beam impacts and measured with a Laser Doppler Vibrometer are in very good agreement with the results obtained with the analytical approach. The same procedure was used for the LHC collimator installed in the SPS ring and submitted to several thermal shocks: the experimental measurements confirmed the validity of the numerical models.

1.5 Structure of the thesis

The thesis is organized in three parts. The first part includes the introductory Chapter 1 that presents some aspects of particle accelerators technology and introduces the subject of the thesis.

The second part focuses on the analytical method developed: Chapter 2 deals with the analytical solution of the thermal problems, while Chapter 3 is dedicated to the structural analysis of beam-like structures in case of particle beam impact including the experimental validation of the analytical solutions.

The third part of the thesis describes the numerical approach used to perform thermo-mechanical studies on complex structures. Numerical methods are mainly

presented through the analysis performed on the LHC collimators. Chapter 4 describes the LHC collimation system focusing on the mechanical design and functional requirements of the collimators. In the 5th chapter, the FEM approach developed to describe thermo-mechanical effects provoked by particle beams in case of steady–state or slow transient energy deposition is discussed. Chapter 6 deals with the numerical method applied to the case of particle beam impact. Comparison with experimental measurements confirmed the numerical results.

References

[1.1] H. Wiedemann, Particle Accelerator Physics I, Springer, Berlin,1993.

[1.2] The Large Hadron Collider, Conceptual design, CERN/AC/95-05, October 1995.

[1.3] LHC Design Report, Vol. I, The LHC Main Ring, CERN Editorial Board, 2004

[1.4] LHC Design Report, Vol. III, The LHC Injector Chain, CERN Editorial Board, 2004.

[1.5] ATLAS Detector and Physics Performance, Technical Design Report, CERN/LHCC/99-14, 1999.

[1.6] CMS Physics Technical Design Report, Volume 1: Detector Performance and Software, CERN/LHCC/06-14, 2006.

[1.7] ALICE Technical Design Report, CERN/LHCC/01-021, 2001.

[1.8] LHCb Technical Design Report, CERN/LHCC/00-007, 2000.

[1.9] A. Bertarelli, A. Dallocchio, T. Kurtyka, Thermally Induced Vibrations of Beams: Longitudinal and Flexural Behaviour, ASME Journal of Applied Mechanics - Accepted for publication, 2007

[1.10] A. Dallocchio et al., A New Analytical Method to Evaluate Transient Thermal Stresses in Cylindrical Rods Hit by Proton Beams, Proceeding of the 10th European Particle Accelerator Conference EPAC06, Edinburgh 2006, Scotland UK

[1.11] A. Dallocchio et al., Analisi Termo-Meccanica agli Elementi Finiti di una Struttura Investita da Fasci di Particelle ad Alta Energia, (Proceedings of the 34th Conference of Italian Association for Strength Analysis - AIAS 2005, Milano)

[1.12] A. Bertarelli, A. Dallocchio et al., Permanent Deformation of the LHC Collimator Jaws Induced by Shock Beam Impact: an Analytical and Numerical Interpretation", Proceeding of the 10th European Particle Accelerator Conference EPAC06, Edinburgh 2006, Scotland UK

[1.13] K. Elsener, 2000, General Description of the CERN Project for a Neutrino Beam to Gran Sasso (CNGS), CERN AC note 2000-03, CERN, Geneva.

[1.14] S. Gilardoni, A. Dallocchio, et al., Splitter Losses in the SPS, Proceedings of the APC meeting, 24th August 2006, CERN, Geneva

[1.15] R. Wilfinger, 2005, Proton-Induced Thermal Stress-wave Measurements for ISOLDE and CNGS, PhD Thesis, Vienna University of Technology, Atominstitut of the Austrian Universities, Vienna, and CERN, Geneva

Part II

ANALYTICAL METHODS

Chapter 2

Thermal analysis: an analytical method

2.1 Introduction

Complex phenomena resulting by the interaction between high energy particle beams and solids are studied in the domain of physics of collisions (see [2.1] and [2.2]); in the context of this dissertation, the interest is limited only to thermo-mechanical effects.

High energy particles, interacting with nuclei of materials, loose their energy that is deposited on the hit structure; the evaluation of thermal loads is usually performed via statistical codes based on the Monte-Carlo method. The most used code, written by CERN physicists, is called FLUKA (see [2.1] and [2.2]); the energy deposition maps obtained from this type of simulation are generally used as input for thermo-structural studies.

Considering simple structures like beams with rectangular and circular cross-sections, it was observed that the energy deposited by particle beams is usually distributed over the cross-section according to a Gaussian function; this observation makes possible to define the heat loads in an analytical way.

Once thermal loads are known, the aim of thermal analysis is the evaluation of temperature field as a function of time; the problem was solved with an analytical approach for circular and rectangular domains by means of Fourier-Bessel and Fourier expansions. The model was developed considering the case of particle beam impact: this situation entails a rapid energy deposition (microseconds or nanoseconds) so that heat diffusion could be neglected during the deposition of the energy; the solution was also extended to the case of slow energy deposition (of the order of seconds), when heat diffusion plays a relevant role, using the convolution integral to calculate the evolution of the temperature.

The developed method was directly applied to the study of beam targets for CNGS (see [2.3]) and to the thermal analysis of SPS collimator as described in [2.4].

2.2 Thermal analysis of cylindrical rods: rapid beam impact

This paragraph is dedicated to the solution of thermal problem in case of particle beam impact on cylindrical rods. The solution is valid on the assumption that the energy deposition can be reasonably considered as constant over the length of the rod (this is usually the case of beam targets). In this way the problem can be reduced to a two-dimensional analysis.

Thus, it is assumed that the deposited energy is longitudinally constant and has a Gaussian distribution over the cross-section, with standard deviation φ and eccentricity η with respect to the axis of the cylinder (see Figure 2.1); in spite of this assumption, the method is valid for any energy distribution provided it is longitudinally constant and writable as a Fourier series expansion. Thermal properties of the material were considered independent of temperature.

Heating processes due to particle beam impacts are extremely fast: thermal shock typically lasts from few nanoseconds to some microseconds. During this time τ the deposited energy can be considered as linearly growing. As shown by Kalbreier et al. [2.5], it is possible to assume that no heat diffusion occurs during the thermal shock because the characteristic thermal diffusion time t_d is much longer than the thermal shock duration τ; hence the rod, hit by the particle beam, sees a rapid temperature rise proportional to the deposited energy.

On the same ground, the system can be considered adiabatic during a typical time of several milliseconds (no heat exchange through the outer surface of the cylinder is taken into account, so the total deposited energy remains constant).

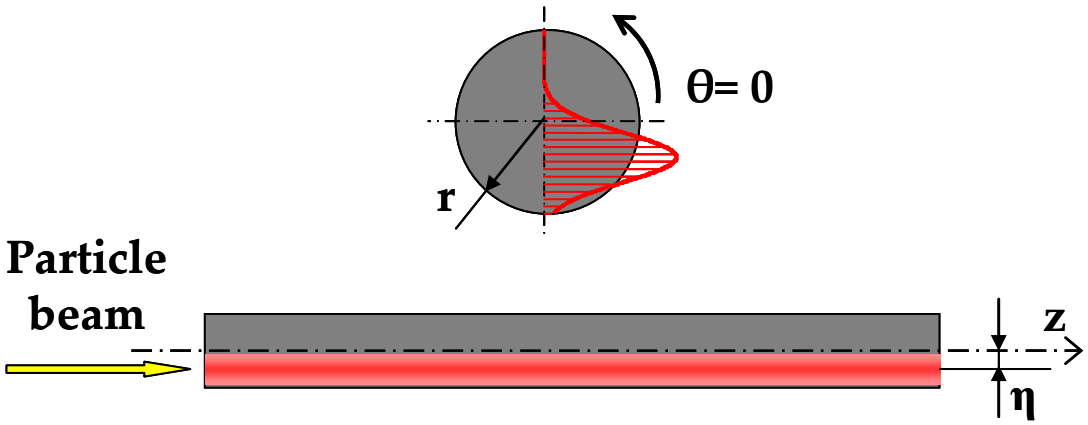

Figure 2.1: Typical energy distribution in cylindrical target rod due to proton beam impact.

2.2.1 Heat conduction equation

As already mentioned, temperature distribution can be supposed constant along the rod axis, thus reducing the analysis to a two-dimensional study. At the end of the thermal shock, when heat is no longer generated inside the cylinder, the following diffusion equation applies:

$$\frac{\partial^2 T(r,\theta,t)}{\partial r^2}+\frac{1}{r}\frac{\partial T(r,\theta,t)}{\partial r}+\frac{1}{r^2}\frac{\partial^2 T(r,\theta,t)}{\partial \theta^2}=\frac{1}{\kappa}\frac{\partial T(r,\theta,t)}{\partial t}$$

Eq. 2.1

$$\nabla^2 T(r,\theta,t)=\frac{1}{\kappa}\frac{\partial T(r,\theta,t)}{\partial t}$$

2.2.2 Initial and boundary conditions

Given that the maximum energy density U_{max} is found at $r=\eta$, $\theta=3\pi/2$ (Figure 2.1), the specific energy takes the following expression:

$$U(r,\theta)=U_{max}\cdot e^{-\frac{r^2+\eta^2+2r\eta\sin\theta}{2\varphi^2}}$$

Eq. 2.2

Having assumed that no heat diffusion occurs during the heating period, the temperature at the end of the thermal shock can be simply calculated via the following equation:

$$T_0(r,\theta) = \frac{U(r,\theta)}{c_p} \qquad \text{Eq. 2.3}$$

Since the analysis begins at $t=\tau$, Eq. 2.3 gives the initial conditions for the heat conduction equation (Eq. 2.1).

Thanks to the adiabatic hypothesis, the total energy deposited on the rod remains constant, so it is easy to calculate the final uniform temperature T_F of the cylinder at the end of the heat diffusion process:

$$T_F = \frac{\iint_{r,\theta} U(r,\theta) dr d\theta}{c_p \pi R^2} \qquad \text{Eq. 2.4}$$

The boundary condition, stemming from the adiabatic hypothesis, is given by:

$$\left.\frac{\partial T(r,\theta,t)}{\partial r}\right|_{r=R} = 0 \qquad \text{Eq. 2.5}$$

Eq. 2.5 states that the temperature gradient on the outer surface must be zero.

Initial temperature distribution given by Eq. 2.3 can be replaced by its Fourier-series expansion (n is the Fourier expansion index and a_n are the usual series coefficients):

$$T_0(r,\theta) = \sum_{n=0}^{\infty} a_n(r) H_n(\theta) \qquad \text{Eq. 2.6}$$

where $H_n(\theta) = \cos(n\theta)$ if n is even and $H_n(\theta) = \sin(n\theta)$ if n is odd.

2.2.3 Temperature distribution

We introduce non-dimensional variables for the radial coordinate $\bar{r}$, time coordinate $\bar{t}$ (note that $\bar{t} = 0$ corresponds to $t = \tau$), and temperature $\overline{T}$, as defined in the nomenclature. Adopting these coordinates, the diffusion equation (Eq. 2.1) assumes the following expression:

$$\nabla^2 \overline{T}(\bar{r},\theta,\bar{t}) = \frac{\partial \overline{T}(\bar{r},\theta,\bar{t})}{\partial \bar{t}} \qquad \text{Eq. 2.7}$$

Making use of the separation of variables method, the function $\overline{T}(\bar{r},\theta,\bar{t})$ can be reduced to the following form:

$$\overline{T}(\bar{r},\theta,\bar{t}) = \sum_n F_n(\bar{r}) \cdot G_n(\bar{t}) \cdot H_n(\theta) \qquad \text{Eq. 2.8}$$

Where H_n is the harmonic term defined in Eq. 2.6. The expression (Eq. 2.8) must satisfy the diffusion equation (Eq. 2.7). Solution of the previous equation can be obtained by means of standard methods for Partial Differential Equations and can be written in the following form:

$$\overline{T}(\bar{r},\theta,\bar{t}) = \sum_n \sum_s C_{n,s} J_n(\lambda_{n,s}\bar{r}) \cdot e^{-\lambda_{n,s}^2 \cdot \bar{t}} \cdot H_n(\theta) \qquad \text{Eq. 2.9}$$

where J_n is a Bessel function of the first kind of order n, $C_{n,s}$ are numerical coefficients obtained from the initial condition (Eq. 2.3) and $\lambda_{n,s}$ are the eigenvalues of the problem obtained from the application of the adiabatic condition (Eq. 2.5) (which can be evaluated using the approximated expressions given by Abramowitz and Stegun [2.6]).

The temperature distribution $\overline{T}$ as a function of time $\bar{t}$ for $\eta=0.6$ is shown in Figure 2.2. Results are scaled to the final uniform temperature T_F (Eq. 2.4), which is proportional to the total energy deposited on the cylinder.

Several plots are presented to describe the temperature evolution at different points of the cross-section; maximum temperature $\overline{T}\left(\eta, \frac{3\pi}{2}, 0\right)$ takes place at the centre of the Gaussian distribution, where the energy deposition has its maximum value. The heat diffusion process is virtually completed at time $\bar{t} = 1$, when temperature distribution becomes practically uniform and equal to T_F ($\overline{T} \cong 1$).

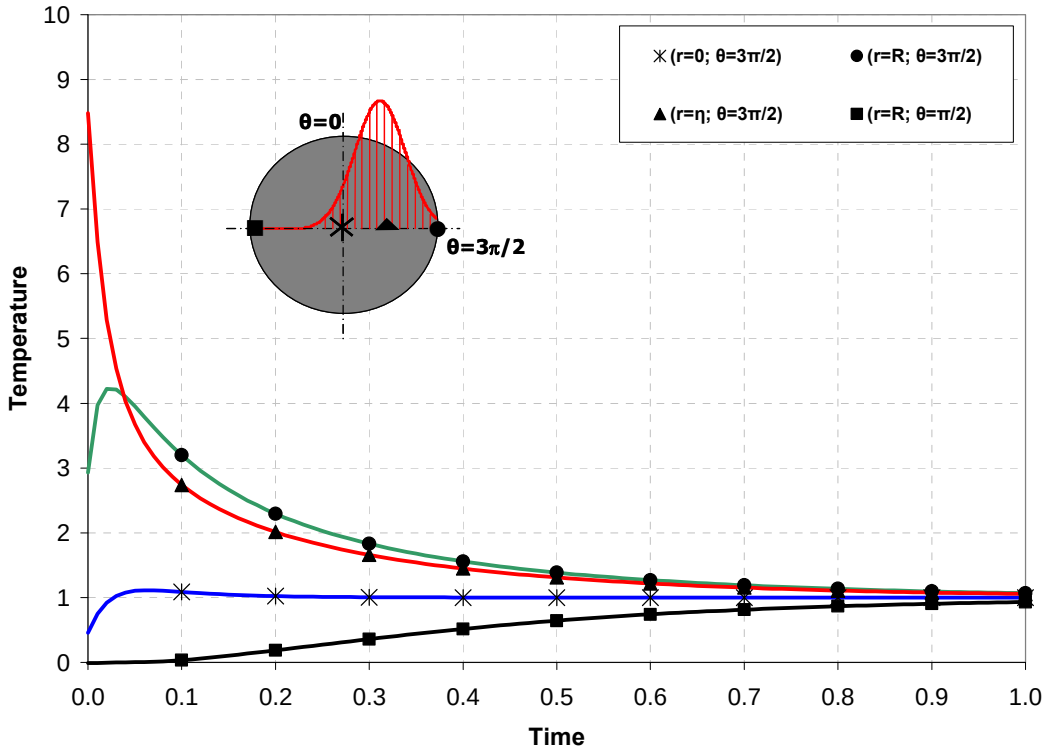

Figure 2.2: Temperature $\overline{T}$ as a function of time $\bar{t}$ with eccentricity $\overline{\eta} = 0.6$

2.2.4 Temperature distribution in graphite target rods

An application of the analytical solution described above is presented in this section: the CNGS project (see [2.3]) consists in producing a neutrino beam at CERN and sending it, several hundreds of meters under earth's crust, towards the Gran Sasso INFN laboratory in order to study the mass properties of these sub-atomic particles.

A neutrino beam of this type is generated from collisions of high energy protons in a beam with protons and neutrons in graphite targets. Thus, the system considered is a graphite cylindrical rod (dimension can be found in Table 2.1) axially hit by a proton beam (same scheme shown in Figure 2.1): the interaction rapidly generates large amounts of heat and triggers the emission, along with other particles, of a neutrino shower.

Considering the same energy distribution as indicated in Eq. 2.2, the heat load parameters resulting from a beam impact are collected in Table 2.2 while material properties can be found in Table 2.3. As stated in the introduction to this chapter, material properties were considered independent of temperature; data listed in following tables corresponds to average values calculated with respect to the expected range of temperature.

Table 2.1: Target rod dimension

Target rod dimension	
Radius	R=2.5 mm
Length	L=100 mm

Table 2.2: Energy distribution parameters relative to proton beam impact on graphite target rods.

Heat load parameters	
Thermal shock duration	τ =10 μs
Maximum specific energy	$U_{max}=8.61\cdot10^{5}$ J/kg
Beam eccentricity (w.r.t. rod axis)	η =1.5 mm
Standard deviation of the energy distribution	φ = 0.63 mm
Number of protons	$N_p=3.5\cdot10^{13}$ p
Proton energy	400 GeV

Table 2.3: Graphite thermo-physical properties.

Graphite properties	
Mass density	ρ = 1850 kg/m^3
Thermal conductivity	K = 70 W/(m·°K)
Specific heat	c_p = 1350 J/(kg·°K)

Figure 2.3 Shows the temperature distribution on the graphite target rod obtained with the analytical method; it is possible to observe that thermal diffusion time is 0.2 s compared with the shock duration τ = 10 μs; so the initial assumption of neglecting heat conduction is valid.

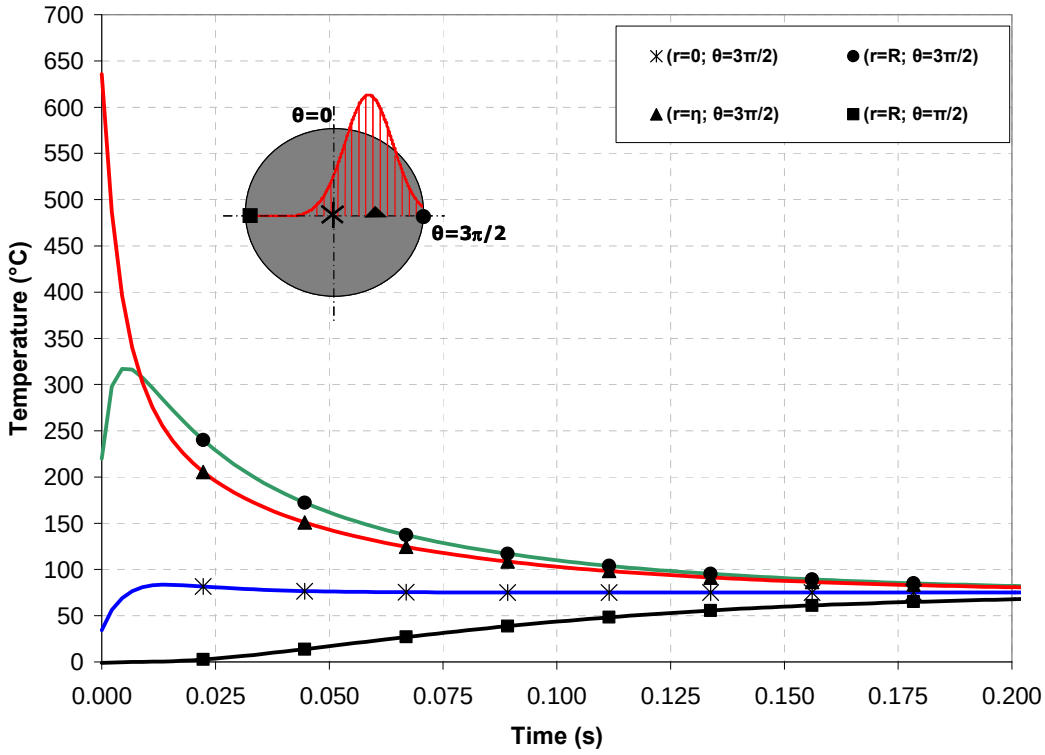

Figure 2.3: Temperature as a function of time at several locations of the CNGS target rod cross-section.

2.3 Thermal analysis of rectangular beams in case of rapid energy deposition

The above analytical approach has been extended to the case of rectangular beams. Same assumptions, adopted for cylindrical rods, have been considered.

The heat conduction equation is now written in the Cartesian coordinates (see Eq.2.10) while it is assumed that the energy deposition has a two-dimensional Gaussian distribution defined with Eq. 2.11, where $\varphi_{x,y}$ and $\eta_{x,y}$ are the standard deviation and the centre of the Gaussian function respectively in x and y directions. Figure 2.4 shows a scheme of the energy distribution over the rectangular domain.

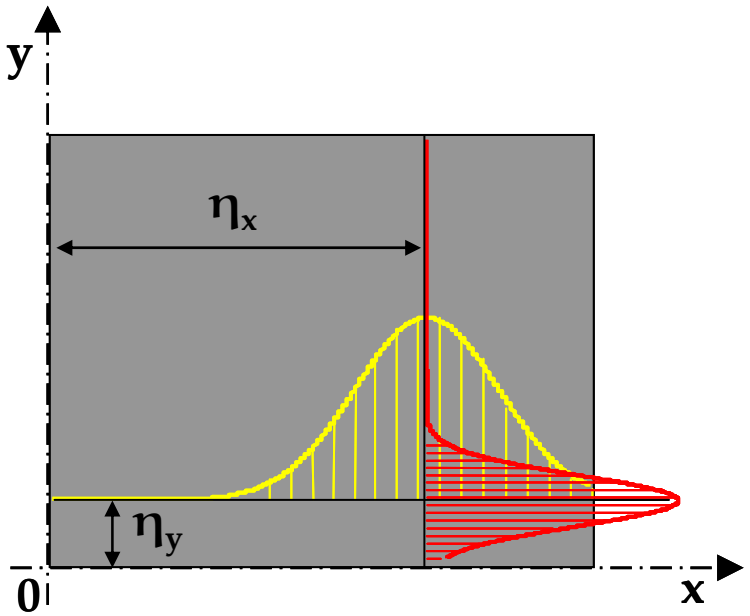

Figure 2.4: Typical energy distribution on rectangular domain due to particle beam impact. The two standard deviations of the Gaussian function in x and y directions could be different depending on particle beam parameters.

$$\frac{\partial^2 T(x,y,t)}{\partial x^2}+\frac{\partial T(x,y,t)}{\partial y^2}=\frac{1}{\kappa}\frac{\partial T(x,y,t)}{\partial t}$$

Eq. 2.10

$$\nabla^2 T(x,y,t)=\frac{1}{\kappa}\frac{\partial T(x,y,t)}{\partial t}$$

The maximum energy density $U_{\max}[J/kg]$ is found at $x=\eta_x$, $y=\eta_y$ as shown in Figure 2.4.

$$U(x,y)=U_{\max}\cdot e-\frac{\varphi_y^2(x-\eta_x)+\varphi_x^2(y-\eta_y)}{2\varphi_x^2\varphi_y^2}$$

Eq. 2.11

$$U(x,y)=U_{\max}\cdot f(x)\cdot g(y)$$

Having assumed that no heat diffusion occurs during the heating period, the temperature distribution at the end of the thermal shock can be simply calculated, as in the previous case with circular domain, with Eq. 2.12 that provides also the initial condition for the solution of the heat conduction equation.

$$T_0(x,y) = \frac{U(x,y)}{c_p} \qquad \text{Eq. 2.12}$$

Thanks to the adiabatic hypothesis, the total energy deposited on the rectangular plate remains constant, so the final uniform temperature T_F at the end of the heat diffusion process can be calculated as in the previous problem with circular domain:

$$T_F = \frac{\int_0^{L_x}\int_0^{L_x} U(x,y)dxdy}{c_p(L_x \cdot L_y)} \qquad \text{Eq. 2.13}$$

The boundary conditions, resulting from the adiabatic hypothesis, are given by:

$$\left.\frac{\partial T(x,y,t)}{\partial x}\right|_{x=L_x} = 0$$
$$\left.\frac{\partial T(x,y,t)}{\partial y}\right|_{y=L_y} = 0 \qquad \text{Eq. 2.14}$$

Initial temperature distribution given by Eq. 2.12 can be replaced by its Fourier-series expansion: assuming that the energy deposition is written as the second expression of Eq. 2.11, the following equation was obtained (n and s are the Fourier expansion index and $a_{n,s}$ are the usual series coefficients):

$$T_0(x,y) = \frac{U_{\max}}{c_p}\sum_{n=0}^{\infty}\sum_{s=0}^{\infty} a_n(x)H_n(x)\cdot a_s(y)H_s(y)$$
$$T_0(x,y) = \sum_{n,s} F_n(x)\cdot G_s(y) \qquad \text{Eq. 2.15}$$

where $H_n(x) = \cos(nx)$ if n is even and $H_n(x) = \sin(nx)$ if n is odd.

Making use of the separation of variables method, the function $T(x,y,t)$ can be reduced to the following form:

$$T(x,y,t) = \frac{U_{\max}}{c_p}\sum_n\sum_s F_n(x)\cdot G_s(y)\cdot \mathrm{I}_{n,s}(t) \qquad \text{Eq. 2.16}$$

where F_n and G_s are the Fourier expansions defined in Eq. 2.15. The expression (Eq. 2.16) must satisfy the diffusion equation (Eq. 2.10). Solution of the previous equation can be obtained by means of standard methods for Partial Differential Equations and can be written in the following form:

$$T(x,y,t) = \frac{U_{\max}}{c_p} \sum_n \sum_s F_n(x) \cdot G_s(y) \cdot e^{-\kappa \cdot \lambda_{n,s}^2 \cdot t} \qquad \text{Eq. 2.17}$$

Where $\lambda_{n,s}$ are the eigenvalues of the problem obtained from the application of the adiabatic condition (Eq. 2.14) and κ is the thermal diffusivity.

2.4 Thermal analysis of rectangular beams: slow energy deposition

The analytical model was also extended to the case of slow energy deposition (of the order of seconds), when heat diffusion plays a relevant role in the calculation of temperature evolution. Assuming that energy is linearly deposited over time during the interaction with particle beams, the energy rate W can be simply calculated as follows:

$$W(x,y) = \frac{U(x,y)}{\tau} \qquad \text{Eq. 2.18}$$

Figure 2.5 shows a qualitative scheme of the constant energy rate deposited. The heat load can be discretized over time in several short energy pulses $\Delta\tau$; thermal response of the system to rapid energy deposition has been already analyzed in previous paragraphs and can be applied also in this case.

Given the linearity of the system the global response to a slow transient thermal load can be calculated superimposing the solutions obtained from each short energy pulses $\Delta\tau$.

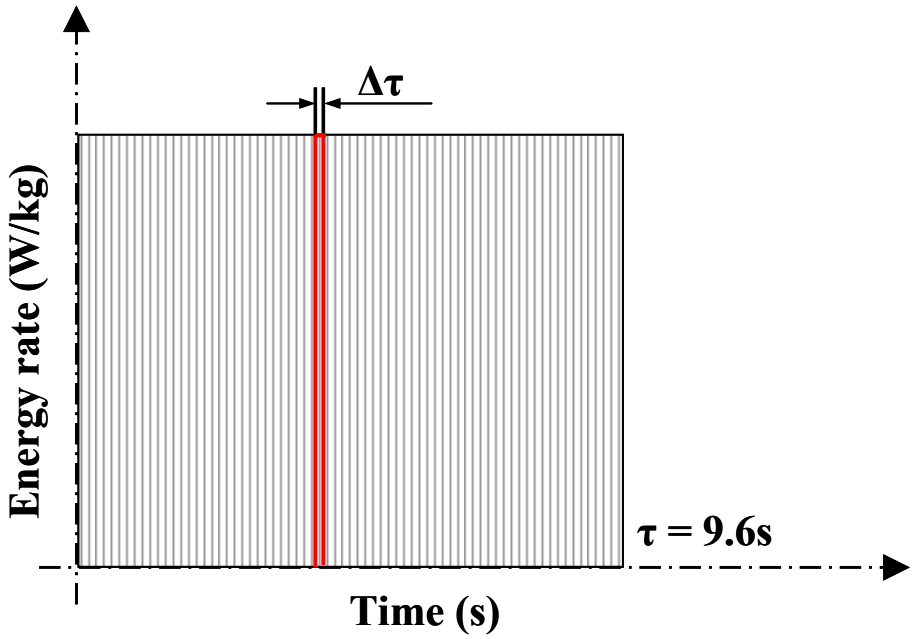

Figure 2.5: Qualitative scheme of constant specific power deposited over a long time. Heat load can be discretized and thermal response can be evaluated by the superposition of the solutions obtained from rapid energy pulses Δτ.

$$T_i(x,y,t) = \frac{W_{\max} \cdot \Delta\tau}{c_p} \sum_n \sum_s F_n(x) \cdot G_s(y) \cdot e^{-\kappa \cdot \lambda_{n,s}^2 \cdot (t - i\Delta\tau)}$$
$$h(x,y,t) = \sum_n \sum_s F_n(x) \cdot G_s(y) \cdot e^{-\kappa \cdot \lambda_{n,s}^2 \cdot t} \qquad \text{Eq. 2.19}$$
$$T_i(x,y,t) = \frac{W_{\max} \cdot \Delta\tau}{c_p} \cdot h(x,y,t - i\Delta\tau)$$

The first expression in Eq. 2.19 shows the ith solution of thermal problem corresponding to the ith energy pulse Δτ.

This approach is similar to the one used to evaluate structural response of a system to an arbitrary excitation as explained in [2.7]: the second expression in Eq.2.19 is the unit response of the system to a energy pulse, thus $T_i(x,y,t)$ can be written as a product between the constant heat load W and the response to a unit impulse excitation $h(x,y,t)$. Thermal response can be finally evaluated by the superposition of the ith solutions as follows:

$$T(x,y,t) = \sum_i W \cdot h(x,y,t - i\Delta\tau) \cdot \Delta\tau \qquad \text{Eq. 2.20}$$

Considering the limit of the discretization, Eq. 2.20 can be solved as an integral of convolution (see [2.7]) over the time τ during which the energy is deposited.

$$T(x,y,t) = W * h(x,y,t-\tau)$$
$$T(x,y,t) = \int_0^{\tau} \left(W \cdot h(x,y,t-\tau)\right) \cdot d\tau \qquad \text{Eq. 2.21}$$

The following expressions represent the solution of the convolution integral as written in Eq. 2.21:

$$T(x,y,t \le \tau) = \frac{W_{\max}}{c_p} \sum_n \sum_s F_n(x) \cdot G_s(y) \cdot \left(\frac{1 - e^{-\kappa \cdot \lambda_{n,s}^2 \cdot t}}{\kappa \cdot \lambda_{n,s}^2} \right) \qquad \text{Eq. 2.22}$$
$$T(x,y,t > \tau) = T(x,y,\tau) \cdot e^{-\kappa \cdot \lambda_{n,s}^2 \cdot (t-\tau)}$$

The solution is split into two parts: during the energy deposition $(t \le \tau)$ and after the end of the thermal load $(t > \tau)$. The maximum increase of temperature corresponds to the maximum of the energy deposition $x = \eta_x$ and $y = \eta_y$.

$$T_{\max}(t) = T(\eta_x, \eta_y, t) \qquad \text{Eq. 2.23}$$

2.4.1 Temperature evolution due to slow energy deposition on SPS collimator

The method described above, based on the integral of convolution, was applied to the thermal analysis of SPS collimators (see [2.4]). The component directly interacting with the proton beam can be simulated with a squared parallelepiped infinitely long; assuming that the energy distribution is longitudinally constant, no heat diffusion takes place in longitudinal direction and the system can be reduced to a two-dimensional problem. The energy deposition is centered in the vertex of the squared domains as shown in the scheme of Figure 2.6.

Table 2.4 indicates the dimensions of the square domain of solution, Table 2.5 includes all the heat load parameters relative to the proton beam interacting with the structure, while Table 2.6 shows the material properties used in the calculations.

Table 2.4: Dimensions of the squared domain directly interacting with the proton beam.

Target rod dimension	
X - dimension	L_x = 33 mm
Y - dimension	L_y = 33 mm

Table 2.5: Energy distribution parameters relative to slow proton extraction.

Heat load parameters	
Thermal shock duration	τ = 9.8 s
Maximum specific energy	U_{max} = $1.07 \cdot 10^5$ J/kg
x-coordinate of beam centre	η_x = 0.5 mm
y-coordinate of beam centre	η_y = 0.5 mm
Energy distribution standard deviation	φ_x = 2.2 mm
Energy distribution standard deviation	φ_y = 2.2 mm
Number of protons	N_p = $3.5 \cdot 10^{13}$ p
Proton energy	400 GeV

Table 2.6: Copper thermo-physical properties.

Cu properties	
Mass density	ρ = 8960kg/m^3
Thermal conductivity	K = 391W/(m·°K)
Specific heat	c_p = 385 J/(kg·°K)

Figure 2.6 shows temperature evolution at different locations of the squared domain. The temperature increase is not linear during the energy deposition ($t \le \tau$) and the effect of heat diffusion can be clearly observed; for $t > \tau$ no thermal load acts on the system and temperature distribution approaches the uniform value T_F reached at the end of the heat diffusion process.

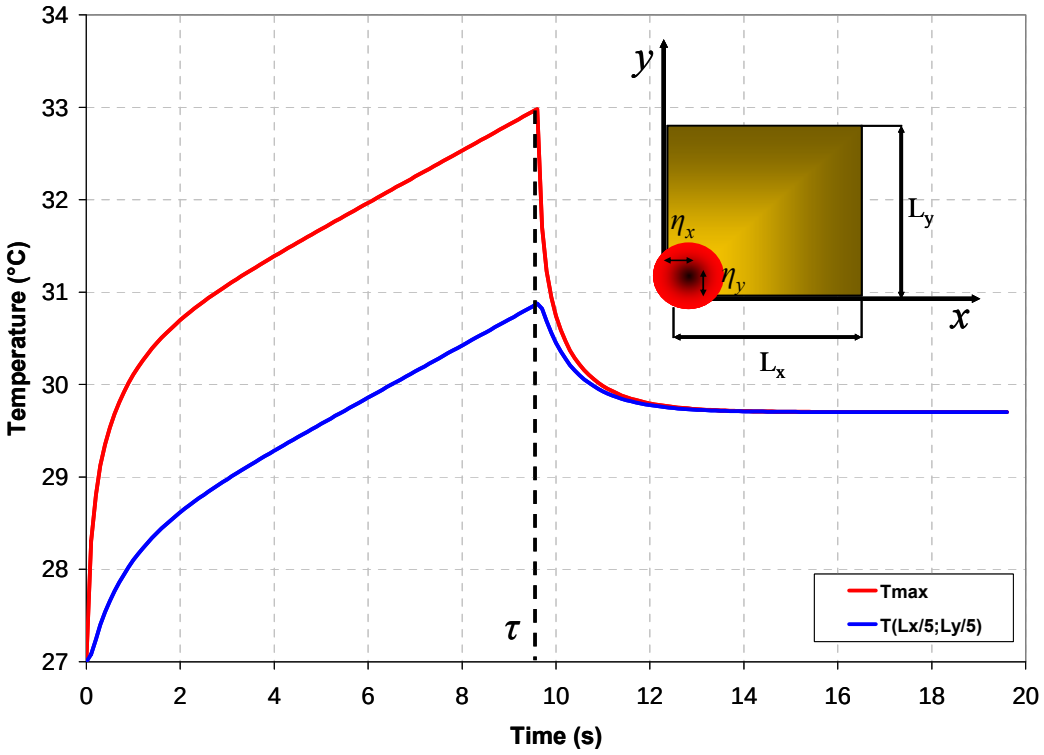

Figure 2.6: Temperature as a function of time in case of slow energy deposition. Copper square domain with energy deposition centered in a corner.

2.5 Summary

Thermal analysis of structures with simple geometry has been solved with analytical approach. The energy deposition resulting from the interaction between high energy particle beams and solids can be usually expressed in analytical way (Gaussian functions). Heat conduction equation was solved for circular and rectangular domains by means of Fourier-Bessel or Fourier expansions. This method can be applied to beam-like structures with circular and rectangular cross-section provided that the energy deposition is longitudinally constant.

Temperature distribution as a function of time was evaluated in case of rapid energy deposition, due to particle beam impact, assuming that no heat diffusion takes place within short time-scale. The method was also extended to the case of slow energy deposition (when heat diffusion must be taken into account) using the convolution integral applied to the thermal problem.

The analytical method developed found direct application in the study of CNGS target rods and SPS collimators; this allowed to appreciate the efficiency of the analytical approach able to quickly provide accurate results.

Thermal analysis developed in this chapter is the basis for the study of thermo-structural effects provoked by particle beams. Structural analysis will be presented in the next chapter.

2.6 Nomenclature

R	Radius of the cylindrical rod
L	Length of the cylindrical rod
r	Radial coordinate
$\bar{r} = r / R$	Non-dimensional radial coordinate
θ	Angular coordinate
x	Horizontal coordinate of rectangular domain
y	Vertical coordinate of rectangular domain
ρ	Mass density
K	Thermal conductivity
c_p	Specific heat
$\kappa = K /(\rho \cdot c_p)$	Thermal diffusivity
U_{max}	Maximum deposited specific energy
W_{max}	Maximum deposited specific power
η	Eccentricity of the energy distribution w.r.t. the cylindrical rod axis
η_x	x-coordinate of the centre of energy distribution on rectangular domain
η_y	y-coordinate of the centre of energy distribution on rectangular domain
$\bar{\eta} = \eta / R$	Non-dimensional eccentricity

φ	Standard deviation of the energy (Gaussian) distribution
φ_x	Standard deviation of the energy (Gaussian) distribution in *x*-direction on rectangular domain
φ_y	Standard deviation of the energy (Gaussian) distribution in *y*-direction on rectangular domain
$\overline{\varphi} = \varphi / R$	Non-dimensional standard deviation of the energy distribution
T	Temperature
T_F	Final uniform temperature
$\overline{T} = T / T_F$	Non-dimensional temperature
t	Time coordinate
$\bar{t} = (t - \tau) / t_d$	Non-dimensional time coordinate
$t_d = R^2 / \kappa$	Thermal diffusion time
τ	Thermal shock duration

References

[2.1] A. Fasso, A. Ferrari, P.R. Sala, Electron-photon transport in FLUKA: Status, Invited talk in the Proceedings of the Monte Carlo 2000 Conference, Lisbon, October 23-26 2000, A. Kling, F. Barao, M. Nakagawa, L. Tavora, P. Vaz eds., Springer-Verlag Berlin, p. 159-164 (2001)

[2.2] A. Fasso, A. Ferrari, J. Ranft, P.R. Sala, FLUKA: Status and Prospective for Hadronic Applications, Invited talk in the Proceedings of the Monte Carlo 2000 Conference, Lisbon, October 23-26 2000, A. Kling, F. Barao, M. Nakagawa, L. Tavora, P. Vaz eds., Springer-Verlag Berlin, p. 955-960 (2001).

[2.3] K. Elsener, 2000, General Description of the CERN Project for a Neutrino Beam to Gran Sasso (CNGS), CERN AC note 2000-03, CERN, Geneva.

[2.4] S. Gilardoni, A. Dallocchio, et al., Splitter Losses in the SPS, Proceedings of the APC meeting, 24th August 2006, CERN, Geneva

[2.5] W. Kalbreier, W.C. Middelkoop, P. Sievers, 1974, External Target at the SPS, CERN Technical Note LAB II/BT/74-1, CERN, Geneva

[2.6] M. Abramowitz and I.A. Stegun (Eds.), 1972, Handbook of Mathematical Functions, Dover Publications, New York, pp. 370-372

[2.7] W.T. Thomson, 1993, Theory of Vibration with Applications, 4th ed., Chapman & Hall, London, pp. 94-95.

Chapter 3

Structural effects due to rapid energy deposition: an analytical approach

3.1 Introduction

Thermal stress analyses are in most cases performed neglecting the effect of inertia force. Even if the thermal problem is time dependent, the study is conventionally solved considering the structural problem as a succession of quasi-static analyses. Thus, the dynamic effect due to the mass inertia of structures is not considered. When a heating process is very rapidly occurring, neglecting the inertia force could lead to a wrong estimation of the thermal stresses.

Studies of the dynamic response of rapidly heated structures, which take into account this effect, have been carried out in several fields of engineering and applied physics as from the 1950s, in particular in aerospace, nuclear engineering, and high energy particle physics.

In the aerospace engineering field, the problem of thermally induced vibrations was first studied by Boley [3.1] [3.2] and by Boley and Barber [3.3], with specific regard to flexible and slender spacecraft booms suddenly exposed to solar radiation. Boley's papers analyzed the behaviour of rectangular beams and plates submitted to rapid surface heating, pointing out that a sudden non uniform temperature rise produces a time dependent thermally induced bending moment that deforms the structure. Boley proposed a relation between the characteristic thermal diffusion time and the structural response time and showed that, if the two parameters are in the same order of magnitude and a sudden heating process occurs, transverse vibrations of the beam take place; Boley's result, which was derived for the case of surface heating, can be adapted to the problem of internally heated beams. Nevertheless, in this case, the structure shows a different behaviour as it will be discussed later.

In the same domain, further works were published by Murozono [3.4] and Blandino and Thornton [3.5] , who studied the case of slender cylindrical beams with uniform internal heating and non uniform heat transfer coefficient on the surface. These studies confirmed that thermally induced flexural vibrations occur in a flexible structure with low fundamental frequencies.

Concerning nuclear engineering, the main contributions came from Burgreen [3.6] [3.7] who studied the dynamic stresses induced in rods (analysis limited to the longitudinal behaviour), thin shells and solid spheres (structures typical of nuclear reactors and nuclear fuel) by rapid temperature pulses with uniform distribution; the effect of the duration of temperature pulses on dynamic stresses was analyzed.

In the field of high energy physics, studying the dynamic response of structures submitted to rapid internal heating is of paramount importance as in modern accelerators short duration impacts on structures induced by highly energetic particle beams frequently occur (by accident or on purpose). Studies on these subjects were first performed by Bargmann [3.8] for the case of a uniformly rapidly heated rod, on the basis of Laplace transforms and by Sievers [3.9] for thin rods and disks, making use of Fourier and Fourier-Bessel series with some particular boundary conditions; both works only dealt with longitudinal vibrations.

The studies cited were performed from mainly engineering point of view; some authors also presented a more theoretical approach: among the most relevant contributions are the works of Lessen [3.10] [3.11], Chadwick and Sneddon [3.12], Chadwick [3.13].

An extensive review on the subject of thermally induced waves and vibrations was made by Bargmann [3.14] .

Virtually all previous works on dynamic thermal stresses induced in rods and bars investigated separately the two problems of thermally induced flexural vibrations and of longitudinal propagation of thermo-elastic stress waves. Moreover, in the aerospace engineering field, the interest was mainly focused on surface heating problems, while in the nuclear engineering area, problems of rapid internal heating were studied considering only the case of uniform temperature distribution.

In this chapter both longitudinal and flexural behaviour of rods excited by rapid non uniform internal heating is studied; the contribution of quasi-static stresses as well

as of the dynamic effect is considered leading to a complete evaluation of displacements and of the thermal stress field.

The system considered is a cylindrical rod submitted to a rapid temperature rise induced by an internal non-uniform heat generation. The heat deposition is constant along the rod axis, and has an axially offset Gaussian distribution over the rod cross-section (same scheme as used in the previous chapter and shown in Figure 2.1). Such an occurrence is common to many particle accelerator components exposed to high energy sub-atomic particle beams. The developed method was directly applied to the study of beam targets in the frame of the CNGS experiment (see [3.15]).

Though particle beams should ideally impact cylindrical targets on their axis, in practice, because of mechanical misalignments, the beam is eccentric with respect to the axis of the cylinder. This induces, on top of axial vibrations, also lateral oscillations, leading, in some cases, to the collapse of the structure.

The analytical model developed takes into account both the longitudinal and flexural thermally induced vibrations; radial wave are small enough (compared to quasi-static deformations) to be neglected, as shown in [3.16].

Temperature distribution as a function of time, obtained with the approach shown in the previous chapter, is used as input for the structural analysis: an analytical model providing quasi-static and dynamic thermal stresses is fully developed on the basis of the work carried out by Bertarelli [3.17], Bertarelli and Kurtyka [3.18] and Dallocchio et al. [3.19].

A parametric study is also performed allowing to determine the influence of thermal shock duration on the longitudinal dynamic stresses and of the ratio of the diffusion time to the fundamental flexural period on dynamic bending stress and lateral oscillations. In the last section, a comparison between the analytical model and experimental measurements performed with a laser vibrometer (Wilfinger [3.20]) is presented.

3.2 Analytical model: main parameters and basic hypotheses

The system considered is a thin cylindrical rod of radius R and length L; the rod is supposed to be simply supported and is free to expand at its extremities. An isotropic material with linear elastic behaviour, without internal damping was

assumed. Thermal and mechanical properties were considered independent of temperature.

Temperature field obtained in previous chapter is used as input for the structural analysis. The evaluation of thermal stresses is based on the linear theory of thermo-elasticity; as stated above, the rapidity of the heat deposition invalidates the usual assumption that the effects of inertia may be disregarded: in fact, it will be shown that inertia plays a major role in the build-up of longitudinal and flexural stresses. However, in spite of the rapidity of the phenomenon, it can be demonstrated that the effects of radial inertia on longitudinal waves can be neglected if the frequency of the system is small compared to a certain reference value (Graff [3.21]): this is true for our case, as it will be proved later.

In its general expression, the linear theory of thermo-elasticity states that a full coupling exists between thermal and structural effects; this means that temperature variation influences the strain field but also that the rate of dilatational strain generates heat affecting the temperature field. As shown by Boley and Weiner [3.22], this coupling can be neglected if the time rate of change of the axial strain is of the same order of magnitude of that of temperature: it will be seen that this is true, at least for the initial phase of the thermo-mechanical response, which is the one of highest interest for this analysis.

On this ground, it is possible to consider this, as a weakly coupled thermo-elastic problem: i.e. the elastic strains are influenced by the temperature distribution but not the inverse. Thus, thermal and structural problems can be separated and sequentially solved; temperature field calculated in the previous chapter is used as input for the evaluation of quasi-static and dynamic thermal stresses.

3.3 Quasi-static stresses

Once the temperature distribution is known, it is possible to obtain the quasi-static stresses adapting a method developed by Goodier [3.23], and described in the book of Timoshenko and Goodier [3.24]; this method has been applied to a plane-strain case, assuming no longitudinal expansion occurs. The exact boundary condition is subsequently restored. Stress components are calculated in two different steps: first the stresses deriving from the application of a non-dimensional displacement potential $\overline{\psi}(\bar{r},\theta,\bar{t})$ are evaluated (same nomenclature used in chapter 2). Goodier has shown

that, in case of pure heat conduction, the general thermo-elastic equation (also known as the Duhamel-Neumann form of the Hooke's law) is automatically satisfied if the non-dimensional displacement potential is a solution of the following equation:

$$\frac{\partial \overline{\psi}(\bar{r},\theta,\bar{t})}{\partial \bar{t}} = \frac{1+\nu}{1-\nu}\overline{T} \qquad \text{Eq. 3.1}$$

Where $\overline{T}(\bar{r},\theta,\bar{t})$ is calculated with Eq.2.9. Since $\overline{T}$ becomes uniform when $\bar{t} \to \infty$ (at the end of the heat diffusion process), $\overline{\psi}$ can be immediately calculated:

$$\overline{\psi}(\bar{r},\theta,\bar{t}) = -\frac{1+\nu}{1-\nu}\sum_n \sum_s \frac{C_{n,s} J_n(\lambda_{n,s}\bar{r}) \cdot e^{-\lambda_{n,s}{}^2 \cdot \bar{t}}}{\lambda_{n,s}{}^2} H_n(\theta) + C \qquad \text{Eq. 3.2}$$

Here, C is a generic constant of integration, not affecting the displacement field. Once $\overline{\psi}$ is known, non-dimensional displacement components in radial and tangential direction $\overline{u}'$ and $\overline{v}'$, can be easily found by means of the following relations:

$$\begin{aligned} \overline{u}' &= \frac{\partial \overline{\psi}}{\partial \bar{r}} \\ \overline{v}' &= \frac{1}{\bar{r}}\frac{\partial \overline{\psi}}{\partial \theta} \end{aligned} \qquad \text{Eq. 3.3}$$

Subsequently, strain and stress components, $\overline{\sigma}_r', \overline{\sigma}_\theta', \overline{\tau}_{r\theta}'$ and $\overline{\sigma}_z'$, can be calculated from general kinematic relations for a two-dimensional problem and Hooke's general law (Duhamel-Neumann) when the axial strain ε_z is equal to zero:

$$\begin{aligned} \varepsilon_r' &= \frac{\partial \overline{u}'}{\partial \bar{r}} \\ \varepsilon_\theta' &= \frac{\overline{u}'}{\bar{r}} + \frac{1}{\bar{r}}\frac{\partial \overline{v}'}{\partial \theta} \\ \gamma_{r\theta}' &= \frac{1}{\bar{r}}\frac{\partial \overline{u}'}{\partial \theta} + \frac{\partial \overline{v}'}{\partial \bar{r}} - \frac{\overline{v}'}{\bar{r}} \end{aligned} \qquad \text{Eq. 3.4}$$

$$\begin{aligned}
&\bar{\sigma}'_r - \nu\left(\bar{\sigma}'_\theta + \bar{\sigma}'_z\right) = \left(\varepsilon'_r - \bar{T}\right)\\
&\bar{\sigma}'_\theta - \nu\left(\bar{\sigma}'_r + \bar{\sigma}'_z\right) = \left(\varepsilon'_\theta - \bar{T}\right)\\
&\bar{\sigma}'_z - \nu\left(\bar{\sigma}'_r + \bar{\sigma}'_\theta\right) = -\bar{T}\\
&\bar{\tau}'_{r\theta} = \frac{\gamma'_{r\theta}}{(1+\nu)}
\end{aligned} \qquad \text{Eq. 3.5}$$

The stress distribution calculated from the displacement potential satisfies the thermo-elastic equation, but not the boundary condition, requiring no forces on the external surface of the cylinder. Invoking the principle of superposition, a pressure field can be added in order to remove non-zero stresses on the lateral rod surface, thus restoring the correct boundary conditions. To do so, the formulation of the non-dimensional Airy stress function $\overline{\Phi}(\bar{r},\theta,\bar{t})$, as derived by Mitchell (Timoshenko and Goodier, [3.24]), is invoked for an ordinary plane-strain problem in polar coordinates. Once $\overline{\Phi}(\bar{r},\theta,\bar{t})$ is known, non-dimensional stress components $\bar{\sigma}''_{\bar{r}}, \bar{\sigma}''_\theta,$ and $\bar{\tau}''_{\bar{r}\theta}$ can be calculated from the following expressions:

$$\begin{aligned}
&\bar{\sigma}''_r = \frac{1}{\bar{r}}\frac{\partial\overline{\Phi}}{\partial\bar{r}} + \frac{1}{\bar{r}^2}\frac{\partial^2\overline{\Phi}}{\partial\theta^2}\\
&\bar{\sigma}''_\theta = \frac{\partial^2\overline{\Phi}}{\partial\bar{r}^2}\\
&\bar{\tau}''_{r\theta} = -\frac{\partial}{\partial\bar{r}}\left(\frac{1}{\bar{r}}\frac{\partial\overline{\Phi}}{\partial\theta}\right)
\end{aligned} \qquad \text{Eq. 3.6}$$

3.3.1 Quasi-static stresses for zero-axial strain

By superposing the stress components (Eq. 3.5 and Eq. 3.6), it is possible to calculate the non-dimensional quasi-static stresses. Previous calculations were made under the hypothesis of zero-axial strain: the resulting axial stress $\bar{\sigma}_{z0}$ is that of a rod whose axial deformation is prevented. Hence, we obtain:

$$\begin{aligned}
&\bar{\sigma}_r = \bar{\sigma}'_r + \bar{\sigma}''_r\\
&\bar{\sigma}_\theta = \bar{\sigma}'_\theta + \bar{\sigma}''_\theta\\
&\bar{\tau}_{r\theta} = \bar{\tau}'_{r\theta} + \bar{\tau}''_{r\theta}\\
&\bar{\sigma}_{z0} = \nu\left(\bar{\sigma}_r + \bar{\sigma}_\theta\right) - \bar{T}
\end{aligned} \qquad \text{Eq. 3.7}$$

The stresses given in Eq. 3.7 are non-dimensional and scaled to a reference stress equal to $\sigma_{ref} = E\alpha T_F$; this value corresponds to the opposite of the compressive axial stress induced by a uniform temperature T_F in a rod with fixed ends.

The quasi-static stress distribution shown in Figure 3.1 has a maximum at the end of the energy deposition $t = \tau$; these stresses tend to disappear as heat diffusion progresses and temperature distribution becomes uniform (apart from σ_{z0} which tends to σ_{ref}).

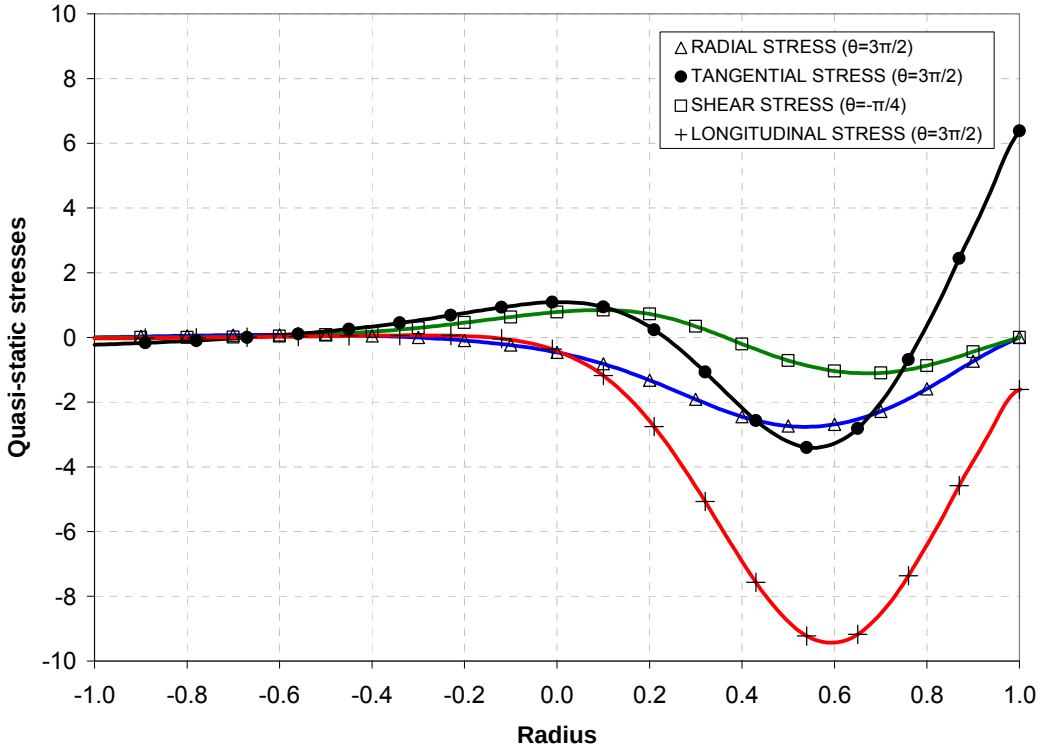

Figure 3.1: Quasi-static in-plane stresses $\bar{\sigma}_r, \bar{\sigma}_\theta, \bar{\tau}_{r\theta}$ and axial stress $\bar{\sigma}_{z0}$ at zero-axial strain as a function of $\bar{r}$ ($t = \tau$, $\bar{\eta} = 0.6$).

3.3.2 Equivalent dynamic loads

Axial stress in previous calculations was obtained in the hypothesis of zero-axial strain. In reality, the rod is longitudinally free at its extremities: to restore such condition, it is necessary to impose that the axial force and bending moment resulting from the axial stress at both ends of the rod are zero.

To do so, we calculate the resultant axial force $\bar{F}_z(\bar{t})$ and bending moment $\bar{M}_x(\bar{t})$ with opposite sign (see Eq. 3.8) and then apply these loads at the two extremities. By the de St. Venant's principle, at a certain distance from the ends, the actual axial stress

on the rod free to expand is obtained by superimposing to $\overline{\sigma}_{z0}$ the stresses induced by $\overline{F}_z(\bar{t})$ and $\overline{M}_x(\bar{t})$.

$$\overline{F}_z(\bar{t}) = -2\int_{-\frac{\pi}{2}}^{\frac{\pi}{2}}\int_0^1 \overline{\sigma}_{z0}(\bar{r},\theta,\bar{t})\bar{r}\,d\bar{r}\,d\theta$$
$$\overline{M}_x(\bar{t}) = -2\int_{-\frac{\pi}{2}}^{\frac{\pi}{2}}\int_0^1 \overline{\sigma}_{z0}(\bar{r},\theta,\bar{t})\bar{r}^2\sin\theta\,d\bar{r}\,d\theta \qquad \text{Eq. 3.8}$$

$$F_z(t) = \overline{F}_z(\bar{t})\cdot\left(E\alpha T_F R^2\right)$$
$$M_x(t) = \overline{M}_x(\bar{t})\cdot\left(E\alpha T_F R^3\right) \qquad \text{Eq. 3.9}$$

Eq. 3.9 represent dimensional quantities.

3.4 Dynamic stresses

The effect of inertia is essential for the correct evaluation of a thermal shock; in fact, if the temperature change within a body is fast enough, its thermal expansion is initially prevented by the body mass, establishing a coupling between thermally originated elastic forces and inertia forces. In the case of a rod, this gives birth to dynamic stresses propagating along the rod axis as elastic stress waves: assuming the thermal shock time τ is very short, at $t = \tau$, the system is still in a compressive state; the stress relaxation due to elastic forces starts from the extremities of the rod, so two stress waves appear, travelling from the extremities, superimposing at the centre and reflecting at the other ends.

The structural dynamic effects provoked by the thermal shock can be studied as the response of the system to the variable loads acting at the rod ends: the force $F_z(t)$ and moment $M_x(t)$ (Eq. 3.9). These loads, applied at the extremities of the beam, and superimposed to the quasi-static stress field, are necessary to ensure the dynamic equilibrium.

Having assumed that no diffusion occurs during thermal shock, the foregoing loads grow up linearly from zero to the maximum value given by $F_z(\tau)$ and $M_x(\tau)$ at the end of the energy deposition; from this time on, $F_z(t)$ remains constant (since it is

proportional to the deposited energy), while $M_x(t)$ decreases as the temperature distribution tends to become uniform because of thermal diffusion (Figure 3.2). To calculate the dynamic response of the system we have considered a piece-wise linear interpolation of the curve of equivalent thermal bending moment. As shown in Figure 3.2, the interpolation is quite coarse, but this did not notably affect the accuracy of the analysis.

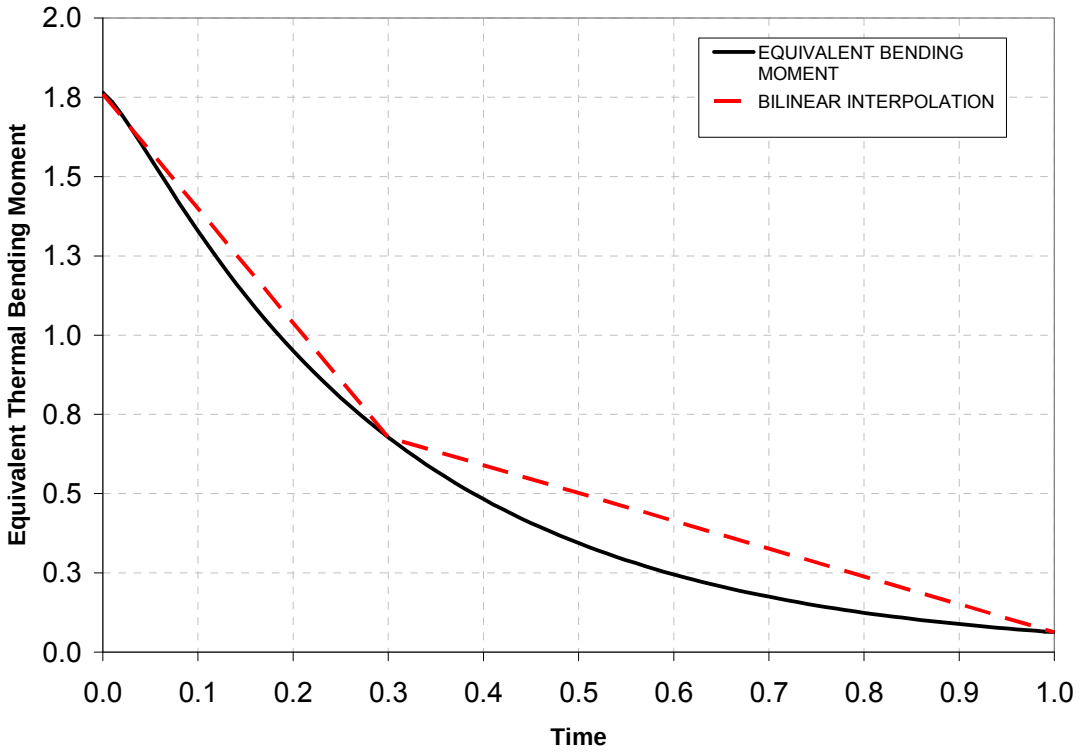

Figure 3.2: Equivalent thermal bending moment $\overline{M}_x(\bar{t})$ ($\bar{t} = (t-\tau)/t_d$).

Figure 3.3 shows the qualitative model of the dynamic loads and the corresponding unit functions *g(t)* and *g'(t)* (so $F_z(t) = F_z(\tau) \cdot g(t)$ and $M_x(t) = M_x(\tau) \cdot g'(t)$).

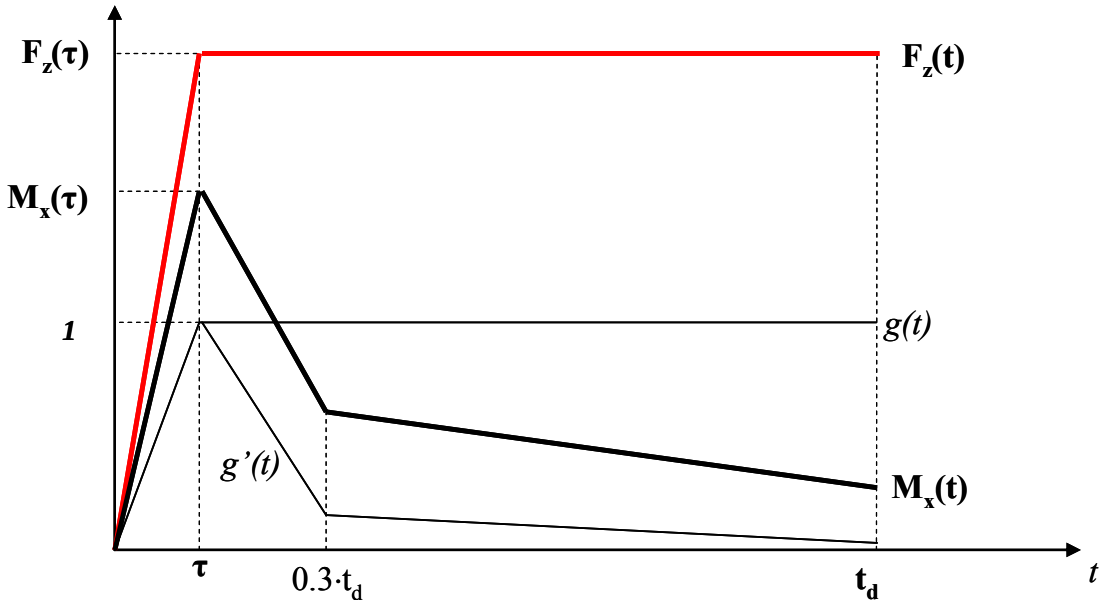

Figure 3.3: Equivalent dynamic excitations, qualitative plot.

At this stage of the analysis, we may wonder if the effects of force and moment can be treated separately. Indeed, this is the case, since $F_z(t)$, being the resultant of internal axial stresses, is always orthogonal to the rod cross-section and gives no contribution to the bending moment, even when the rod is deflected.

As a consequence, no mutual influence exists between axial force and bending moment, so the system can be considered linear, the axial and flexural behaviours can be studied separately and the superposition principle applied.

To calculate the system time-response, we have used the mode-summation method (see e.g. Thomson, [3.25]), which basically expands the deformation in terms of the longitudinal and flexural natural modes ($\phi_{z_i}(\bar{z})$ and $\phi_{f_i}(\bar{z})$) and of the generalized coordinates ($q_{z_i}(t)$ or $q_{f_i}(t)$) of a simply supported uniform beam, loaded at the extremities with $F_z(t)$ or $M_x(t)$ respectively. Given the slenderness of the rod, the classical Bernoulli-Euler beam theory has been assumed for the flexural behaviour.

The equation of motion for each linearly independent mode is obtained by the application of the Lagrange's equation which leads to:

$$\frac{d^2 q_i}{dt^2} + \omega_i^{\,2} q_i = \frac{Q_i}{m_i} \qquad \text{Eq. 3.10}$$

Where m_i and Q_i are the generalized masses and generalized forces for the i^{th} mode. The generalized force Q_i is obtained from the work done by the load $F_z(t)$ or $M_x(t)$ applied at the two ends, in the virtual displacement δq_i.

3.4.1 Flexural modal analysis

In case of bending, the lateral displacement $w(z,t)$ of a simply supported beam can be expanded in terms of the natural modes and of the generalized coordinates as follows:

$$w(z,t) = \sum_i \phi_{f_i}(z) \cdot q_{f_i}(t) \qquad \text{Eq. 3.11}$$

The expressions of mode shapes and natural (circular) frequencies for a simply supported beam under bending are given by:

$$\phi_{f_i}(z) = \sqrt{2}\sin\left(i\pi \cdot \frac{z}{L}\right) \qquad \text{Eq. 3.12}$$

$$\omega_{f_i} = (i\pi)^2 \sqrt{\frac{EJ}{mL^3}} \qquad \text{Eq. 3.13}$$

If the bending moment $M_x(t)$, as given in Figure 3.3, is applied at the rod extremities, the generalized force for the i^{th} mode takes the following expression:

$$\frac{Q_{f_i}(z)}{m_i} = \frac{M_x(\tau)\sqrt{2} \cdot i\pi}{m \cdot L}\left[1-(-1)^i\right] \cdot g'(t) \qquad \text{Eq. 3.14}$$

Where m is the mass of the rod, and $g'(t)$ is the unit excitation function shown in Figure 3.3.

Note that the modal shapes (Eq. 3.12) cannot satisfy the natural boundary condition for the actual load case (at $z=0$, $z=L$ $\frac{\partial^2 w(0)}{\partial z^2} = \frac{\partial^2 w(L)}{\partial z^2} = 0$ always); however it can be shown that w'' tends to its true value at the ends $\frac{\partial^2 w(0)}{\partial z^2} = \frac{\partial^2 w(L)}{\partial z^2} = \frac{M_x(t)}{EJ}$, provided a sufficiently large number of terms is used for

the expansion showed in Eq. 3.11. Generalized coordinates $q_{f_i}(t)$ are obtained by the well-known response of a single d.o.f. system excited by the superposition of multiple ramp functions (Thomson [3.25]).

Given ($t_2=0.3 \cdot t_d$) and ($t_3=t_d$) the following expression was obtained:

$$F1_i = -\frac{M_x[0]}{m} \cdot \frac{\sqrt{2} \cdot i \cdot \pi}{L} \cdot [1-(-1)^i]$$

$$F2_i = -\frac{M_x\left[\frac{t_2-\tau}{t_3}\right]}{m} \cdot \frac{\sqrt{2} \cdot i \cdot \pi}{L} \cdot [1-(-1)^i]$$

$$F3_i = -\frac{M_x\left[\frac{t_3-\tau}{t_3}\right]}{m} \cdot \frac{\sqrt{2} \cdot i \cdot \pi}{L} \cdot [1-(-1)^i]$$

$$F4_i = \frac{F2_i \cdot \tau - F1_i \cdot t_2}{t_2-\tau}$$

$$F5_i = F3_i - \frac{F1_i \cdot t_3}{\tau} - G2_i \frac{t_3-\tau}{t_2-\tau}$$

$$q_{f_i}(t>t_2) = \frac{F5_i}{(\omega_{f_i})^2} \cdot \left(\frac{t-t_2}{t_3-t_2} - \frac{\sin[\omega_{f_i}(t-t_2)]}{\omega_{f_i} \cdot (t_3-t_2)} \right) + \qquad \text{Eq. 3.15}$$

$$+ \frac{F4_i}{(\omega_{f_i})^2} \cdot \left(\frac{t-\tau}{t_2-\tau} - \frac{\sin[\omega_{f_i}(t-\tau)]}{\omega_{f_i} \cdot (t_2-\tau)} \right) + \frac{F1_i}{(\omega_{f_i})^2} \cdot \left(\frac{t}{\tau} - \frac{\sin(\omega_{f_i} t)}{\omega_{f_i} \tau} \right)$$

$$q_{f_i}(\tau \le t \le t_2) = \frac{F4_i}{(\omega_{f_i})^2} \cdot \left(\frac{t-\tau}{t_2-\tau} - \frac{\sin[\omega_{f_i}(t-\tau)]}{\omega_{f_i} \cdot (t_2-\tau)} \right) +$$

$$+ \frac{F1_i}{(\omega_{f_i})^2} \cdot \left(\frac{t}{\tau} - \frac{\sin(\omega_{f_i} t)}{\omega_{f_i} \tau} \right)$$

$$q_{f_i}(0<t<\tau) = \frac{F1_i}{(\omega_{f_i})^2} \cdot \left(\frac{t}{\tau} - \frac{\sin(\omega_{f_i} t)}{\omega_{f_i} \tau} \right)$$

Dynamic bending stress induced by lateral displacement *w(z,t)* immediately follows:

$$\begin{aligned}\phi''_{f_i}(z) &= -\sqrt{2}\cdot\left(\frac{i\pi}{L}\right)^2\cdot\sin\left(i\pi\cdot\frac{z}{L}\right)\\ w''(z,t) &= \sum_i \phi''_{f_i}(z)\cdot q_{f_i}(t)\\ \sigma_{f_d}(r,\theta,z,t) &= Ew''(z,t)\cdot r\sin\theta\end{aligned} \qquad \text{Eq. 3.16}$$

Where $w''(z,t)$ is the second derivative of the lateral displacement with respect to z.

In the following graphs, results are given for lateral displacement and bending stress at the middle of the rod, considering an eccentricity $\eta = 0.6R$; the results are scaled to the value of static lateral displacement w_s and static bending stress σ_{f_S} :

$$w_s\left(\frac{L}{2}\right) = \frac{M_x(\tau)\cdot L^2}{8EJ} \qquad \text{Eq. 3.17}$$

$$\sigma_{f_s} = \frac{M_x(\tau)\cdot R}{J} \qquad \text{Eq. 3.18}$$

Figure 3.4 shows that the dynamic deflection of the rod is twice as large as the static one, confirming the findings of Boley [3.1]; the oscillations have a slight drift because the thermal moment decreases during the heat diffusion process.

Interestingly, Figure 3.5 shows that the dynamic bending stress can be almost three times larger than the static one σ_{f_s} : to the authors' knowledge this was never evidenced in previous works.

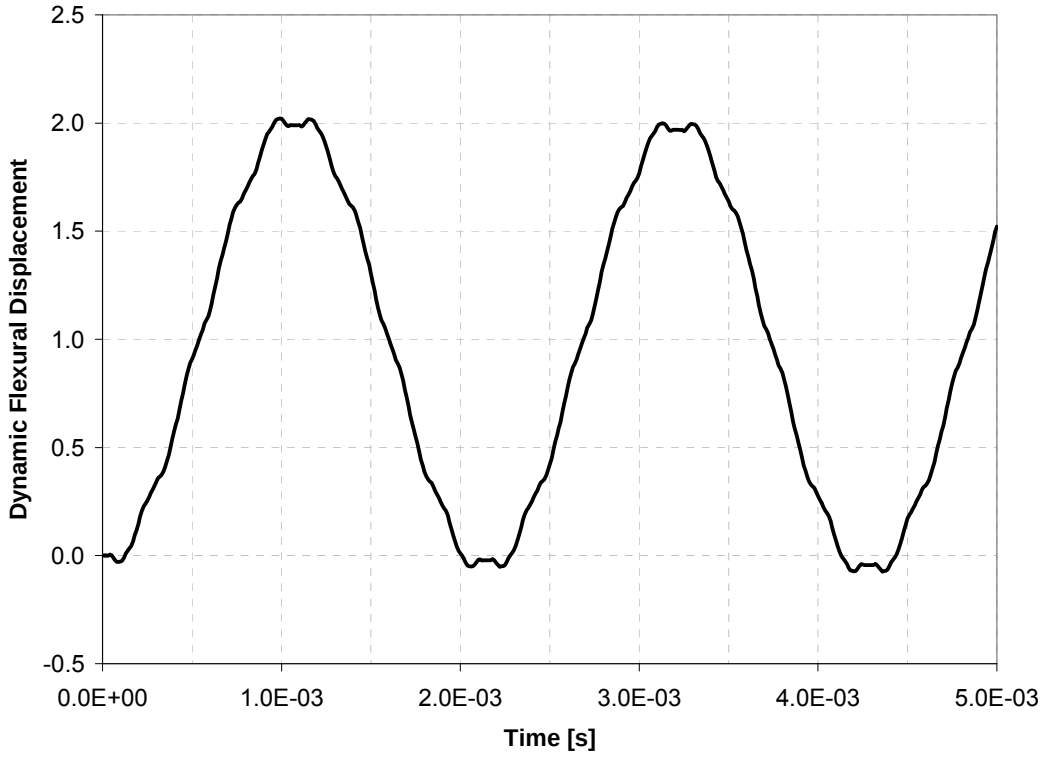

Figure 3.4: Dynamic flexural response w / w_s at $z = L/2$ (r=R; φ=3π/2; η=0.6)

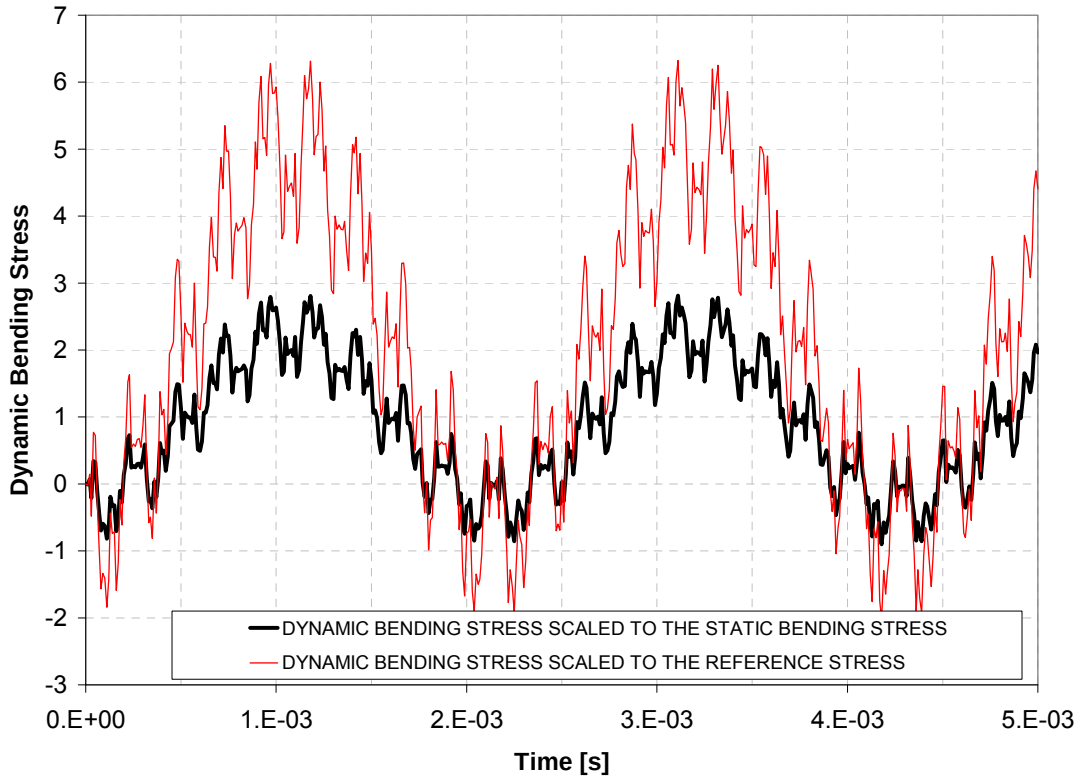

Figure 3.5: Scaled dynamic bending stress ($\sigma_{f_d} / \sigma_{f_s}$ and $\sigma_{f_d} / \sigma_{ref}$) at $z = L/2$ (*r=R; θ=3π/2; η=0.6R*)

3.4.2 Longitudinal modal analysis

The longitudinal dynamic stress is calculated by the same method used for dynamic bending. In this case the variable of interest is the longitudinal displacement, which is given by:

$$u_z(z,t) = \sum_i \phi_{z_i}(z) \cdot q_{z_i}(t) \qquad \text{Eq. 3.19}$$

The generalized forces are given by:

$$\frac{Q_{z_i}(t)}{m_i} = \frac{F_z(\tau)\sqrt{2}}{m}\left[1-(-1)^i\right] \cdot g(t) \qquad \text{Eq. 3.20}$$

Natural modes and natural frequencies are:

$$\phi_{z_i}(z) = \sqrt{2}\cos\left(i\pi \cdot \frac{z}{L}\right) \qquad \text{Eq. 3.21}$$

$$\omega_{z_i} = \frac{i\pi}{L}\sqrt{\frac{E}{\rho}} \qquad \text{Eq. 3.22}$$

Generalized coordinates $q_{zi}(t)$ are given by the response of a single d.o.f. system excited by a ramp function:

$$\begin{aligned} F_{z_i} &= -\frac{F_z(\tau)}{m} \cdot \sqrt{2} \cdot [1-(-1)^i] \\ q_{z_i}(t \geq \tau) &= \frac{F_{z_i}}{(\omega_{z_i})^2} \cdot \left(1 - \frac{\sin(\omega_{z_i} t)}{\omega_{z_i}\tau} + \frac{\sin[\omega_{z_i}(t-\tau)]}{\omega_{z_i}\tau}\right) \\ q_{z_i}(t < \tau) &= \frac{F_{z_i}}{(\omega_{z_i})^2} \cdot \left(\frac{t}{\tau} - \frac{\sin(\omega_{z_i} t)}{\omega_{z_i}\tau}\right) \end{aligned} \qquad \text{Eq. 3.23}$$

Finally, the dynamic longitudinal stress component is calculated as follows:

$$\phi'_{z_i}(z) = -\sqrt{2} \cdot \frac{i\pi}{L} \cdot \sin\left(i\pi \cdot \frac{z}{L}\right)$$
$$u'_z(z,t) = \sum_i \phi'_{z_i}(z) \cdot q_{z_i}(t) \qquad \text{Eq. 3.24}$$
$$\sigma_{z_d}(z,t) = E \cdot u'_z(z,t)$$

Where $u'_z(z,t)$ denotes the first derivative of u_z, with respect to z, i.e. the longitudinal strain.

Figure 3.6 shows the evolution over time of the longitudinal dynamic stress. The values are scaled with respect to σ_{ref}; the maximum longitudinal dynamic stress is exactly two times larger than the reference stress value.

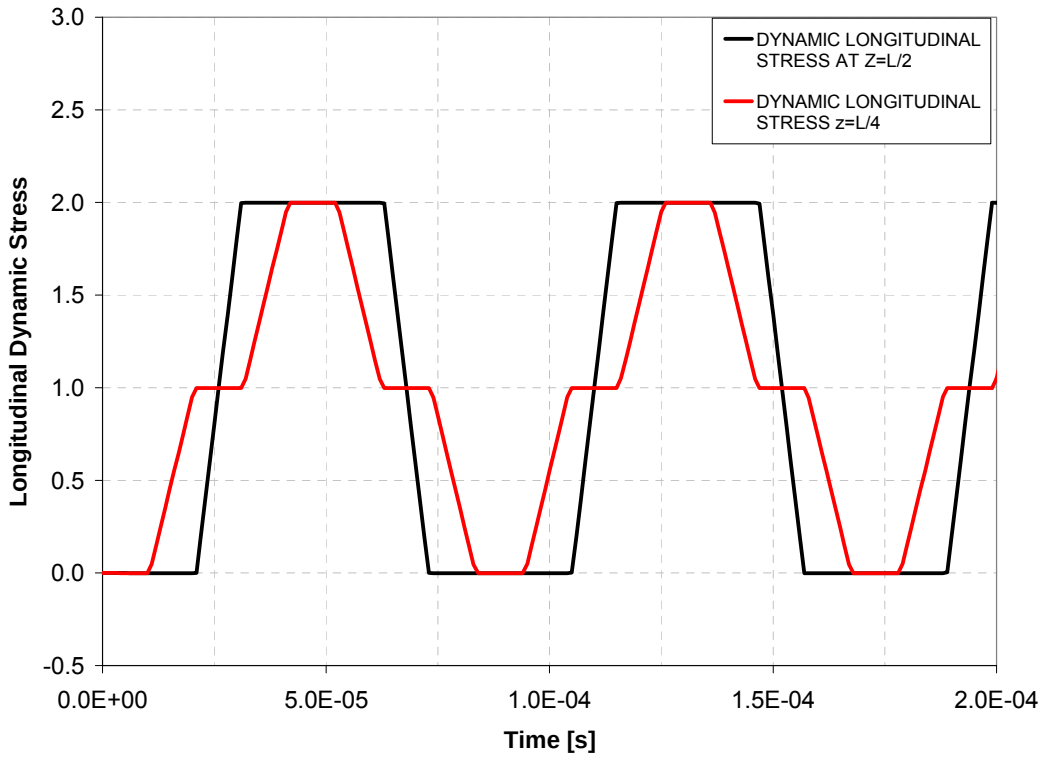

Figure 3.6: Dynamic axial stress scaled to the reference stress $\sigma_{z_d} / \sigma_{ref}$ as a function of time at different location along the cylinder

Figure 3.7 shows the progression of stress relaxation and the first reflection of the longitudinal stress wave; t_0 is the first fundamental period of longitudinal vibrations, $t_0 = 2L/c_0$; ($c_0 = (E/\rho)^{1/2}$ is the velocity of longitudinal wave propagation).

At time $t = \tau$, the dynamic tensile stress, relaxing the quasi-static compressive stress, only affects the end parts of the rod (elsewhere $\sigma_{z_d} = 0$); at time $t = \tau + t_0/4$, the two dynamic stress waves travelling in opposite directions, have already begun to superimpose attaining $\sigma_{z_d}/\sigma_{ref} = 2$. At $t=t_0/2$, each of the two waves has reached the opposite end, and reflection starts to play its role.

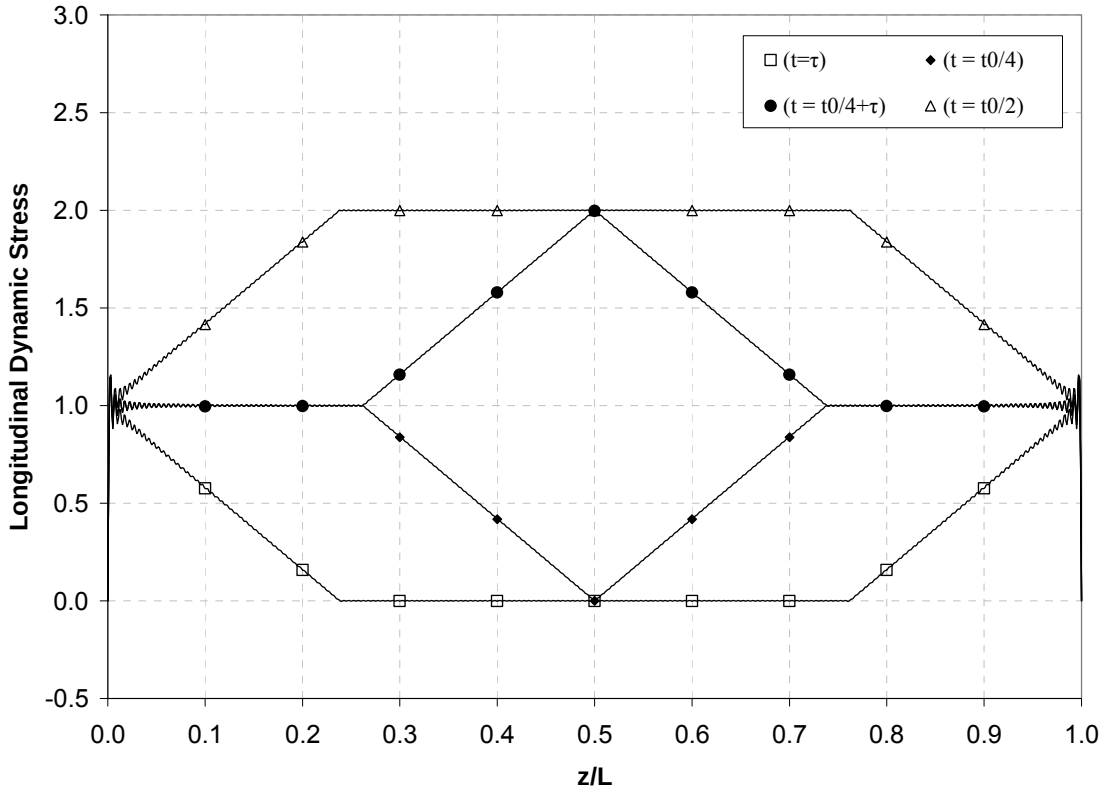

Figure 3.7: Scaled dynamic axial stress $\sigma_{z_d}/\sigma_{ref}$ along rod length at different instants

3.4.3 Influence of thermal shock duration on maximum longitudinal dynamic stress

In order to extend the applicability of this method to a broader class of problems, we want to analyze the influence of thermal shock duration τ on maximum dynamic longitudinal stress.

The dynamic longitudinal stress is considered in the middle of the rod, where the maximum value is reached; it can be easily verified that the maximum stress at $\bar{z} = 1/2$ always occurs at time $t = \tau + t_0/4$.

As shown by Eq. 3.25, the thermal shock response spectrum H, defined as the ratio between the dynamic and the reference stress, is now function only of the thermal shock parameter τ:

$$H(\tau) = \frac{\sigma_{z_d}\left(\frac{1}{2}, \tau + \frac{t_0}{4}\right)}{\sigma_{ref}} \qquad \text{Eq. 3.25}$$

By letting $\tau_0 = \tau / t_0$, after some manipulations we obtain:

$$H(\tau_0) = \frac{4}{\pi}\left[\sum_i \left[\frac{1-(-1)^i}{2}\left[\frac{1}{i} + \frac{(-1)^{\frac{i-1}{2}} \cdot (1-\cos(i2\pi\tau_0))}{i^2 2\pi\tau_0}\right] \cdot (-1)^{\frac{i-1}{2}}\right]\right] \qquad \text{Eq. 3.26}$$

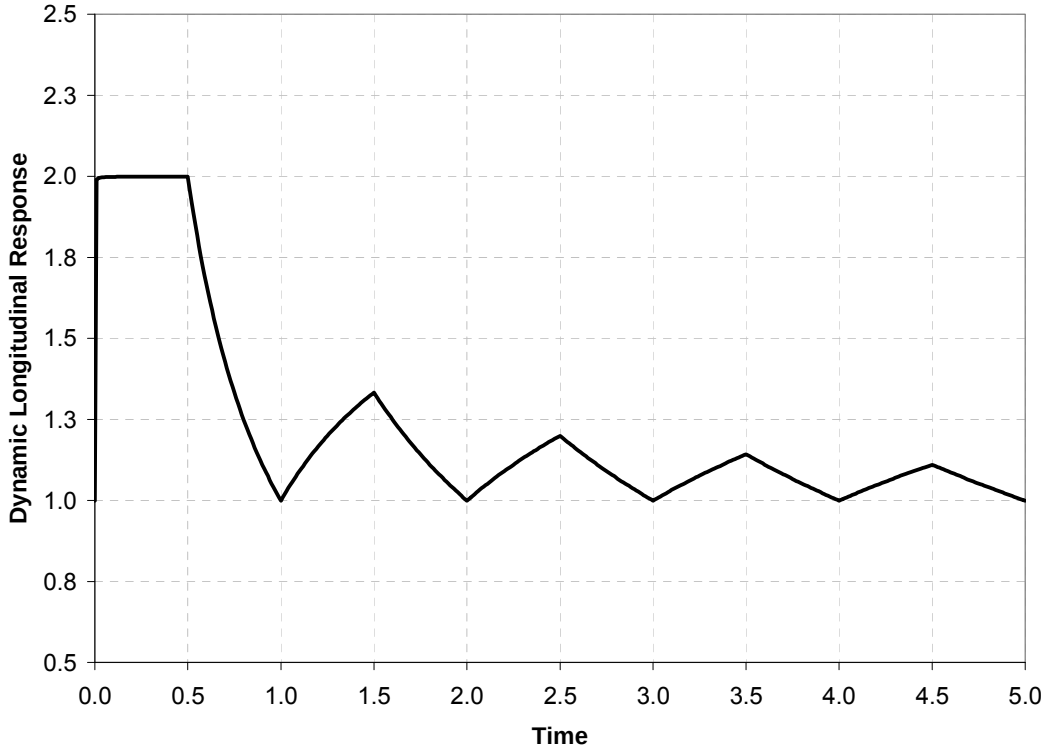

Figure 3.8: Thermal shock longitudinal dynamic response $H = \sigma_{z_d}(0.5, \tau + t_0/4)/\sigma_{ref}$ as a function of $\tau_0 = \tau / t_0$.

Figure 3.8 shows that the maximum longitudinal dynamic stress is initially twice as large as the reference value. This relation holds until the parameter τ is smaller than half of the first fundamental period $t_0/2 = L/c_0$; if the thermal shock is longer than this, the heating process will be slower than the stress relaxation phenomenon occurring through wave propagation and the maximum longitudinal dynamic stress will never be reached; in other words, the temperature rise time τ is longer than the time required for the stress wave to propagate along the rod at the speed of sound c_0.

This relation between maximum longitudinal dynamic stress, first fundamental period of the system and thermal shock duration τ, is very important in the design of systems submitted to thermal shocks; in fact, given a heating duration τ, the natural frequency of the system could be chosen, by modifying its geometry, so as to limit the maximum dynamic longitudinal stress.

3.4.4 Influence of the ratio between thermal and structural characteristic response time on the dynamic maximum deflection.

Some considerations should be done also on the effect of the thermal shock parameter τ on the dynamic flexural response. In this case τ is typically some orders of magnitude smaller than the first natural period of flexural oscillation, thus varying τ has a negligible influence on the maximum dynamic flexural deflection. More interestingly, for the flexural behaviour, the characteristic heat diffusion time t_d should be compared to the first fundamental period of bending oscillation $t_f = 2\pi/\omega_{f1}$, as illustrated by Boley [3.1] [3.2] and Boley and Barber [3.3], who identified this ratio as the key parameter for the description of thermally induced oscillations; following his notation we define $B = \sqrt{t_d/t_f}$.

In his papers, Boley analyzed the ratio of dynamic maximum deflection w_{dyn} to static maximum deflection w_{st} as a function of the parameter B (also known as Boley Number) showing that, for beams submitted to rapid surface heating, thermally induced vibrations occur only when B is close to or smaller than one.

In this paragraph we can show that the dynamic behaviour dependence upon B for internally heated beams is quite different.

We have first identified a range of values for B, from zero to thirty, which covers several engineering applications. Values of B smaller than one correspond to flexible

structures with low fundamental frequencies made up of materials with high thermal conductivity; higher values of B correspond to stiffer structures or to structures made up of materials with low thermal conductivity.

The variation of the ratio of dynamic maximum deflection to static maximum deflection as a function of B is plotted in Figure 3.9 for the case of rapid internal heating. We can observe that for values of B larger than two, the dynamic maximum deflection is roughly twice the correspondent static deformation; practically this means that thermally induced flexural vibrations play a relevant role for values of B larger than one.

For engineering design purposes, we present an analytical function that interpolates the exact curve (see Figure 3.9):

$$\frac{w_{dyn}}{w_{st}} = \left(\frac{2B^2}{0.1 + B^2} \right) \cdot \left(1 - e^{\frac{-\pi \cdot B^2}{2.3}} \right) \qquad \text{Eq. 3.27}$$

It is also possible to evaluate the variation of the ratio of maximum dynamic bending stress to static bending stress with parameter B, (see Figure 3.10). As already shown in paragraph 3.4.1, this ratio could reach a value up to three (see Figure 3.5).

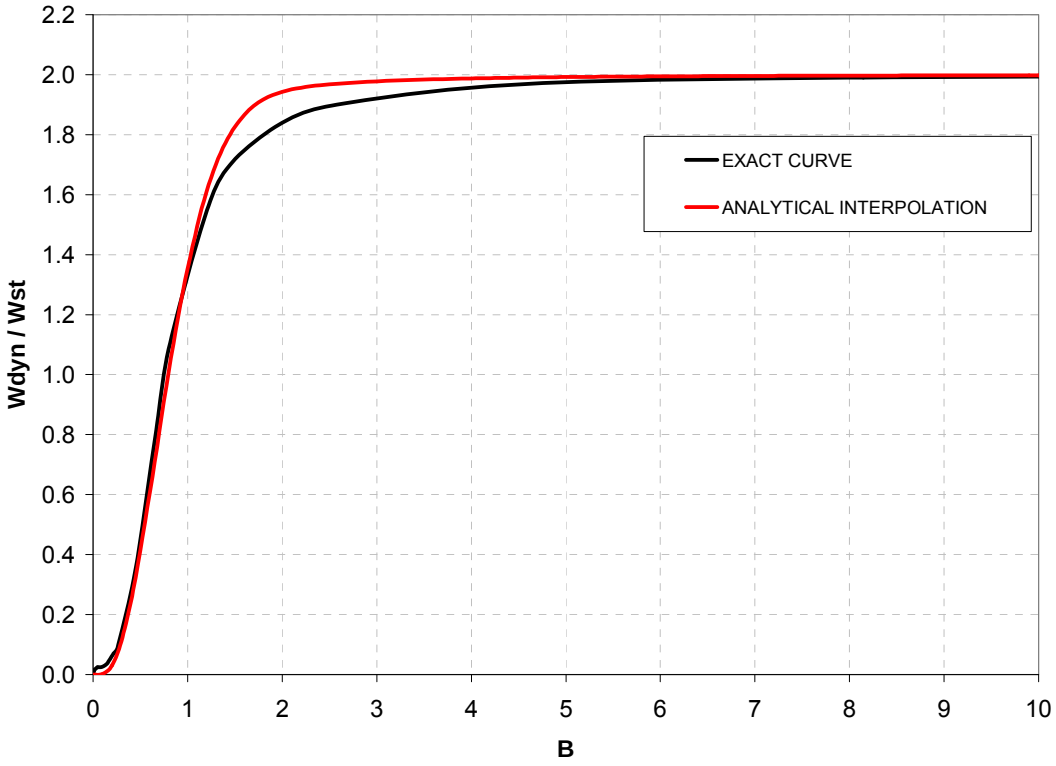

Figure 3.9: Variation of the ratio of dynamic maximum deflection to static maximum deflection with parameter B at $z = L/2$

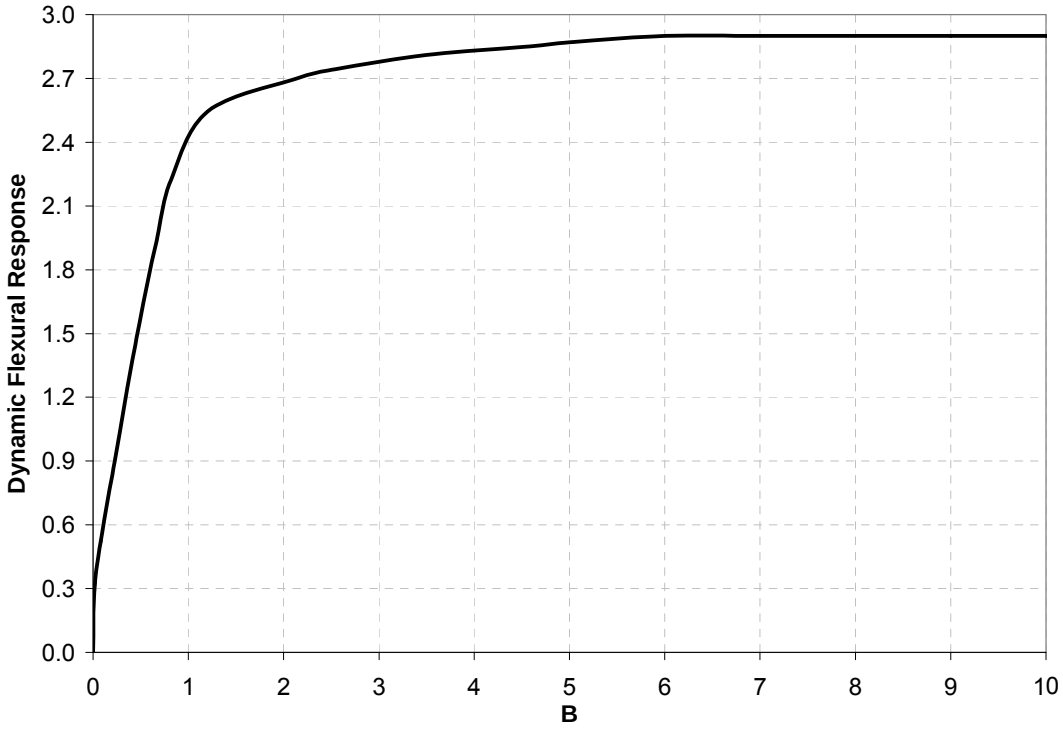

Figure 3.10: Variation of the ratio of maximum dynamic bending stress to static bending stress with parameter B at $z = L/2$

The results shown above are quite different from the one presented by Boley in his papers [3.1] [3.2] [3.3]. Nevertheless, we can confirm that Boley's number is the key parameter that governs the dynamic phenomenon of thermally induced vibration; but the range of values for B and the relation between B and the dynamic flexural response of the structure are different depending on thermal boundary conditions.

3.4.5 Global axial stress

The global axial stress, as already mentioned, can be evaluated superimposing the zero-strain quasi-static component with the dynamic bending stress and the dynamic longitudinal stress:

$$\overline{\sigma}_{z_{tot}} = \frac{\sigma_{z0} + \sigma_{f_d} + \sigma_{z_d}}{\sigma_{ref}} \qquad \text{Eq. 3.28}$$

Figure 3.11 gives the evolution over time of the axial global stress scaled to the reference stress. It is important to observe that the peak value for the global stress at $r = R$, $\theta = 3\pi/2$ and $\eta = 0.6R$ is roughly six times larger than the reference stress and occurs at a time hundred times longer than the shock duration ($t_f \cong 1ms$ against $\tau \cong 10\mu s$). This gives a valuable indication for the design of accelerator components submitted to thermal shocks.

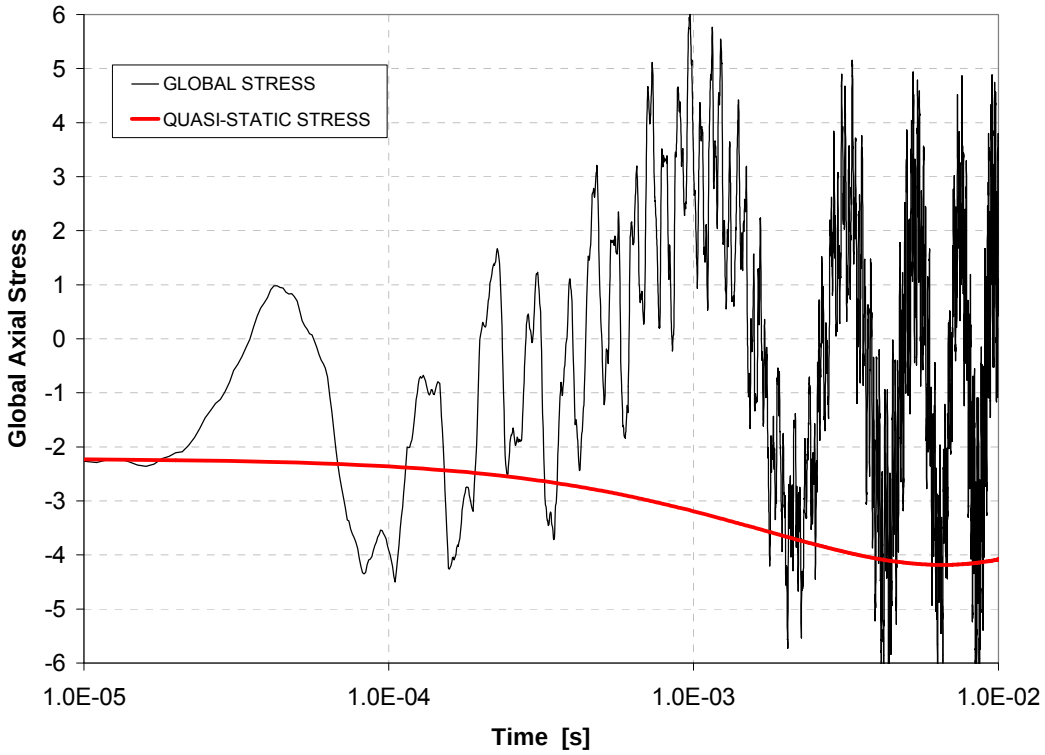

Figure 3.11: Scaled global axial stress $\sigma_{z_{tot}} / \sigma_{ref}$ and quasi-static axial stress $\sigma_{z0} / \sigma_{ref}$ as a function of time at $r=R$, $\theta=3\pi/2$, $\eta=0.6R$ (logarithmic scale).

3.4.6 Discussion on radial inertia effect and weak thermo-elastic coupling

At this point of the analysis, we want to clarify with a brief discussion the initial assumptions of neglecting the influence of radial inertia on the longitudinal dynamic behaviour and of weak thermo-elastic coupling.

For radial inertia, we follow the considerations made by Graff [3.21] . He found that, beyond a limiting working frequency, radial inertia must be considered and the simplified theory of longitudinal wave propagation in cylindrical rods cannot be applied.

Following Graff's notation, we define several non dimensional quantities: velocity of longitudinal wave propagation $\bar{c}$, wave number $\bar{\gamma}$ and pulse frequency $\bar{\omega}$:

$$\begin{aligned} \bar{c} &= \frac{c}{c_0} \\ c_0 &= \sqrt{\frac{E}{\rho}} \\ \bar{\gamma} &= \beta \nu \gamma \\ \bar{\omega} &= \bar{\gamma} \cdot \bar{c} \\ \beta &= \frac{R}{\sqrt{2}} \end{aligned} \qquad \text{Eq. 3.29}$$

Here, β is the radius of gyration of the cylinder, ν is the Poisson's ratio, c is the actual velocity of longitudinal wave propagation and c_0 is the reference value from the classical wave equation.

After some simple manipulations, we obtain:

$$\bar{\gamma} = \frac{\nu \cdot \omega \cdot R}{\sqrt{2} \cdot c} \qquad \text{Eq. 3.30}$$

If $\bar{\gamma} << 1$ the simplified classical theory of wave propagation can be applied and the effects of radial inertia can be neglected.

We can make some remarks on Eq. 3.30: if $\bar{\gamma} << 1$, we can assume $c = c_0$, (as confirmed also by Suhubi [3.26], for the case of infinitely long cylinders), and $\omega = \frac{\pi \cdot c_0}{L}$.

Replacing in Eq. 3.30 we obtain:

$$\frac{\nu \pi}{\sqrt{2}} \cdot \frac{R}{L} << 1 \qquad \text{Eq. 3.31}$$

Since ν can assume values between 0 and 0.5 it is possible to write that:

$$\frac{R}{L} << 1 \qquad \text{Eq. 3.32}$$

If Eq. 3.32 is verified, then the restriction on radial inertia is valid. For the application presented in this chapter $L = 100mm$ and $R = 2.5mm$, so Eq. 3.32 is valid.

Concerning the weak thermo-elastic coupling hypothesis, we follow the study of Boley and Weiner [3.22] showing that this assumption is valid if the strain rate is of the same order of magnitude of the temperature rate.

The coupled thermo-elastic heat conduction equation in indicial notation is given by:

$$K \cdot \nabla^2 T = \rho \cdot c_p \cdot \dot{T} + (3\lambda + 2\mu) \cdot \alpha \cdot T \cdot \dot{\varepsilon}_{kk} \qquad \text{Eq. 3.33}$$

In Eq. 3.33 λ and μ are the Lamé's constants and $\dot{\varepsilon}_{kk}$ is the trace of the strain rate tensor. From Eq. 3.33, neglecting radial and circumferential terms, we immediately obtain the thermo-elastic coupling term Γ; if $\Gamma << 1$ then the weak coupling assumption can be applied:

$$K \cdot \nabla^2 T = \rho \cdot c_p \cdot \dot{T} \cdot (1 + \Gamma)$$

$$\Gamma(r,\theta,z,t) = \left[\frac{(3\lambda + 2\mu) \cdot \alpha \cdot T}{\rho \cdot c_p} \right] \cdot \left(\frac{\dot{\varepsilon}_z}{\dot{T}} \right) \qquad \text{Eq. 3.34}$$

In Eq3.34 $\dot{\varepsilon}_z = \frac{\partial}{\partial t}\left(\varepsilon_{z_d}(z,t) + \varepsilon_{f_d}(z,r,\theta,t)\right)$ is the time derivative of the dynamic axial strain due to flexural and longitudinal oscillations.

Figure 3.12 shows the evolution over time of the thermoelastic coupling term Γ evaluated at $z = L/2$ in the coldest zone of the rod cross-section ($r=R$; $\theta=\pi/2$), where the temperature change rate is small and the strain rate is high; it is possible to observe that the parameter is always much smaller than unity; so the weak coupling assumption is valid, at least in the first milliseconds of the analysis.

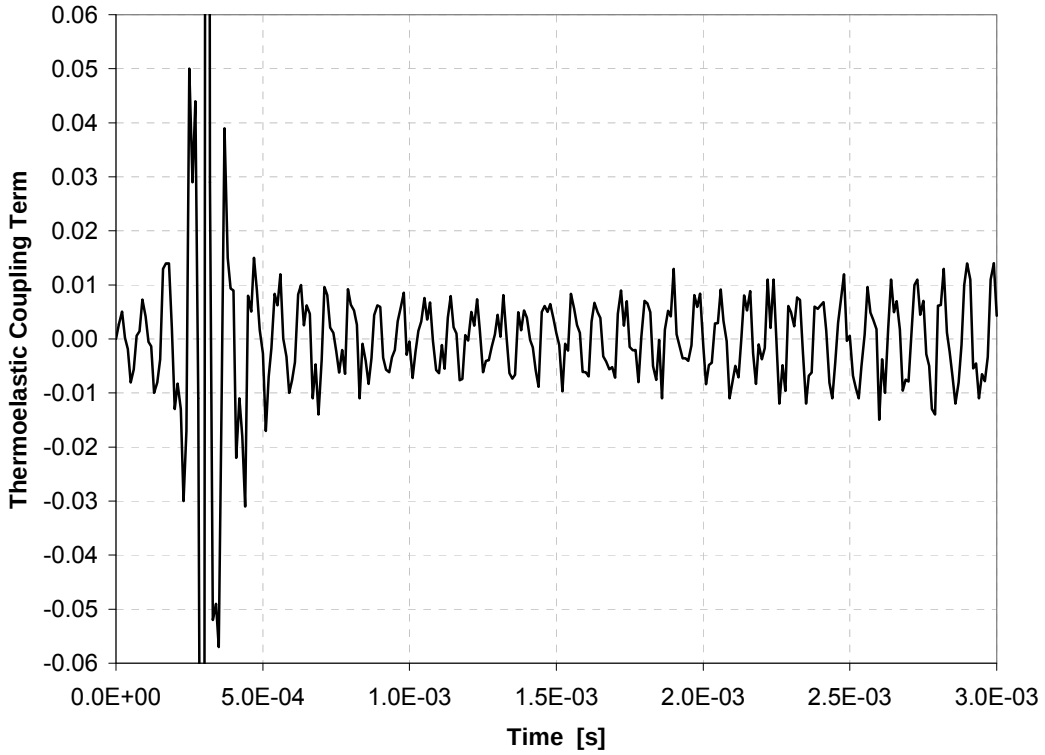

Figure 3.12: Thermo-elastic coupling term as a function of time at r=R, θ=π/2

3.5 Comparison with experimental results

We present here a comparison between the analytical model described in this paper and the experimental measurements performed at CERN on a CNGS target rod hit by a proton beam; material properties as well as rod dimension are listed in Table 2.1, Table 2.3 and Table 3.1. The experimental test exploits the procedure elaborated by Wilfinger [3.20]: a Laser Doppler Vibrometer suitably positioned picks up the lateral velocity of the rod surface at $z = L/2$; the flexural displacement is obtained by integrating the recorded signal.

Figure 3.13 shows the comparison between experimental data and analytical calculation: we can observe that the frequency and the shape of the flexural oscillations of the rod are in very good agreement; the amplitude is scaled with respect to the intensity and position of the proton beam impacting the rod (η, θ, φ and U_{max} are directly dependent on the proton beam parameters). The discrepancy between the curves shown in Figure 3.13 is mainly due to damping, not considered in the analytical model.

Experimental measurements showed that CNGS target rods behaved as if they were completely free at the extremities rather than simply supported, because of mechanical play on the bearings. Flexural dynamic displacement shown in Figure 3.13 has been obtained using expressions for modal shapes and natural circular frequencies derived by Blevins [3.27], instead of those given in Eq. 3.12 and Eq. 3.13.

For a free-free rod, the expressions of the natural circular frequencies and of the modal shapes are as follows:

$$\omega_{fi} = \chi_i^2 \sqrt{\frac{EJ}{mL^3}} \qquad \text{Eq. 3.35}$$

$$\phi_{fi}(z) = \cosh\left(\omega_{fi} \cdot \frac{z}{L}\right) + \cos\left(\omega_{fi} \cdot \frac{z}{L}\right) + - \xi_i \left[\sinh\left(\omega_{fi} \cdot \frac{z}{L}\right) + \sin\left(\omega_{fi} \cdot \frac{z}{L}\right)\right] \qquad \text{Eq. 3.36}$$

In Eq. 3.35, coefficients χ_i can be evaluated numerically if $i < 5$ while $\chi_i = (2i+1)\frac{\pi}{2}$ if $i > 5$. Similarly, in Eq. 3.36, coefficients ξ_i can be evaluated numerically if $i < 5$ and $\xi_i = 1$ if $i > 5$.

By using formulas 3.35 and 3.36, it is possible to obtain the displacement $w(z,t)$ by means of Eq. 3.11. Figure 3.13 shows that the period of flexural oscillation is roughly 1 ms; if we consider the simply supported rod, we can observe a period of flexural oscillation of more than 2 ms as shown in Figure 3.4. The difference is due to the distinct support conditions of the rod.

Table 3.1: CNGS Graphite target rods, mechanical and thermo-physical properties.

Graphite properties	
Young modulus	E = 9.3 GPa
Poisson's ratio	$\upsilon = 0.032$
Coefficient of thermal expansion	$\alpha = 3.9 \cdot 10^{-6}$ °C^{-1}

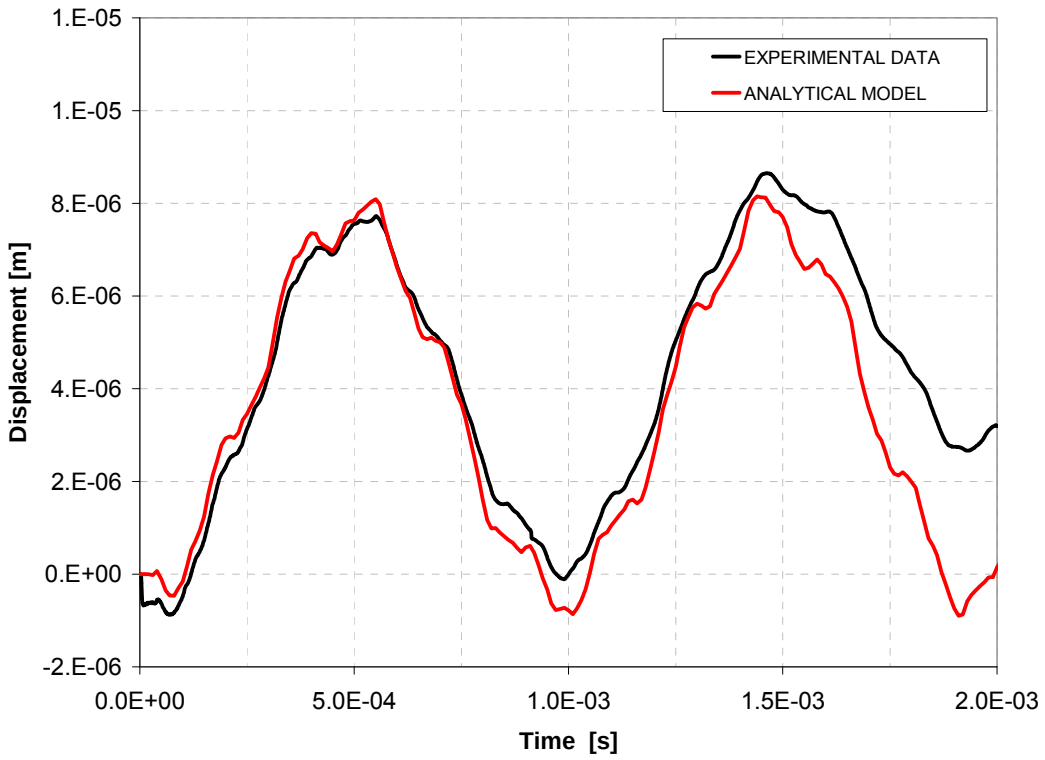

Figure 3.13: Flexural displacement at the rod centre z=L/2; comparison between analytical model and experimental data.

3.6 Summary

The analytical model presented in this chapter allows the complete evaluation, within the linear elastic domain, of quasi-static and dynamic thermal stresses induced in an isotropic cylindrical rod by rapid internal heating.

We have considered a heat deposition constant over the rod length with a Gaussian distribution over the cross-section, which is typically provoked by sub-nuclear particle beams directly impacting the rod. However, the method can be extended to any other problem of thermal shock on cylindrical rods with an arbitrary energy distribution on the cross-section, longitudinally constant.

The approach used in this chapter allows a fast evaluation of the complex stress field induced by thermal shocks acting on isotropic cylindrical rods.

The solution of the problem is divided into three main steps: the evaluation of the temperature distribution as a function of space and time, the evaluation of the quasi-static thermal stress components and the study of the dynamic problem both for the longitudinal and flexural behaviour.

Once the temperature distribution is known, quasi-static stresses have been calculated by means of the thermo-elastic displacement potential, in the plane-strain hypothesis; Airy stress function is also applied to restore the free boundary condition on the lateral surface of the cylinder.

Due to the rapidity of the heat deposition, the inertia effect of the structure cannot be neglected: two equivalent variable loads $F_z(t)$ and $M_x(t)$ applied at the extremities of the rod are introduced to model the effect of the fast non-uniform temperature rise and restore the correct boundary conditions; the response of the system is evaluated by way of the mode-summation method.

The global axial stress can be assessed via the superposition of the quasi-static axial stress at zero-axial strain with the longitudinal and flexural dynamic stresses induced by $F_z(t)$ and $M_x(t)$. An analytical expression has been developed to describe the influence of the thermal shock duration τ on the maximum dynamic longitudinal stress.

The influence of the ratio between thermal and structural characteristic response time (Boley number *B*) on the dynamic maximum deflection has been studied and extended to the case of rapid internal heating: it has been confirmed that *B* is the key parameter for evaluating the dynamic behaviour of a rapidly heated slender structure, however this behaviour depends on the way the heating occurs and on the thermal boundary conditions.

In the last section, a comparison between the analytical model and an experimental measurement is presented; curves show that the analytical calculations give very good prediction of the real behaviour of the structure.

The model developed permits to quickly obtain good estimates of the thermo-elastic behaviour of isotropic rods submitted to thermal shocks. Among other findings, it is worth noting that, for the case of interest, dynamic bending stress can be up to three times larger than the corresponding quasi-static stress.

The results of this study could be usefully applied for the design of slender structures submitted to thermal shocks typically used in particle accelerator technology, but easily extendable to aerospace and nuclear applications.

3.7 Nomenclature

R	Radius of the cylindrical rod
L	Length of the cylindrical rod
r	Radial coordinate
$\bar{r} = r / R$	Non-dimensional radial coordinate
θ	Angular coordinate
$A = \pi R^2$	Cross-section area
$J = \pi R^4 / 4$	Cross-section moment of inertia
ρ	Mass density
$m = \rho A L$	Mass of the rod
E	Young's modulus
ν	Poisson's ratio
α	Thermal expansion coefficient
$\sigma_{ref} = E \alpha T_F$	Reference axial stress
$\overline{\Phi} = \Phi / (E \alpha T_F)$	Non-dimensional Airy Stress Function
$\lambda = \frac{\nu E}{(1+\nu) \cdot (1-2\nu)}$	First Lamé's constant
$\mu = G = \frac{E}{2(1+\nu)}$	Second Lamé's constant
$c_0 = \sqrt{E / \rho}$	Velocity of longitudinal waves (classical wave equation)
K	Thermal conductivity
c_p	Specific heat
$\kappa = K / (\rho \cdot c_p)$	Thermal diffusivity
Γ	Thermoelastic coupling term
U_{max}	Maximum deposited specific energy

η	Eccentricity of the energy distribution w.r.t. the cylindrical rod axis
$\overline{\eta} = \eta / R$	Non-dimensional eccentricity
u_z	Longitudinal displacement
w	Lateral displacement (rod deflection)
z	Longitudinal coordinate
$\overline{z} = z / L$	Non-dimensional longitudinal coordinate
ψ	Displacement potential
$\overline{\psi} = \psi / (\alpha T_F \kappa)$	Non-dimensional displacement potential
q_f	Flexural generalized coordinate for modal analysis
q_z	Longitudinal generalized coordinate for modal analysis
ϕ_z	Longitudinal modal shape
ϕ_f	Flexural modal shape
T	Temperature
T_F	Final uniform temperature
$\overline{T} = T / T_F$	Non-dimensional temperature
t	Time coordinate
$\overline{t} = (t - \tau) / t_d$	Non-dimensional time coordinate
$t_d = R^2 / \kappa$	Thermal diffusion time
τ	Thermal shock duration
$t_0 = 2L / c_0$	Fundamental period of longitudinal vibrations

References

[3.1] B.A. Boley, 1955, Thermally Induced Vibrations of Beams, Journal of the Aeronautical Science, vol. 23, pp. 179-181

[3.2] B.A. Boley, 1972, Approximate Analyses of Thermally Induced Vibrations of Beams and Plates, Journal of Applied Mechanics, vol. 39, pp. 212-216

[3.3] B.A. Boley and A. D. Barber, 1957, Dynamic Response of Beams and Plates to Rapid Heating, Journal of Applied Mechanics, vol. 24, No.3, pp. 413-416.

[3.4] M. Murozono, 1996, Thermally Induced Bending Vibrations of Internally Heated Beams in Air, Journal of Thermal Stresses, vol. 19, pp 649-670

[3.5] J.R. Blandino and E.A. Thornton, 2001, Thermally Induced Vibration of an Internally Heated Beam, Journal of Vibration and Acoustic, vol. 123, pp 67-75

[3.6] D. Burgreen, 1962, Thermoelastic Dynamics of Rods, Thin Shells, and Solid Spheres, Nuclear Science and Engineering, vol. 12, pp. 203-217

[3.7] D. Burgreen, 1967, Thermoelastic Dynamics of a Pulse Reactor, Nuclear Science and Engineering, vol. 30, pp. 317-327

[3.8] H. Bargmann, 1973, Dynamic Response of External Targets Under Thermal Shock, CERN Technical Note, Lab. II/BT/Int/73-3, CERN, Geneva

[3.9] P. Sievers, 1974, Elastic Stress Waves in Matter due to Rapid Heating by an Intense High-energy Particle Beam, CERN Technical Note, Lab. II/BT/74-2, CERN, Geneva

[3.10] M. Lessen, 1956, Thermoelasticity and Thermal Shock, Journal of the Mechanics and Physics of Solids, vol. 5, pp 57-61

[3.11] M. Lessen, 1959, Thermoelastic Waves and Thermal Shock, Journal of the Mechanics and Physics of Solids, vol. 7, pp 77-84

[3.12] P. Chadwick, I. N. Sneddon, 1958, Plane Waves in an Elastic Solid Conducting Heat, Journal of the Mechanics and Physics of Solids, vol. 6, pp 223-230

[3.13] P. Chadwick, 1962, On the Propagation of Thermoelastic Disturbances in Thin Plates and Rods, Journal of the Mechanics and Physics of Solids, vol. 10, pp 99-109

[3.14] H. Bargmann, 1974, Recent Developments in the Field of Thermally Induced Waves and Vibrations, Nuclear Science and Design, vol. 27, pp. 372-385

[3.15] K. Elsener, 2000, General Description of the CERN Project for a Neutrino Beam to Gran Sasso (CNGS), CERN AC note 2000-03, CERN, Geneva

[3.16] T. Mura, 1956, Dynamical Thermal Stresses due to Thermal Shock, Research Reports of the Faculty of Engineering, Meiji University, No. 8, (2)

[3.17] A. Bertarelli, 2003, An Analytical Model to study Transient Thermal Stresses in Graphite Target Rods hit by Off-axis Beam for CNGS Facility, Technical Note EST-ME-2003-06, CERN, Geneva

[3.18] A. Bertarelli and T. Kurtyka, 2004, Dynamic Thermo-Mechanical Phenomena Induced in Isotropic Cylinders Impacted by High Energy Particle Beam. In N. Jones, C.A. Brebbia (Eds.), Proceedings of the VIII International Conference on Structures Under Shock and Impact (SUSI), Wessex Institute of Technology, 33-43

[3.19] A. Dallocchio, A. Bertarelli, T. Kurtyka, 2006, A New Analytical Method to Evaluate Transient Thermal Stresses in Cylindrical Rods Hit by Proton Beams, Proceedings of the 10th European Particle Accelerator Conference (EPAC06), Edinburgh, Scotland

[3.20] R. Wilfinger, 2005, Proton-Induced Thermal Stress-wave Measurements for ISOLDE and CNGS, PhD Thesis, Vienna University of Technology, Atominstitut of the Austrian Universities, Vienna, and CERN, Geneva

[3.21] K. F. Graff, 1991, Wave Motion in Elastic Solids, Dover Publications, New York, pp. 116-121

[3.22] B.A. Boley, J.H. Weiner, 1997, Theory of Thermal Stresses, pp 30-44, Dover Publications, New York

[3.23] J.N. Goodier, 1937, On the Integration of the Thermo-Elastic Equations, Phil. Mag. (7th series), 23, pp. 1017-1032.

[3.24] S. Timoshenko, J.N. Goodier, 1970, Theory of Elasticity, 3rd ed., McGraw-Hill Book Company, New York, , pp. 476-481, 132-135

[3.25] W.T. Thomson, 1993, Theory of Vibration with Applications, 4th ed., Chapman & Hall, London, pp. 100-101, 345-349

[3.26] E. S. Suhubi, 1964, Longitudinal Vibrations of a Circular Cylinder Coupled with a Thermal Field, Journal of the Mechanics and Physics of Solids, vol. 12, pp 69-75

[3.27] R.D. Blevins, 2001, Formulas for Natural Frequency and Mode Shape, Krieger Publishing Company, Malabar Florida, pp. 107-108

Part III

NUMERICAL METHODS

Chapter 4

LHC Collimators

4.1 Introduction

The third part of the thesis deals with the numerical models, based on the Finite Element Method, developed for the analysis of complex systems. Analytical methods have proven useful to quickly obtain solutions in case of beam-like structures, however, if the geometry is more complicated, the numerical approach is highly necessary. Furthermore, the analytical solutions described in the second part of this dissertation are only valid in the linear elastic domain of the material and isotropic material models have been only considered. Thus it is clear that implementation of a numerical approach is needed, that could be used for the simulation of complex accelerator devices in several working conditions taking into account geometrical and material non-linearity as well as multi-component systems where contact interfaces play an important role for the accuracy of thermo-structural analyses. Particle accelerator structures having interaction with high energy particle beams should typically undergo thermal loads with different time-scales; this can be translated, from a thermo-mechanical point of view, into different load cases: steady-state, slow transient and fast dynamic. This is the case of the LHC Collimators; as discussed in the introduction, these particular devices must be placed near to the particle beam thus being submitted to high thermal loads. The study of these complex structures gave the opportunity to directly apply to an actual case the numerical methods developed. This chapter is dedicated to the presentation of the LHC collimation system and of the mechanical design of collimators.

4.2 LHC collimation system

As discussed in the second part of this thesis, particle beams have a cross-section that could be described as a two-dimensional Gaussian distribution. Particles belonging to the external halo of the Gaussian function could escape from the proper trajectory thus hitting some sensible equipments.

Furthermore, each of the two LHC rings will handle a stored beam energy of up to 360 MJ ($3 \cdot 10^{14}$ protons at 7 TeV), two orders of magnitude beyond the achievements in the Tevatron or HERA [4.1] (see Figure 4.1). Comparing transverse energy densities, LHC advances the state of the art by even three orders of magnitude, from 1 MJ/mm^2 to 1 GJ/mm^2. This makes the LHC beams highly destructive. At the same time the superconducting magnets in the LHC would quench at 7 TeV if small amounts of energy (on the level of 30 mJ/cm^{-3}, induced by a local transient loss of $4 \cdot 10^7$ protons) are deposited into the superconducting magnet coils [4.2]. For these reasons a collimation system is essential for the proper functionality of the LHC.

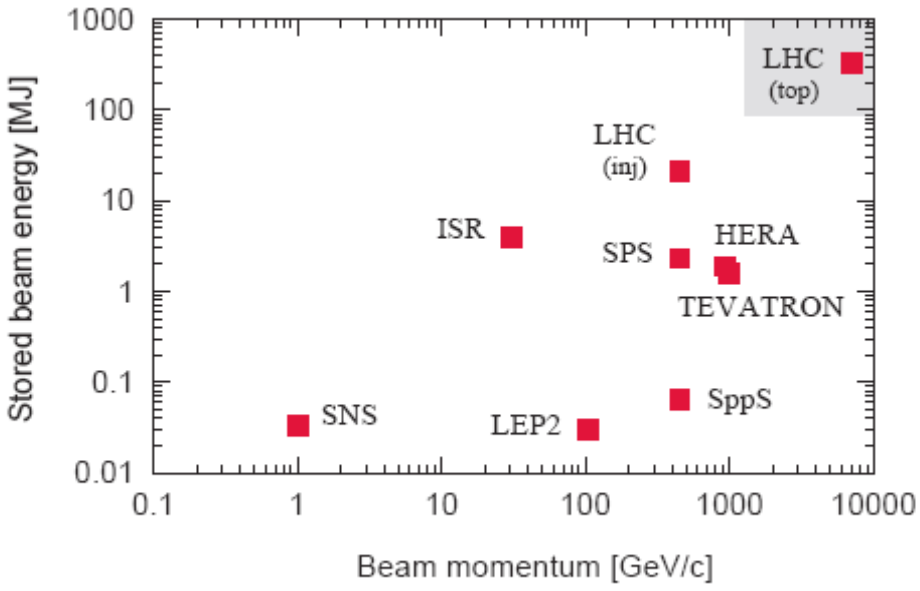

Figure 4.1: Stored beam energy in different proton colliders versus the beam momentum.

Collimators are particular devices that, placed closed to the beam, intercept and stop particles of the external halo as shown in the schema of Figure 4.2. Moreover, in case of accident scenarios, when the high energy beam is out of control, collimators are strategically positioned in order to absorb the particle impact thus preserving other critical structures like the superconducting magnets.

LHC collimation system is made up of several collimators placed all along the LHC rings, having the two essential functions of *beam cleaning* and *machine protection* [4.3] [4.4]. LHC Collimators are the closest elements to the proton beams, thus they are submitted to high thermal loads in several working conditions; an in-depth thermo-mechanical analysis was essential for the achievement of the objectives of the project.

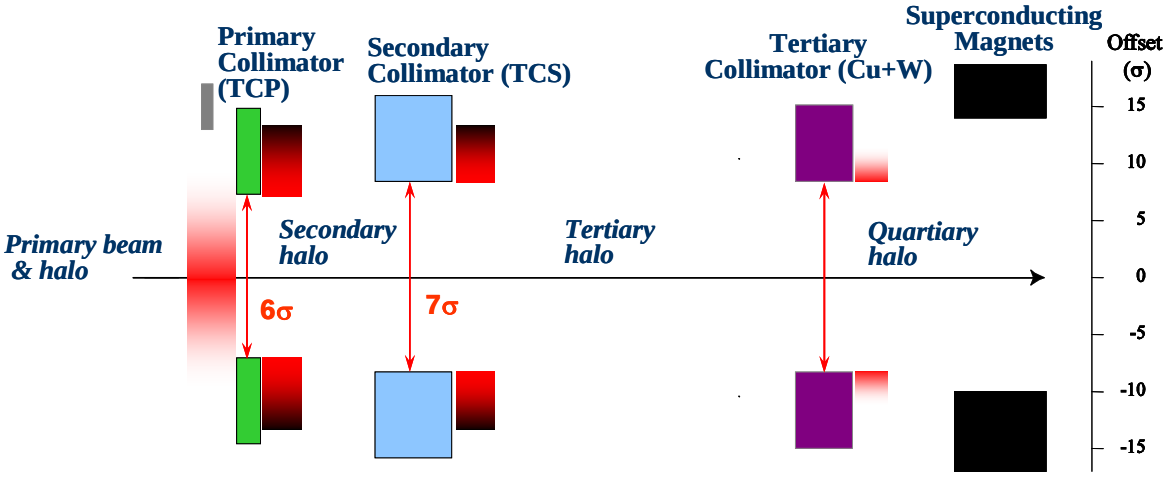

Figure 4.2: Qualitative scheme of the LHC collimation system

4.3 Mechanical design of LHC collimators

4.3.1 General Layout

LHC collimators, as shown in Figure 4.3, are made up of a support on which the vacuum tank and the actuation mechanism are positioned thanks to a plug-in system; particle beam enters longitudinally into the vacuum tank through the connections at the extremities (see Figure 4.3 and Figure 4.4).

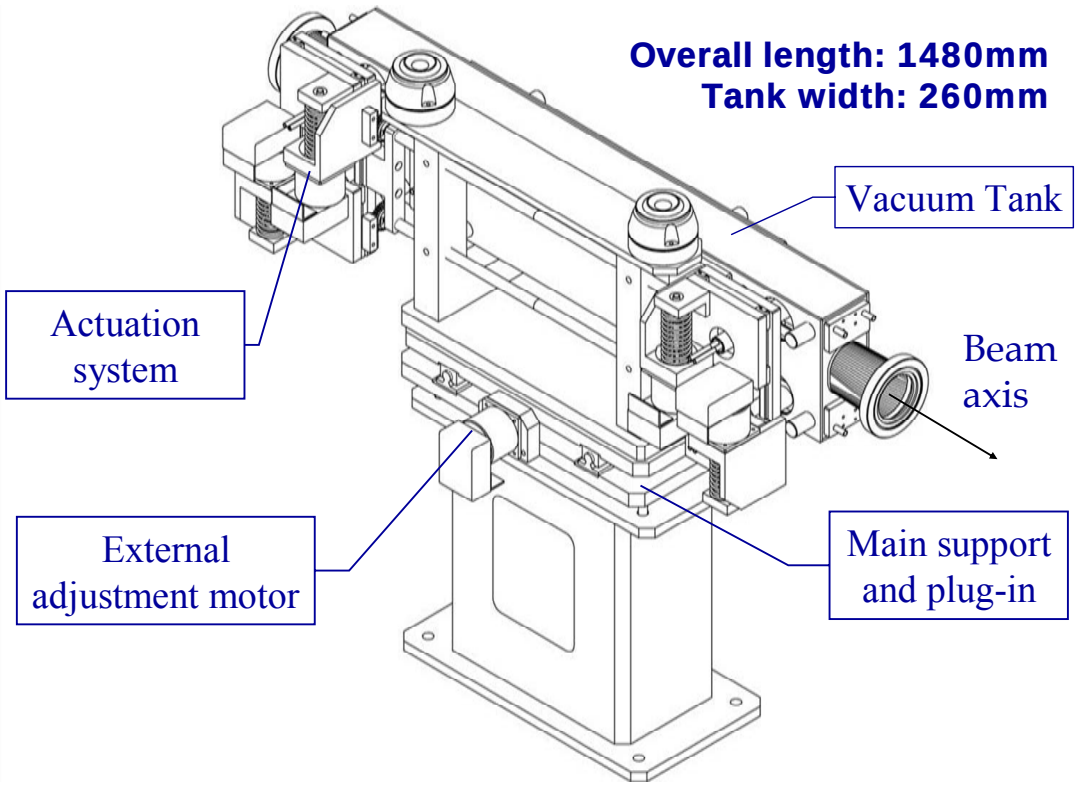

Figure 4.3: 3D CAD assembly of a full LHC collimator on its support.

Inside the vacuum tank there are the two collimation jaw assemblies, core of the system, these are the components having direct interaction with particle beams (see Figure 4.5 and Figure 4.6). In nominal working condition particle beam grazes jaw assemblies with its external halo; actuation system assure the alignment of the jaws with an high precision. Figure 4.7 shows more in detail how the jaw assemblies are supported at the extremities by two shafts that transmit the movement given by the actuation system.

Figure 4.8 shows the different layouts of collimators that can be installed in vertical, horizontal and skew configuration in order to ensure a complete cleaning all around the particle beam axis.

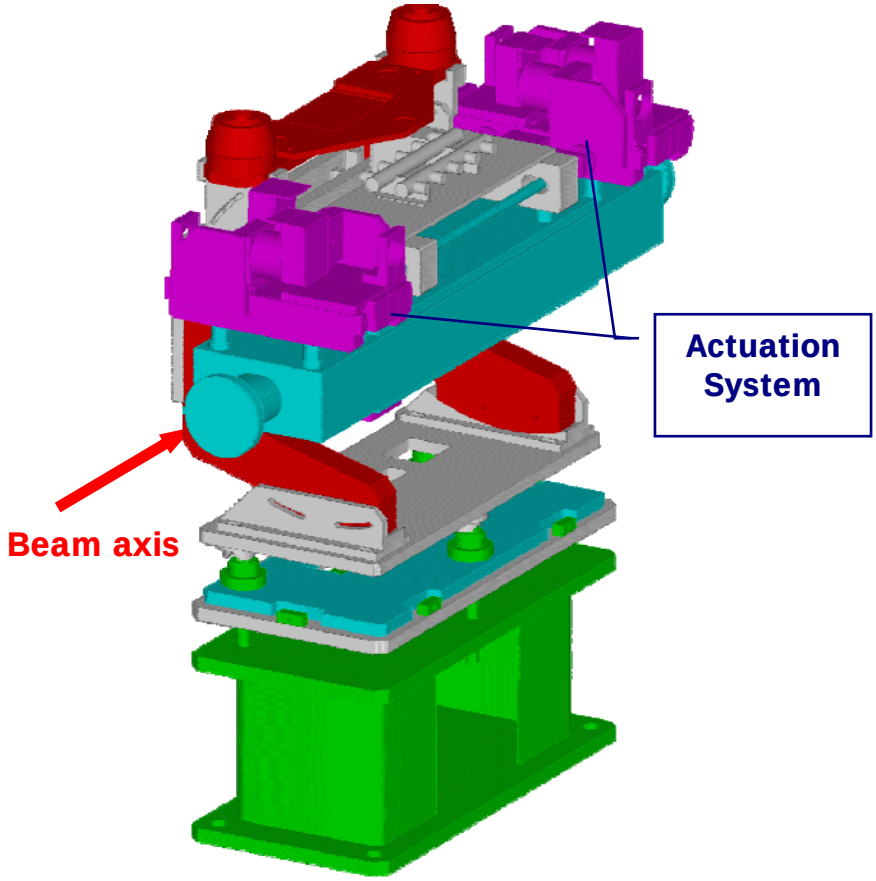

Figure 4.4: 3D CAD drawing of .a full LHC collimator. The green part is the support, the light blue one is the vacuum tank while the actuation system is in magenta.

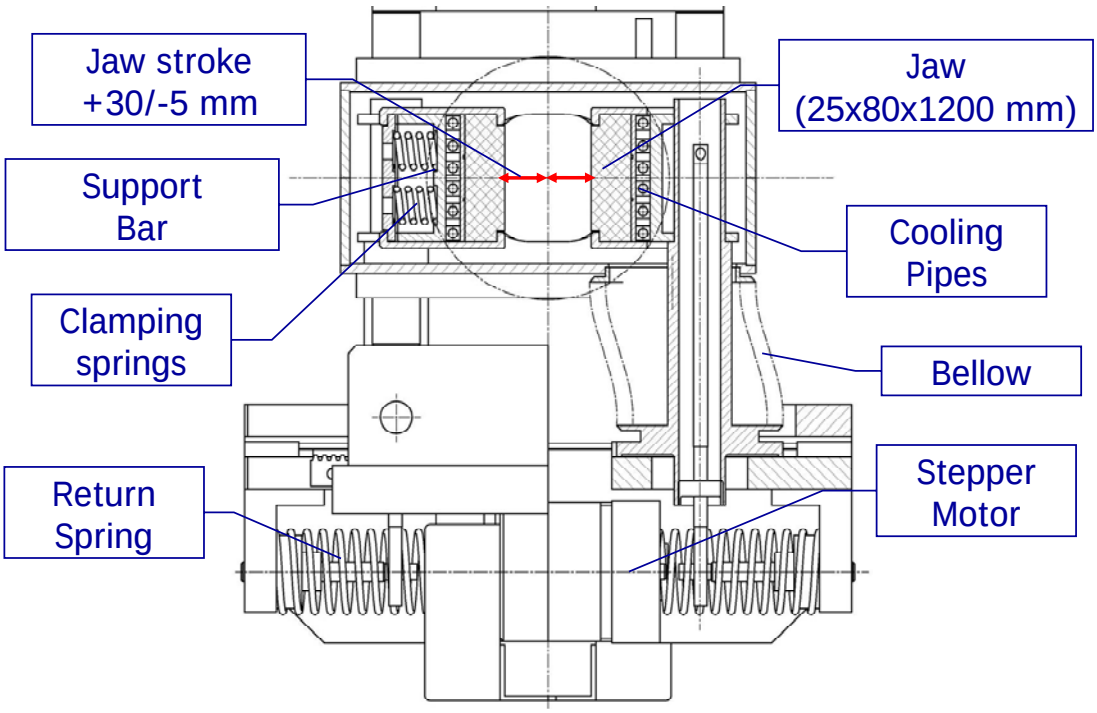

Figure 4.5: Front view of an LHC collimators with the actuation system and the two jaw assembly.

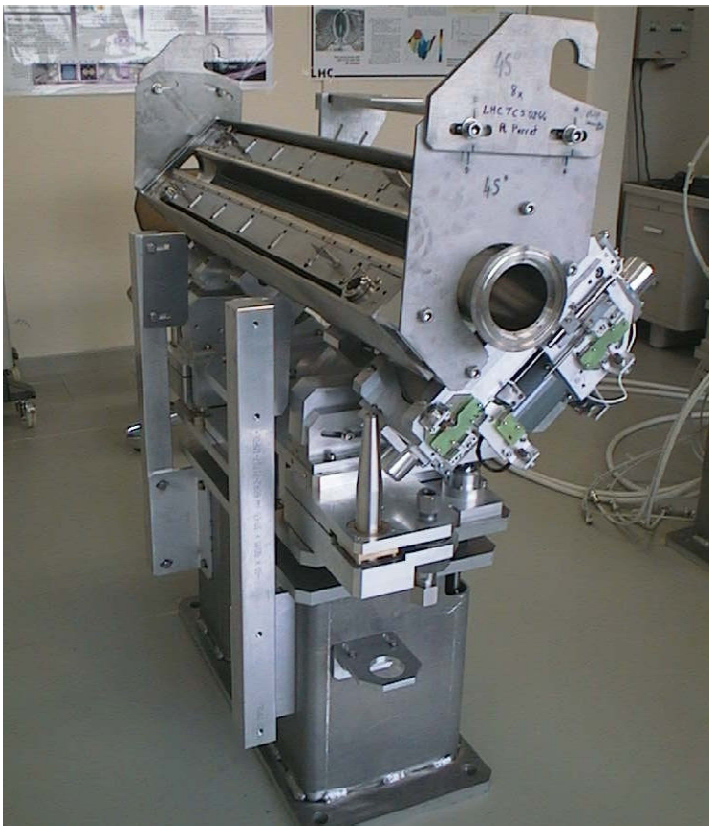

Figure 4.6: Picture showing the real structure on its support. Vacuum tank is opened exhibiting the two collimation jaw assemblies.

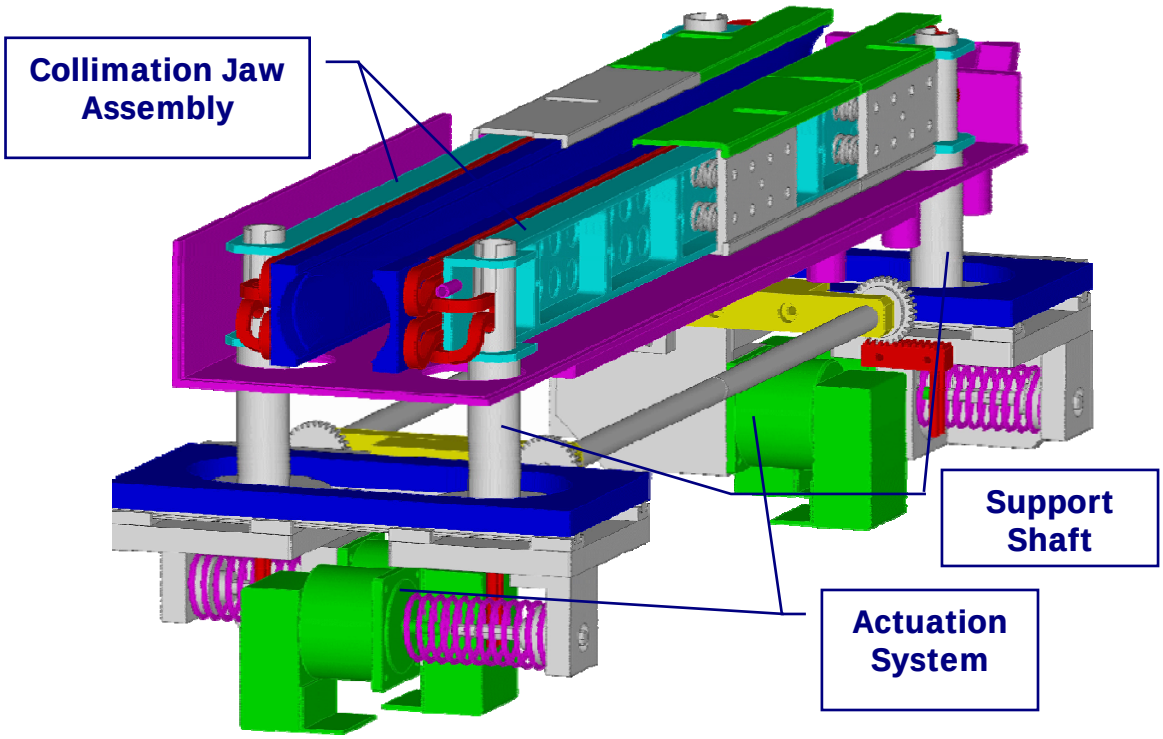

Figure 4.7: Cutaway of an LHC collimator: Jaw assemblies, enclosed in the vacuum tank, are supported at the extremities by two shafts transmitting the movement given by the actuation system

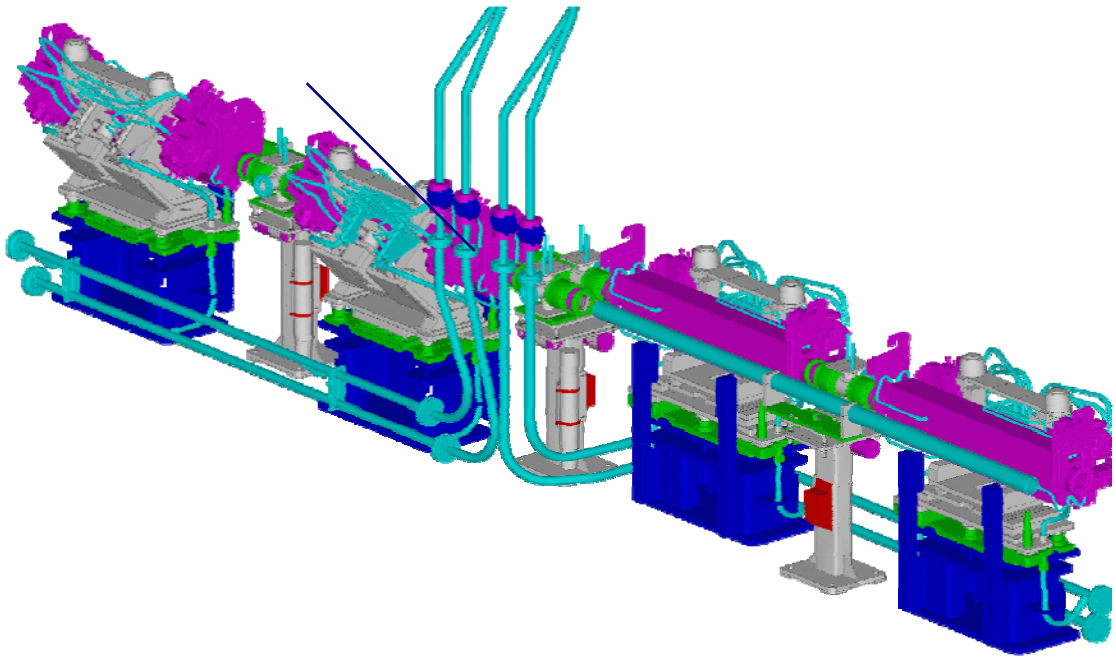

Figure 4.8: Collimators can be installed in the LHC ring with different orientations (vertical, horizontal and skew) in order to clean the full beam orbit.

4.3.2 Collimation jaw assembly

Let us present more in detail the collimation jaw assembly, core of the system, and object of the thermo-mechanical analyses that will be presented in next chapters. Jaw assembly can be considered as a beam with an almost squared cross-section (Length: 1200 mm; Side: 80 mm). With reference to Figure 4.9 and Figure 4.10 it is possible to describe the various component of the assembly:

1. *Collimation jaw* (that will be hereinafter indicated only as *jaw*) is the component having direct interaction with the particle beams thus receiving the thermal load. The jaw is a beam with an almost rectangular cross-section and it is made up of a 2D Carbon-Carbon composite.
2. *Support beam* is the element that gives the structural support to the jaw assembly; it has a C-shaped cross-section with a sequence of ribs disposed over the length and it is simply supported at the extremities. This component is made up of Alumina strengthened copper.
3. *Cooling circuit* is essential for the evacuation of the heat deposited on the jaw. It is made up of pipes with an internal circular cross-section and an external squared shape. A 3 mm thin plate is placed between the cooling pipes and the jaw in order to create a good contact interface with the jaw. Cooling pipes are made up of Copper-Nickel alloy while the contact plate is made up of alumina strengthened copper.
4. *Counter-plates* are part of the clamping system that exploits the force given by preloaded spring in order to assure a contact pressure between the jaw and the contact plate of the cooling system. Counter plates are made up of stainless steel.
5. *Clamping plates* are part of the clamping system being the elements that keep together all the jaw assembly; they are made up of alumina strengthened copper.
6. *Springs* are placed with a certain preload between the support beam and the counter-plates in order to assure a good contact pressure between the jaw and the cooling system. Spring are made up of stainless steel.

For a better understanding it is important to explain that main support beam, cooling pipes and contact plate are brazed together thus creating a single body. Given the large difference between thermal expansion coefficients of carbon-carbon composite and alumina strengthened copper, in order to avoid large thermal deformations, it was not possible to braze the jaw on the contact plate of the cooling system. Nevertheless the clamping system, exploiting the force of preloaded springs, ensure a good contact pressure between the jaw and the cooling system; thanks to this pressure it is possible to obtain a good thermal contact conductance so that the heat deposited on the collimation jaw could be efficiently evacuated by the cooling system.

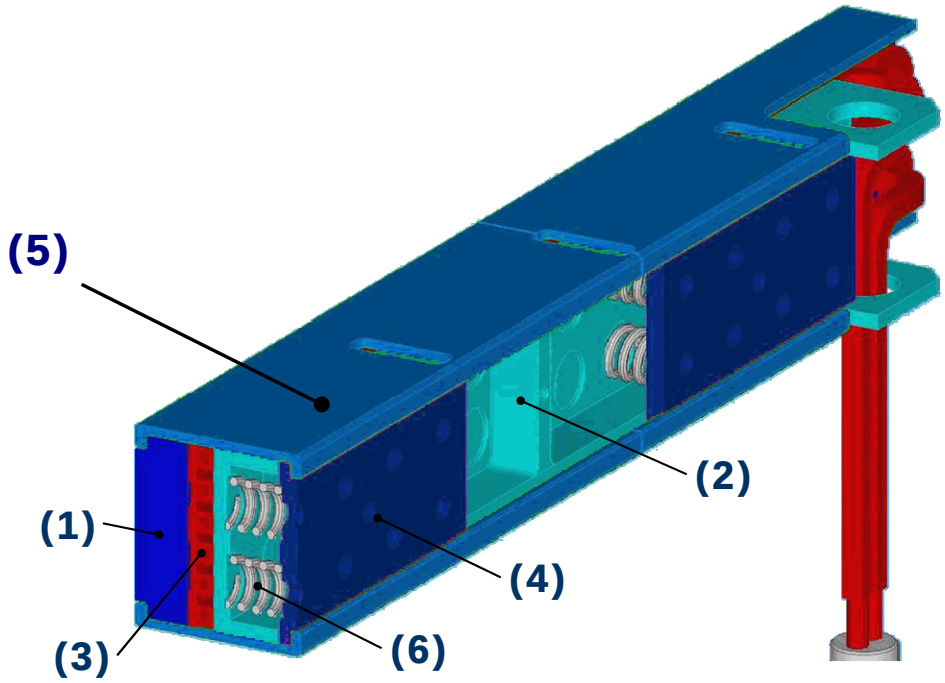

Figure 4.9: Cutaway of a jaw assembly

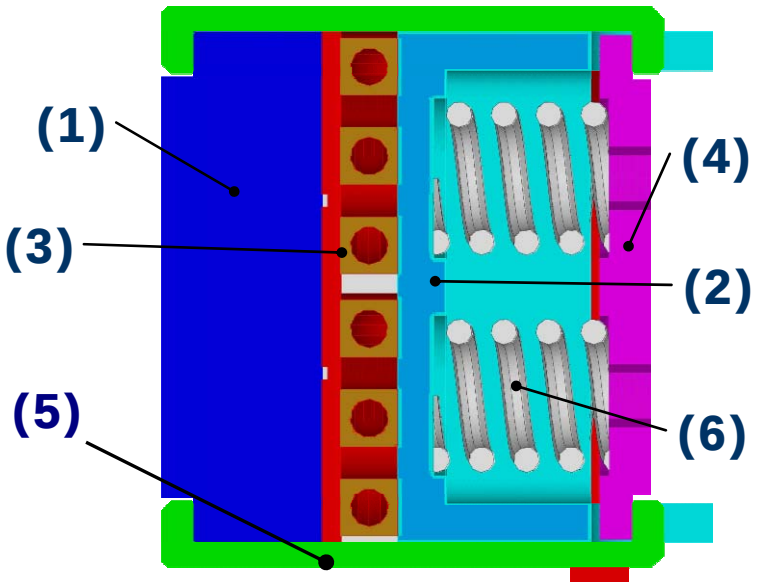

Figure 4.10: Cross-section of the jaw assembly

Figure 4.11: Picture showing a complete jaw assembly ready to be installed inside a vacuum tank. It is possible to see the tapering at the ends of the Carbon-Carbon jaw.

4.3.3 Materials

In this paragraph, thermo-physical and mechanical properties of materials are discussed giving a motivation for the choice of each material [4.5].

- *Carbon-Carbon composite*. Collimator jaws are the most important components of the whole collimation system; the jaw has direct interaction with the high energy LHC beams, thus being submitted to intense thermal loads both in nominal working conditions as well as in case of accident scenario as will be later discussed. Carbon-Carbon composite has been chosen for its good resistance to high temperature thermal shocks and also for its low coefficient of thermal expansion that ensure a high geometrical stability as required by the design specifications that will be discussed in the next paragraphs. The material is a 2D composite with short carbon fiber in a graphite matrix. Carbon fibres are randomly disposed to create a layer in the YZ plane; several layers are bundled over the thickness in the X directions. In this way it is possible to obtain an orthotropic material with equal properties in the layer plane YZ and a different behaviour in the X direction transversal to the layers (see Figure 4.12). In Table 4.1 are collected thermo-physical and mechanical properties of carbon-carbon; all data have been experimentally measured as a function of temperature in a range from room temperature to 1000 °C, here we report only values at room temperature.
- *Alumina Dispersion Strengthened Copper*. This material, which commercial name is GLIDCOP, is widely used for high temperature applications. It has the same properties of copper in terms of thermal and electrical conductivity but with an higher yield strength. Furthermore the good mechanical properties are retained also to high temperature and the material does not suffer of thermal softening. This is a very important characteristic knowing that collimator jaw assembly must be submitted to a bake out process at high temperature before being installed inside the tank in order to respect the constraint imposed by the ultra-high vacuum. In Table 4.2 are collected thermo-physical and mechanical properties of GLIDCOP. Figure 4.13 shows the experimental characterization of the elastic-plastic stress-strain characteristic of the material.

- *Copper–Nickel alloy*. This material has been chosen for the cooling pipes for its good resistance to the corrosion provoked by the water cooling thus maintaining a good thermal conductivity. In Table 4.3 are collected thermo-physical and mechanical properties of Cu-Ni alloy.
- *Stainless steel*. standard stainless steel 304L has been used for springs and counter-plates because these components are not submitted to high thermal loads, so thermal conductivity does not play an important role in this case. In Table 4.4 are collected thermo-physical and mechanical properties of stainless steel.

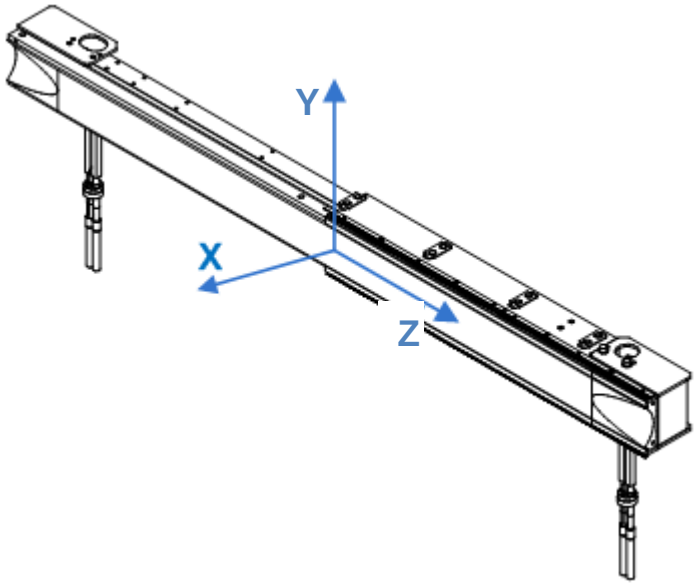

Figure 4.12: 3D CAD drawing of a jaw assembly. The coordinate system is taken as a reference for the identification of the orthotropic material properties of the carbon-carbon jaw.

Table 4.1: Thermo-physical and mechanical properties of 2D Carbon-Carbon composite AC150

Carbon-Carbon composite	AC150		
Young Modulus	E_{XX}=5 GPa	E_{YY}=77 GPa	E_{ZZ}=77 GPa
Shear modulus	G_{XY}=2.98 GPa	G_{XZ}=2.98 GPa	G_{YZ}=33 GPa
Poisson's ratio	υ_{XY}=0.158	υ_{XZ}=0.158	υ_{YZ}=0.165
Density	1656 kg/m^3	1656 kg/m^3	1656 kg/m^3
Coefficient of thermal expansion	α_X=8.75·10^{-6} °C^{-1}	α_Y= -1.55·10^{-6} °C^{-1}	α_Z= -1.55·10^{-6} °C^{-1}
Thermal conductivity	K_X=68 W/m°K	K_Y=218 W/m°K	K_Z=218 W/m°K
Specific heat	780 J/kg°K	780 J/kg°K	780 J/kg°K

Table 4.2: Thermo-physical and mechanical properties of Alumina Dispersion Strengthened Copper (GLIDCOP)

Young Modulus	120 GPa
Poisson's ratio	0.343
Coefficient of thermal expansion	$16.6 \cdot 10^{-6}$ °C^{-1}
Density	8840 kg/m^3
Thermal conductivity	365 W/m°K
Specific heat	385 J/kg°K

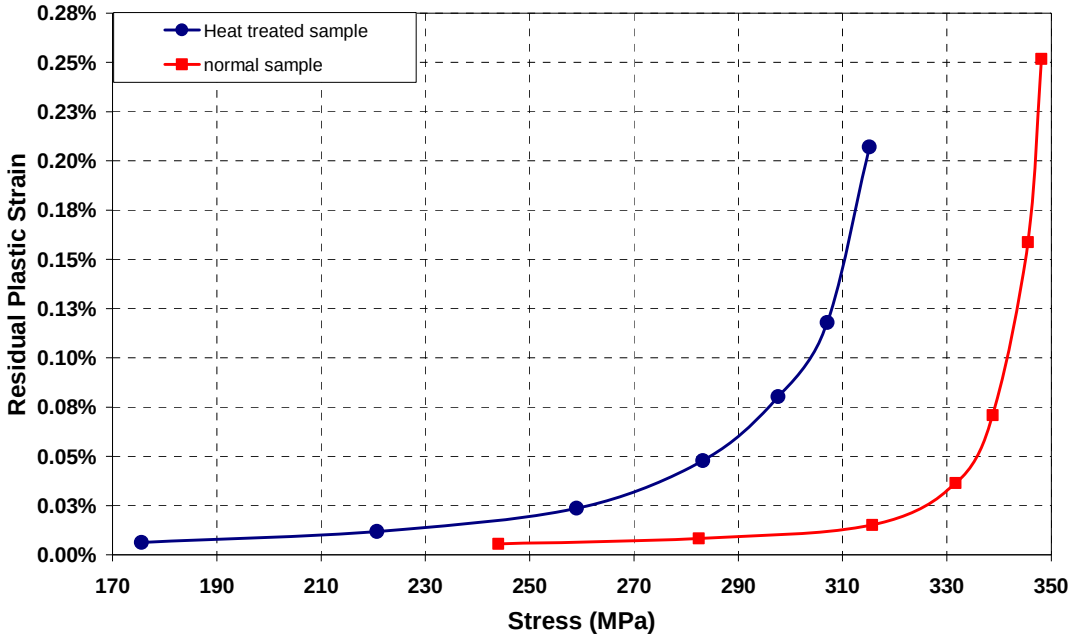

Figure 4.13: Alumina Dispersion Strengthened Copper (GLIDCOP). Experimental characterization of the elastic-plastic stress-strain curve considering different samples with and without the heat treatment.

Table 4.3: Thermo-physical and mechanical properties of Copper-Nickel alloy

Young Modulus	135 GPa
Poisson's ratio	0.345
Coefficient of thermal expansion	$17 \cdot 10^{-6}$ °C^{-1}
Density	8900 kg/m^3
Thermal conductivity	50 W/m°K
Specific heat	377 J/kg°K

Table 4.4: Thermo-physical and mechanical properties of Stainless Steel

Young Modulus	200 GPa
Poisson's ratio	0.29
Coefficient of thermal expansion	$16.6 \cdot 10^{-6}$ °C^{-1}
Density	7900 kg/m^3
Thermal conductivity	16.3 W/m°K
Specific heat	500 J/kg°K

4.3.4 Load Cases

Different working conditions have been foreseen for the LHC collimation system (see [4.6] depending on particle beam losses. Load cases can be classified into normal and abnormal processes.

In normal working condition the so-called "primary beam halo" [4.6] will continuously be filled by various particle beam dynamics processes in a way that the beam life time will have a finite duration. In other words collimator jaws continuously interact with particles belonging to the external beam halo; this gives origin to a steady state thermal load deposited on the jaws. Another normal load case foresees that, starting from a normal situation, as a consequence of an error in beam dynamics control, an increasing of the beam loss took place. From a thermo-mechanical point of view this second nominal load case entails that, starting from a normal proton loss condition, the energy deposition increases of a factor 5 over a transient period of ten seconds. After 10s the normal condition will be recovered.

In case of accident scenarios, abnormal beam loss processes must be taken into account; in these cases particle beam impacts occur on the collimator jaws and very fast energy deposition provoke thermo-mechanical dynamic response of the system.

Table 4.5 and Table 4.6 contains a resume of the parameters of the various load cases.

Table 4.5: Nominal working condition of LHC collimators. T is the duration of the process, τ is the corresponding beam life time, R_{loss} is the proton loss rate and P_{loss} is the power deposited on the structure

Nominal Load Cases	T[s]	τ[h]	R_{loss}[p/s]	P_{loss}[kW]
Steady–State	continuos	1	$0.8 \cdot 10^{11}$	6
Transient	10	0.1	$4 \cdot 10^{11}$	30

Table 4.6: Accident scenarios of LHC collimators: direct beam impacts entail that a large amount of energy is deposited on the structure very rapidly. This table collects parameters of heat loads in case of abnormal beam losses.

Accident Cases	Beam Energy [TeV]	Beam Intensity [protons]	Energy Deposit [kJ]	Impact duration [ns]
Injection Error	0.45	$3.2 \cdot 10^{13}$	2073	7200
Asynchronous Beam Dump	7	$9.1 \cdot 10^{11}$	1021	200

4.3.5 Functional Requirements

The design of the LHC collimators must comply with the very demanding specifications [4.7] resulting from the highly energetic beam handled in the LHC. These requirements impose that temperature on the collimating jaws does not exceed a certain value in nominal steady-state operations in order to avoid possible problem of outgassing of the carbon-carbon jaws according to the requirements of ultra high vacuum. Moreover, given the typical particle beam transverse dimensions of the order of some tenth of millimeter, it is important to obtain a high geometrical stability of the jaws limiting as much as possible thermal deformations. Finally high robustness in case of accident scenarios is also required: collimators must survive to proton beam impacts keeping their correct functionality.

These are the design requirements:

- *Temperature*. In nominal steady state condition temperature increase on the collimation jaws does not exceed the limit of 50 °C
- *Geometric Stability*. In nominal steady-state condition the deflection of collimator jaws due to thermal loads must not exceed the limit of 40 μm over a length of 1200 mm of the whole jaw assembly.
- *Robustness*. LHC collimators must survive to particle beam impacts in case of accident scenarios.

4.4 Summary

The overview of the LHC collimation system presented in this chapter is a useful introduction to better understand the study of thermo-mechanical phenomena, based on a numerical approach, that will be presented in the next chapters. Numerical methods developed to evaluate thermo-structural effects provoked by high energy particle beams found an important application for the study of LHC collimators.

Solution of thermo-mechanical problems require different approaches depending on different load conditions. Two different methods have been developed and will be presented in Chapter 5 and chapter 6: the first one is applied to the case of nominal working conditions, the second one is useful to simulate the accident scenarios in case of particle beam impacts.

References

[4.1] LHC Design Report, Vol. I, Chapter 2, Beam Parameters and Definitions, 2004

[4.2] J.B. Jeanneret, D. Leroy, L. Oberli and T. Trenkler. LHC Project Report 44 (1996).

[4.3] LHC Design Report, Vol. I, Chapter 18, Beam Cleaning and Collimation System, 2004.

[4.4] R. Aßmann, O. Aberle et al. "Designing and Building a Collimation System for the High Intensity LHC Beam", CERN-LHC-Project-Report-640, 2003.

[4.5] P. Sievers, O. Aberle, R. Aβmann, L. Bruno, A. Ferrari, V. Vlachoudis, "Appropriate Materials for LHC-Collimators", LHC Performance Workshop-Chamonix XII, 2003.

[4.6] LHC Design Report, Vol. I, Chapter 18, Beam Cleaning and Collimation System, 2004

[4.7] R. Aßmann, et al. "Requirements for the LHC Collimation System", CERN-LHC-Project-Report-599, 2002.

Chapter 5

FEM approach for the analysis of steady-state and slow transient thermal loads

In this chapter we present a numerical FE approach useful to evaluate thermo-structural effects provoked by high energy particle beams in case of steady-state or slow transient thermal loads, with no dynamic response of the structure. This method has been successfully applied to the study of the LHC collimators, thus showing the capability of the developed approach to give reliable results. Finite Element models have been implemented using commercial code ANSYS [5.1].

A numerical FEM approach, complementary to the analytical solutions presented in the second part of this thesis, is essential for the study of complex structures, multi-component system with contact interfaces and all problems wherein material and geometric non-linearity have a strong influence on the results.

Energy deposition due to the interaction between particle beams and solids can be evaluated via a statistical code FLUKA based on the Monte-Carlo method [5.2]; results of this type of simulations are used as input for the thermo-mechanical analyses - object of this dissertation. Once thermal loads are defined, the numerical models allow the evaluation of temperature distribution as well as the calculation of thermal stresses and deformations.

Particular attention is paid to the study of multi-component systems: in these problems the effect of contact interfaces plays a major role and influences the accuracy of the results. Furthermore, as will be later explained more in details, the presence of contact interfaces implies a coupling between thermal and structural problems such that a dedicated algorithm of solution must be used.

In particular, for the case of the LHC collimators, the attention is focused on the geometrical stability of the structure with the aim of minimize thermal deformations, as required by design specifications described in chapter 4.

The evaluation of thermal deformations of the order of micrometers on structures with a longitudinal dimension of more than one meter requires a detailed and accurate model. Thermo-mechanical contact algorithm will be described; furthermore, the numerical method has been experimentally validated and the comparison between numerical results and experimental measurements will be shown.

Finally, a brief description of the design optimization performed on the base of the numerical results will be presented.

5.1 Introduction

Thermo-mechanical phenomena due to quasi-static and slow transient thermal loads do not include dynamic response of the structure, thus the effect of the inertia can be neglected and other aspects must be considered with respect to the ones described in the second part of this thesis.

As discussed in the third chapter, the weak thermo-elastic coupling hypothesis [5.3] is valid if the strain rate is of the same order of magnitude as the temperature rate; this is true in case of quasi-static and slow transient thermal loads. Upon this assumption, thermal and structural problems can be generally separated and sequentially solved: once temperature distribution is known it can be used as input for the structural analysis in order to evaluate thermal stresses and deformations.

This simple procedure cannot be usually applied to the case of multi-component structures with contact surfaces. It is well-known that the heat flow crossing a contact interface depend on thermal contact conductance which, in turn, is a function of the contact pressure. Finally it is simple to understand that there is a mutual influence between temperature distribution due to thermal loads and structural deformations: temperature distribution provokes thermal deformation of the structure, while the deformation has influence on the contact pressure at the interfaces, thus modifying the thermal contact conductance and, as a consequence, also the temperature distribution is influenced.

For this type of problems the weak coupling hypothesis is still valid but thermal and structural analysis cannot be separated and must be solved with a coupled

approach. An example dedicated to thermo-mechanical FEM analysis of LHC collimator jaw assembly will be shown in the next paragraphs.

5.2 Finite Element model of collimator jaw assembly

A 3D Finite Element model of the LHC collimator jaw assembly has been developed (see Figure 5.1). In this model it has been important to find a good compromise between a detailed geometry, similar to the real structure, and possible simplifications aimed to obtain a regular mesh and, as a consequence,. a reduction of time of calculation. Comparison between Figure 5.1 and Figure 5.2 shows that the structure has been modeled in details.

Carbon-carbon jaw has tapered ends (see Figure 5.3) that are not included in the model; in fact the jaw assembly was modeled only between the two support shafts (see Figure 4.7). This simplification does not affect the accuracy of the results because tapered extremities of collimation jaws do not have interaction with particle beams and energy distribution affects the structure only on the actual length of the jaws (1000 mm), between the two support shafts. Figure 5.4 shows the finite element model of a half of the structure; thanks to the symmetry of the system and also of the energy distribution (as it will be shown later) it is generally possible to perform simulation with the symmetric half-model.

The main support beam, the cooling pipes and the contact plate have common nodes that are “glued” in order to simulate the brazing as discussed in chapter 4; jaw, clamping-plates and copper plates were modeled as separated components. All contact interfaces of real structure were simulated in order to evaluate the behavior of the clamping system. More details on the contact algorithm will be given in the next paragraph.

Preloaded springs were modeled via equivalent hollow cylinders with pre-strain given as initial condition. Jaw assembly model can be globally considered as a beam with a rectangular cross-section; the displacement boundary conditions are applied on the main support beam that is simply supported at the extremities.

The definition of thermal boundary conditions took into account both the energy rate [W/m^3] deposited on the jaw (more details in next paragraph concerning thermal loads) as well as the heat convection on the wet surface of the pipes. The convection coefficient was analytically calculated as a function of hydraulic parameters and of water temperature, leading, with a water flow of 5 l/min at 27 ºC, to a film coefficient of 12360 W/m^{2}K on each pipe. The effect of inner pressure due to the water flow was also considered; a pressure of 15 bars was experimentally measured and an equivalent load was applied to the inner surface of cooling pipes of the FE model.

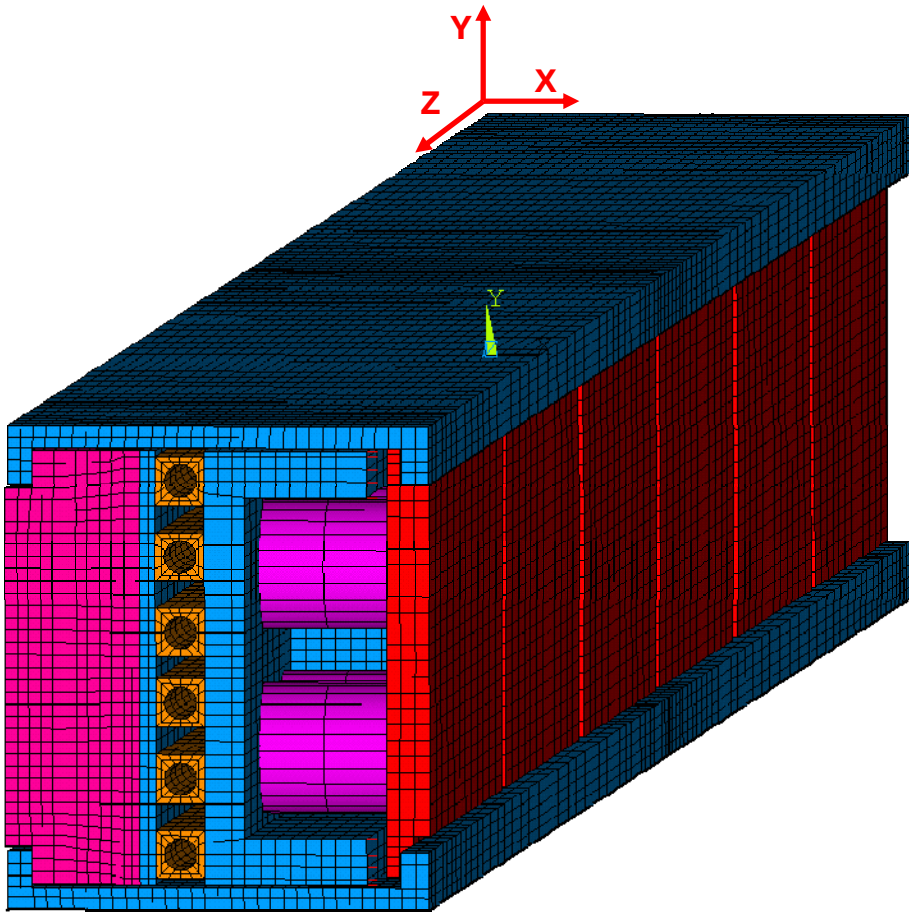

Figure 5.1: 3D Finite Element Model of LHC collimator jaw assembly

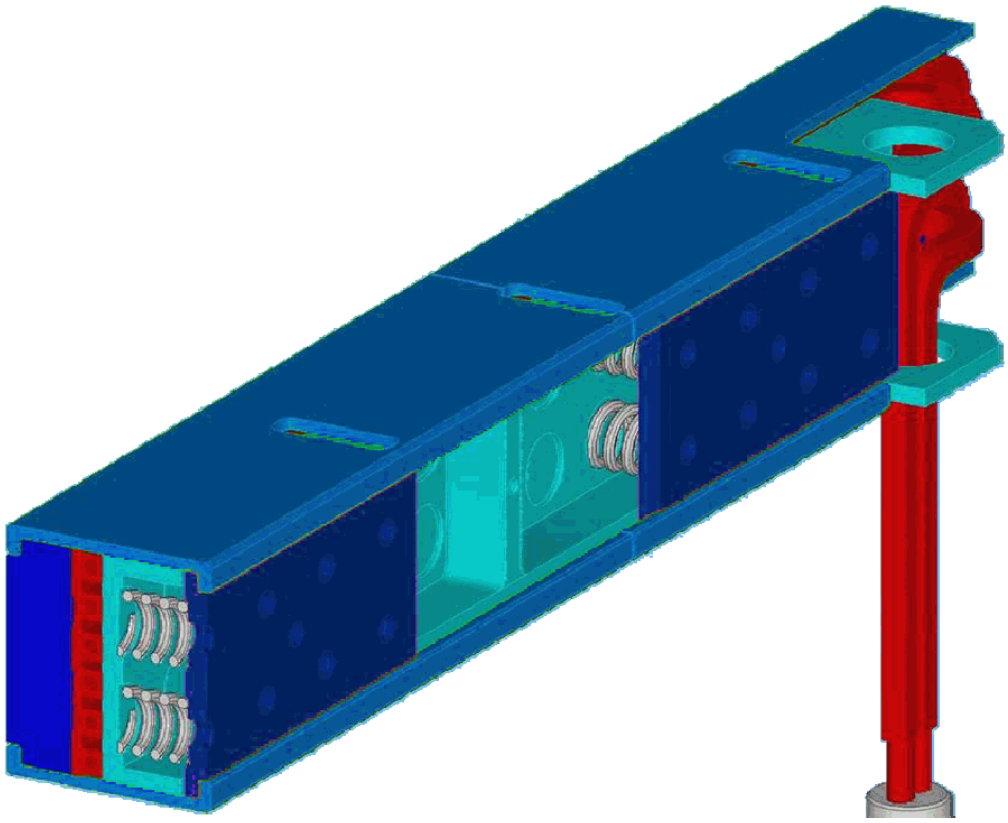

Figure 5.2: Cutaway of LHC collimator jaw assembly (3D CAD model).

Figure 5.3: Picture of LHC collimator jaw assembly showing final tapering of the carbon-carbon jaw.

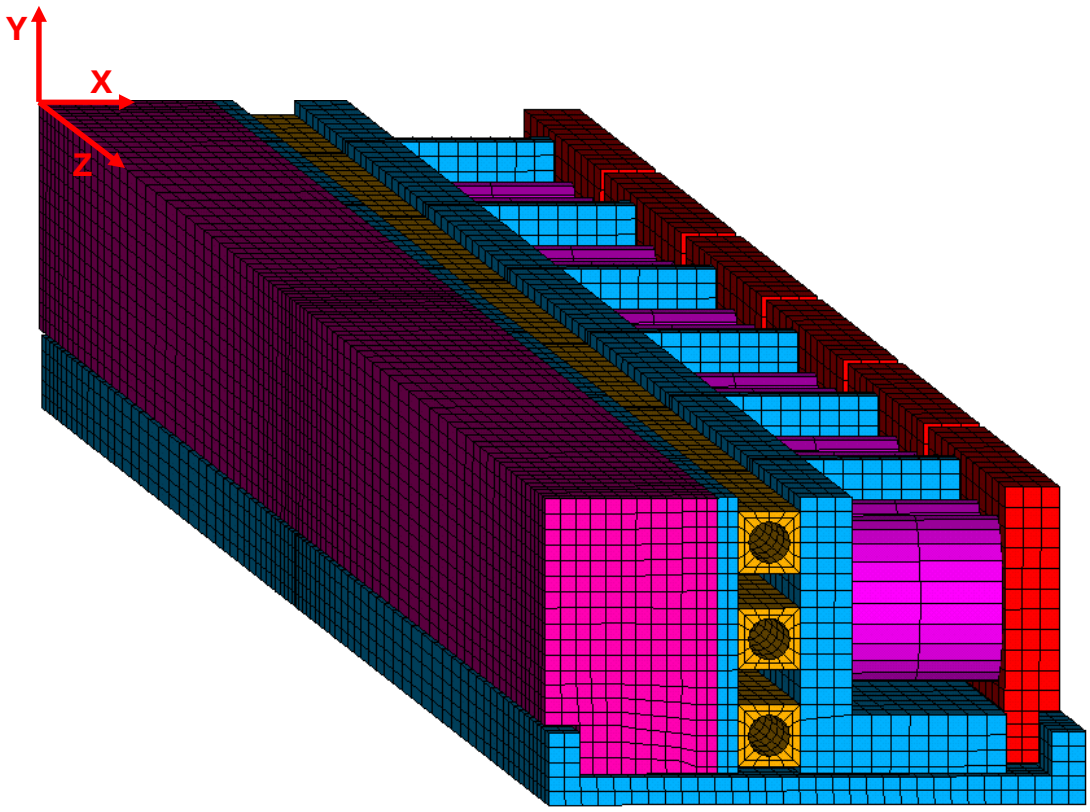

Figure 5.4: 3D FE model of LHC collimator jaw assembly. Half structure is modeled exploiting a symmetry plane.

The coupling between thermal and structural analyses due to contact interfaces, entails that a coupled algorithm of solution must be used; ANSYS includes a coupled finite element called SOLID 5 (see [5.1]) that supports this capability: at each iteration thermal and structural problems are iteratively solved. Thanks to the regular mesh, eight-node brick elements could be used; the mesh size was carefully calibrated in order to obtain accurate results but also to minimize the time of calculation of the CPU. Eq. 5.1 and Eq. 5.2, written in matrix form, show structural and thermal problems that must be solved to evaluate both displacement and temperature degree-of-freedom $\{u\}$ and $\{T\}$.

$$[K]\{u\} = \{F_{pressure}\} + \{F_{thermal}\} \qquad \text{Eq. 5.1}$$

$$[C_{thermal}]\{\dot{T}\} + [k_{thermal}]\{T\} = \{Q_{heatgen}\} + \{Q_{convection}\} + \{Q_{flux}\} \qquad \text{Eq. 5.2}$$

As it will be shown in next paragraphs, material properties depending on temperature have been implemented in the FEM model. This feature together with the use of contact elements introduce a non-linearity in the system. The solution of non-linear equations was based on the Newton-Raphson method as explained in [5.4]

5.2.1 Thermo-mechanical contact algorithm

Thermo-mechanical problems involving multi-component structures require a careful modeling of contact interfaces in order to obtain a reliable simulation of both structural behavior as well as thermal flux between different elements of the system.

In particular, the analysis of the LHC collimation jaw assembly needs high accuracy of the results, given that one of the aim is to evaluate thermal deformations of the order of micrometers with respect to the longitudinal dimension of one meter. As shown in Figure 5.5 all contact interfaces of the structure have been modeled for a correct simulation of the clamping system.

A contact algorithm with mixed formulation was chosen: *lagrangian multiplier* method is used to simulate contact behavior in the orthogonal direction with respect to contact surface while *penalty stiffness* method is used to evaluate the contact behavior in the tangent direction with respect to contact surface. This algorithm is available in ANSYS (see [5.1]) and allows to obtain convergence of the solution with zero penetration between contact interfaces thus improving the accuracy of the results; furthermore the effect of friction can be taken into account.

Thermal flux at the interfaces between components of jaw assembly was simulated using 3D surface-to-surface contact elements with both displacement and temperature dof. A crucial aspect is the evaluation of thermal contact conductance; for many applications, simplified models with constant average value of thermal contact conductance are used. On the other hand the study of a complex structure like the collimation jaw assembly with very demanding design specifications, needs a more accurate and detailed analysis.

An analytical model providing thermal conductance as a function of the contact pressure (see [5.5] and [5.6]) was adopted and implemented in the finite element contact algorithm. This approach allows to evaluate thermal conductance as a function of pressure distribution thus improving the accuracy of numerical simulations. Thermal conductance $h(p)$ depends both on material properties of the two contact

interfaces (Young modulus E and thermal conductivity k) as well as on geometrical parameters of the surface roughness. As shown in Eq. 5.3 thermal flux q depends on the conductance and on delta temperature ΔT between the two contact surfaces.

$$q_{flux} = h(p) \cdot \Delta T \qquad \text{Eq. 5.3}$$

Eq. 5.4 and Eq. 5.5 give equivalent average values of thermal conductivity and elasticity modulus between the two materials of the contact interface. Eq. 5.6 is used for the contact between carbon-carbon jaw and copper plate: in this equation E_g is the Young modulus of carbon-carbon while m_r and A_r are respectively the mean absolute asperity slope and r.m.s. surface roughness. Equation 5.7 is used to describe the contact between two metallic component (i.e. stainless steel counter-plates and copper clamping-plates); in this expression E is evaluated by Eq. 5.5 (Eq. 5.6 and Eq. 5.7 describe thermal contact model as studied in [5.5] and [5.6]). Figure 5.6 shows a schema of the contact joint between a graphite-based material and a metallic material.

The described procedure allows to locally evaluate thermal flux as a function of the contact pressure distribution thus leading to a better evaluation of thermal deformations of the structure. An experimental validation of the procedure described above will be presented.

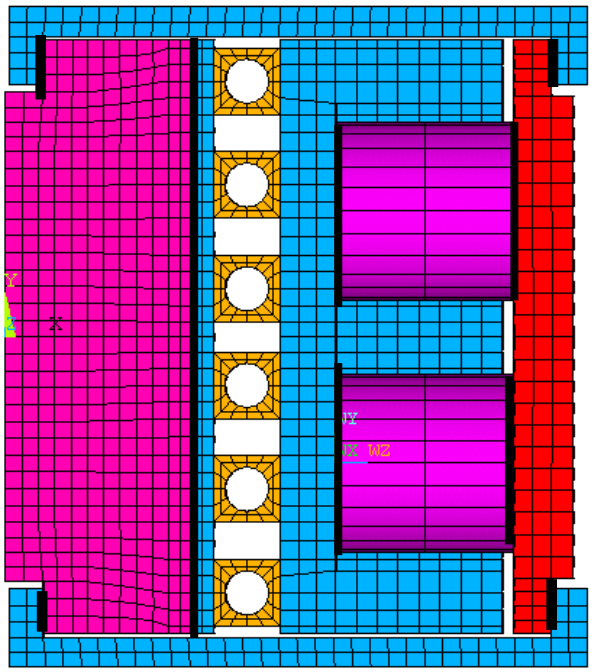

Figure 5.5:3D FEM model front view with contact surfaces put in evidence.

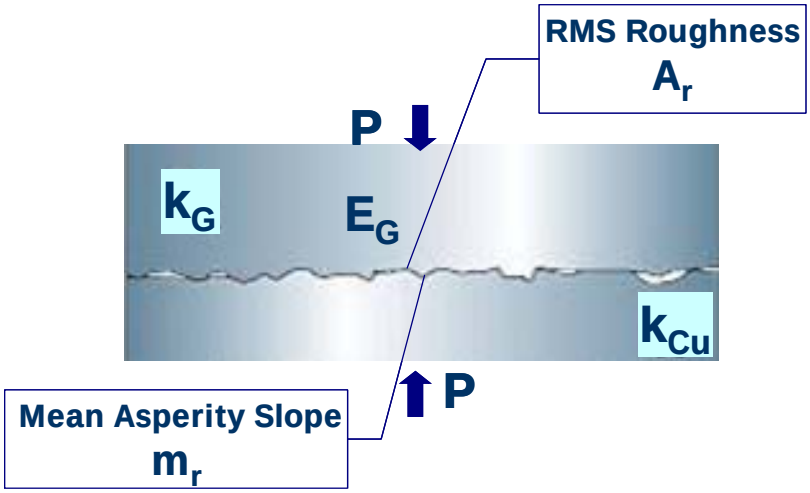

Figure 5.6: Schema of the contact between a graphite-based material and a metallic material. Young modulus, thermal conductivity and geometrical parameters of surface roughness are the main factors that determine the thermal contact conductance.

$$k = \left[\frac{1}{2} \left(\frac{1}{k_1} + \frac{1}{k_2} \right) \right]^{-1} \qquad \text{Eq. 5.4}$$

$$E = \left(\frac{E_1 \cdot E_2}{E_1 \left(1 - \upsilon_1^2\right) + E_2 \left(1 - \upsilon_2^2\right)} \right) \qquad \text{Eq. 5.5}$$

$$h_g(p) = 1.49 \frac{k \cdot m_r}{A_r} \left(\frac{2.3 \cdot p}{E_g \cdot m_r} \right)^{0.935} \qquad \text{Eq. 5.6}$$

$$h_m(p) = 1.55 \frac{k \cdot m_r}{A_r} \left(\frac{\sqrt{2} \cdot p}{E \cdot m_r} \right)^{0.94} \qquad \text{Eq. 5.7}$$

5.2.2 Material models

As discussed in chapter 4 the LHC jaw assembly is made up of several materials. A careful implementation of material models is of primary importance in order to obtain reliable results by FEM simulations. Thermo-physical and mechanical properties of carbon-carbon composite have been experimentally measured while data concerning GLIDCOP, copper-nickel alloy and stainless steel were provided by the suppliers. Figure 5.7 shows FEM model of the carbon-carbon jaw, while pictures from 5.8 to 5.13 show thermo-physical properties of carbon-carbon composite and GLIDCOP measured as a function of temperature and implemented in the FEM model.

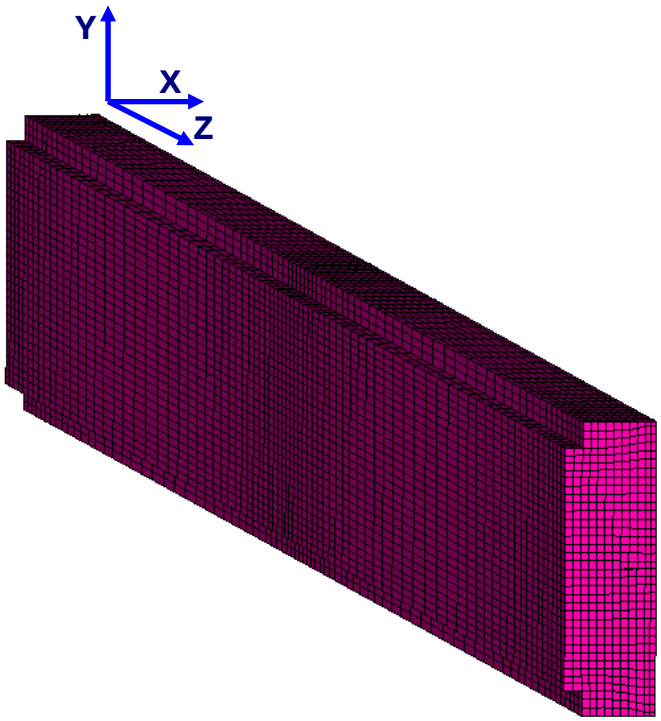

Figure 5.7: FEM model of carbon-carbon jaw. The coordinate system corresponds to the directions of orthotropic material properties that have been measured.

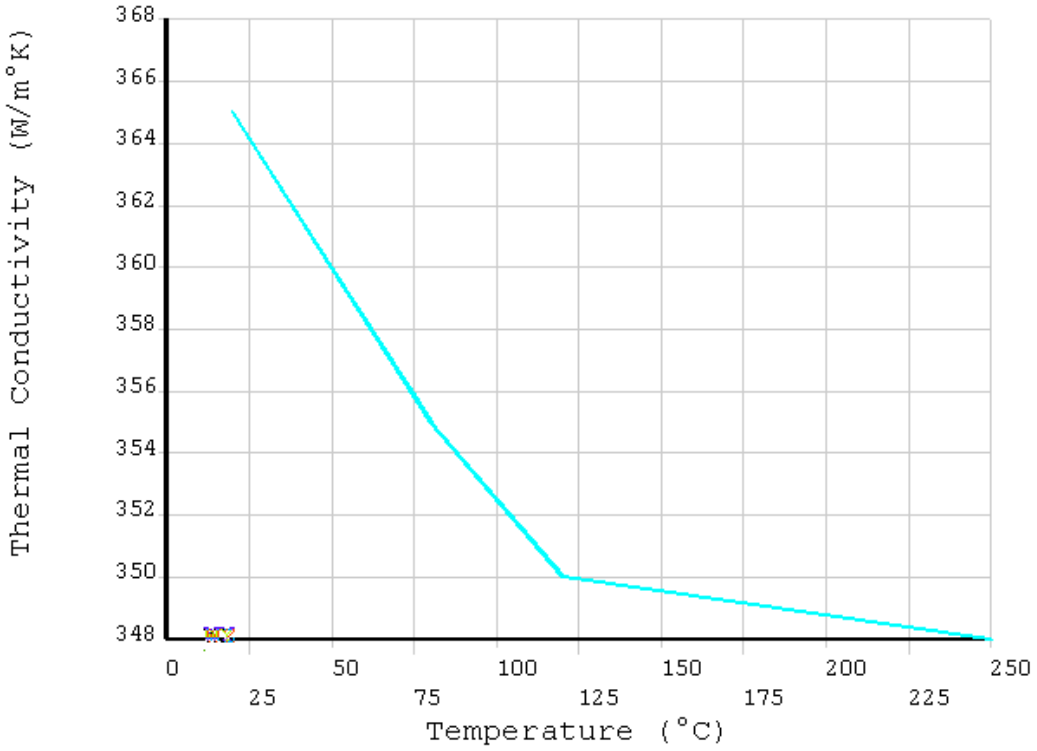

Figure 5.8: Thermal conductivity as a function of temperature for alumina dispersion strengthened copper (GLIDCOP). Data provided by the supplier.

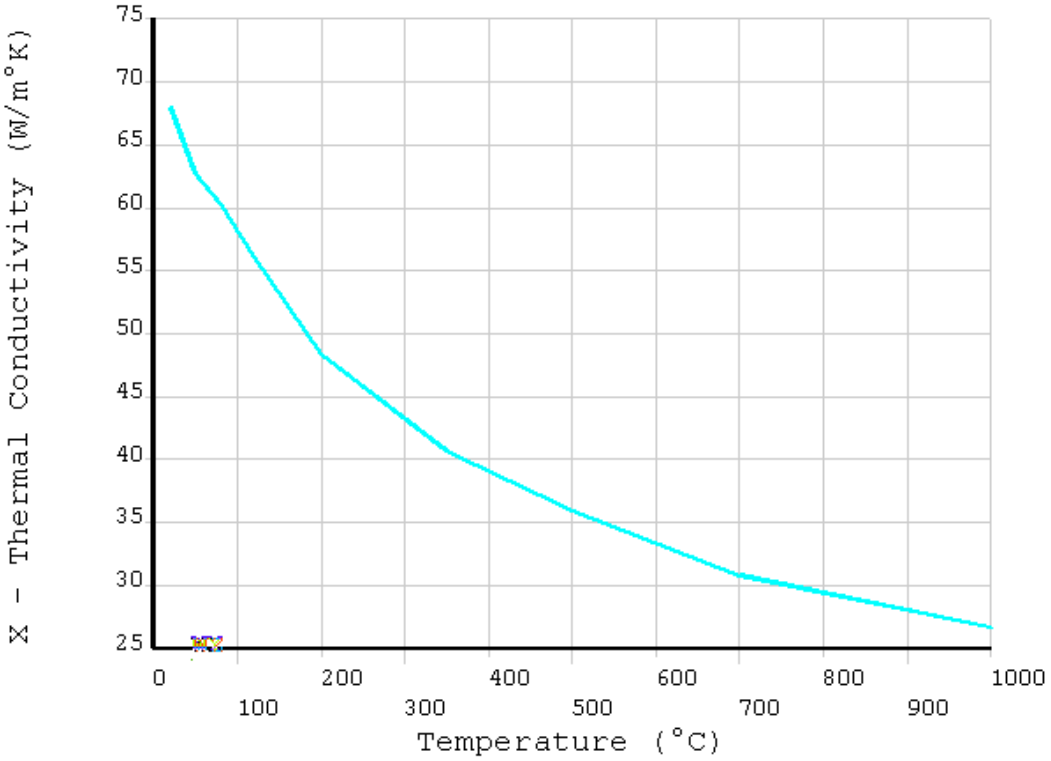

Figure 5.9: Thermal conductivity as a function of temperature for Carbon-Carbon composite (X-direction). Experimentally measured data.

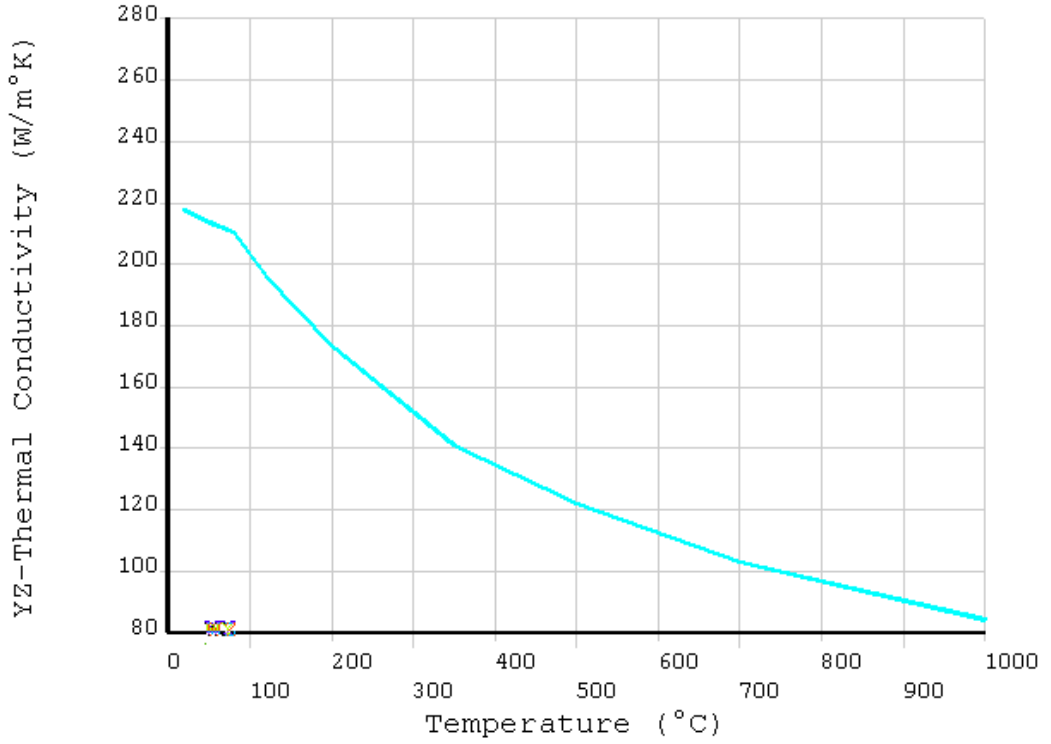

Figure 5.10: Thermal conductivity as a function of temperature for Carbon-Carbon composite (Y and Z directions). Experimentally measured data.

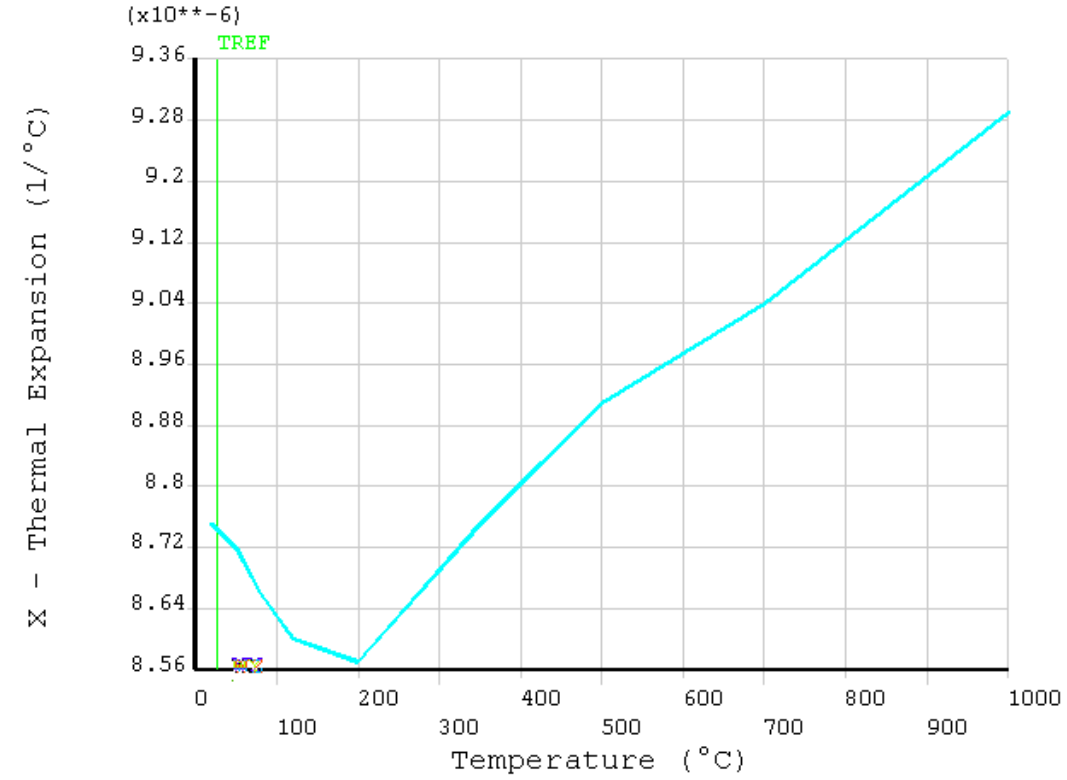

Ex

Figure 5.11: Thermal expansion coefficient as a function of temperature for Carbon-Carbon composite (X directions). Experimentally measured data.

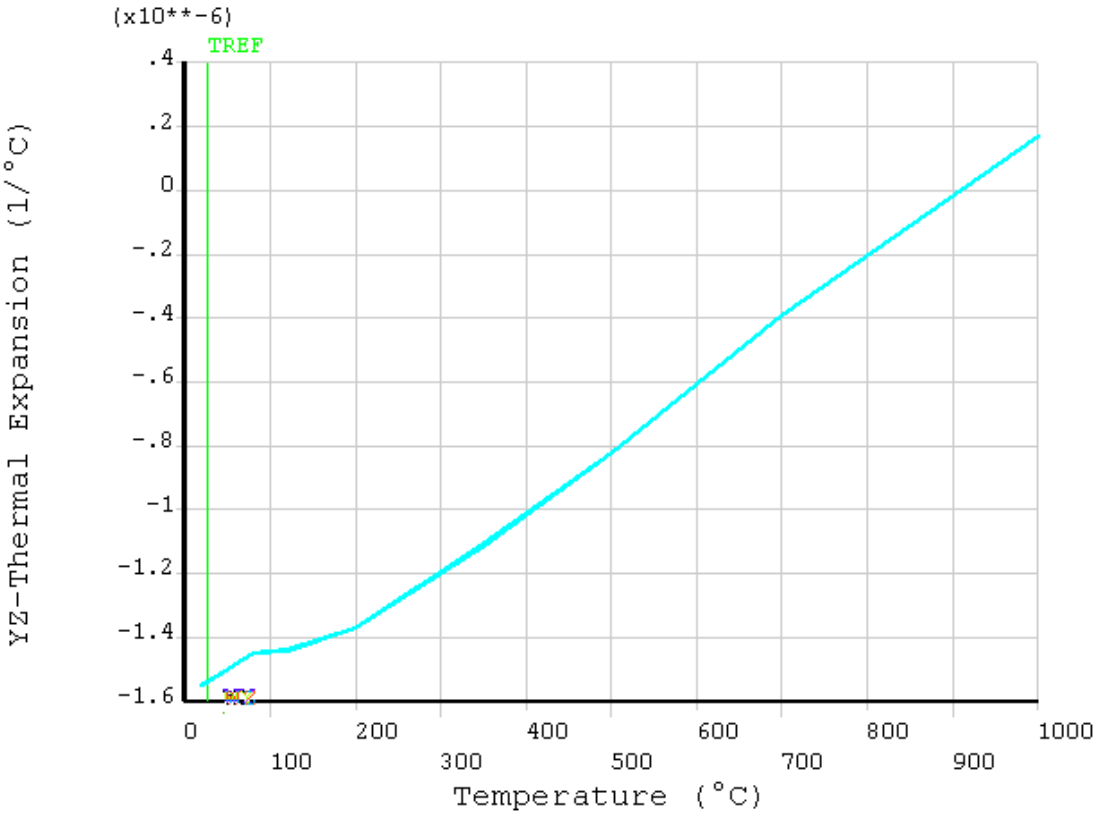

Figure 5.12: Thermal expansion coefficient as a function of temperature for Carbon-Carbon composite (Y and Z directions). Experimentally measured data.

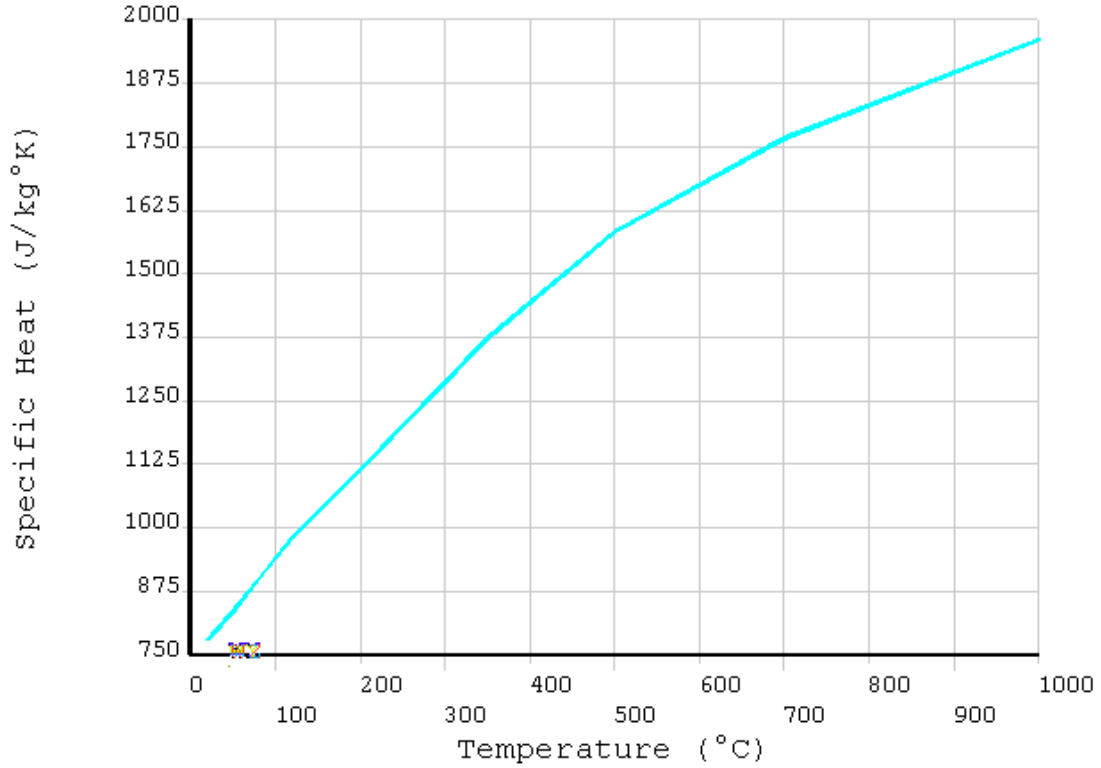

Figure 5.13: Specific heat for carbon-carbon composite. Experimentally measured data.

5.3 Energy deposition

Interaction between particle beams and solids entails several complex phenomena in the domain of particle physics including inelastic scattering of impinging particles and electro-magnetic interactions (see [5.2]). Without entering into details of physics of collisions, that is outside of the scope of this dissertation, we focus on the thermo-structural effects provoked by particle beams.

High energy particles, interacting with nuclei of material, loose their energy that is deposited on the hit structure; the resulting thermal loads are finally used for thermo-mechanical studies.

In particular, for the case of LHC collimators, non-uniform energy distributions must be carefully evaluated in order to provide accurate inputs to thermo-structural analyses. These calculations were performed at CERN with a statistical code based on the Monte-Carlo method called FLUKA (see [4.7]).

Results coming from FLUKA simulations need to be processed via a dedicated algorithm in order to create a correct input to the FEM code. Data from FLUKA were rearranged in a 3D matrix that rebuilt the energy distribution as a function of the

coordinate system of the FE model; 2D matrices at relevant longitudinal cross-sections are extracted (see an example in Figure 5.14). These 2D matrices are read into ANSYS as a 3D table (see Figure 5.15) and applied to the FEM model as internal heat generation [W/m^3]; ANSYS use an interpolation routine that rebuilt the 3D power density distribution. To avoid errors in the transfer of data the mesh size of the two codes (FLUKA and ANSYS) should be comparable; furthermore 2D matrices, used as a reference for the 3D interpolation, must be carefully chosen on the base of the longitudinal energy distribution. A cross-check between the FLUKA outputs and the actual power density distributions imported in ANSYS confirm that the level of error is acceptable in our model.

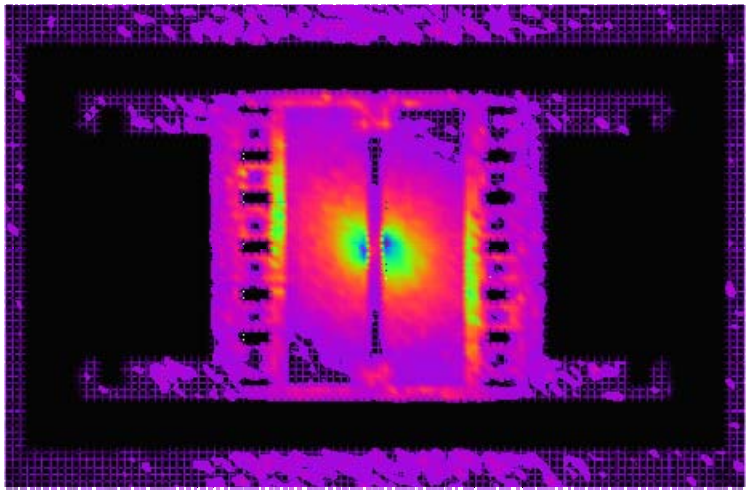

Figure 5.14: Energy distribution on LHC collimator jaw assemblies including vacuum tank. Visualization of a 2D matrix corresponding to a longitudinal cross-section.

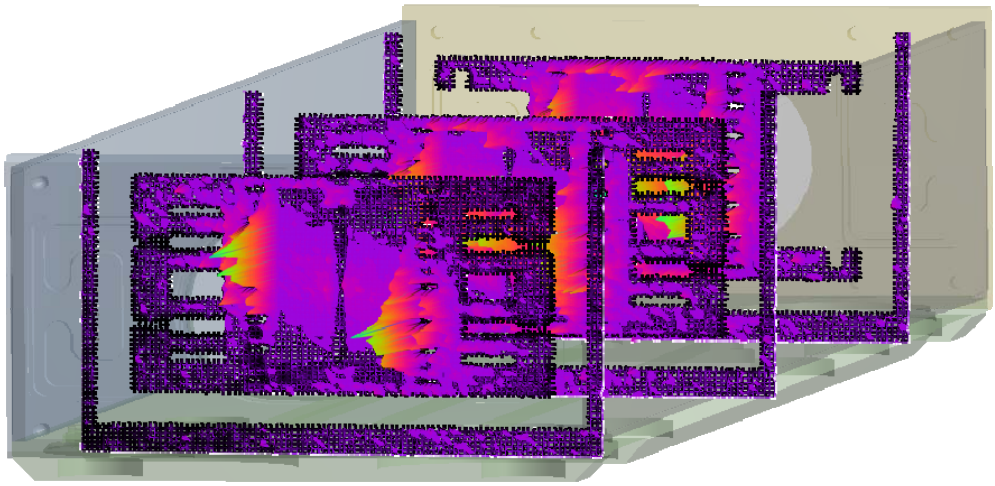

Figure 5.15: Energy distribution on several longitudinal cross-sections of LHC collimator jaw assemblies. 2D matrices are organized in a 3D table based on coordinate system of the FEM model. FLUKA data are rearranged in this way in order to obtain a suitable input to ANSYS.

5.3.1 Steady-state thermal load

As explained in chapter 4, the nominal working condition for the LHC collimators foresees a beam life time of one hour; in this situation, the external halo of particle beam, grazes continuously the surfaces of collimation jaws and a constant energy rate is deposited on the structure. Over this long time-scale the heat diffusion process is completely stabilized thus it is possible to make the assumption of steady-state thermal load with balance between the input energy rate and the heat evacuated by the cooling system. Figure 5.16 shows the power density distribution implemented in the FEM model. Steady-state thermal load foresees a power deposition up to 6 kW on the jaw assembly as indicated in Table 4.5.

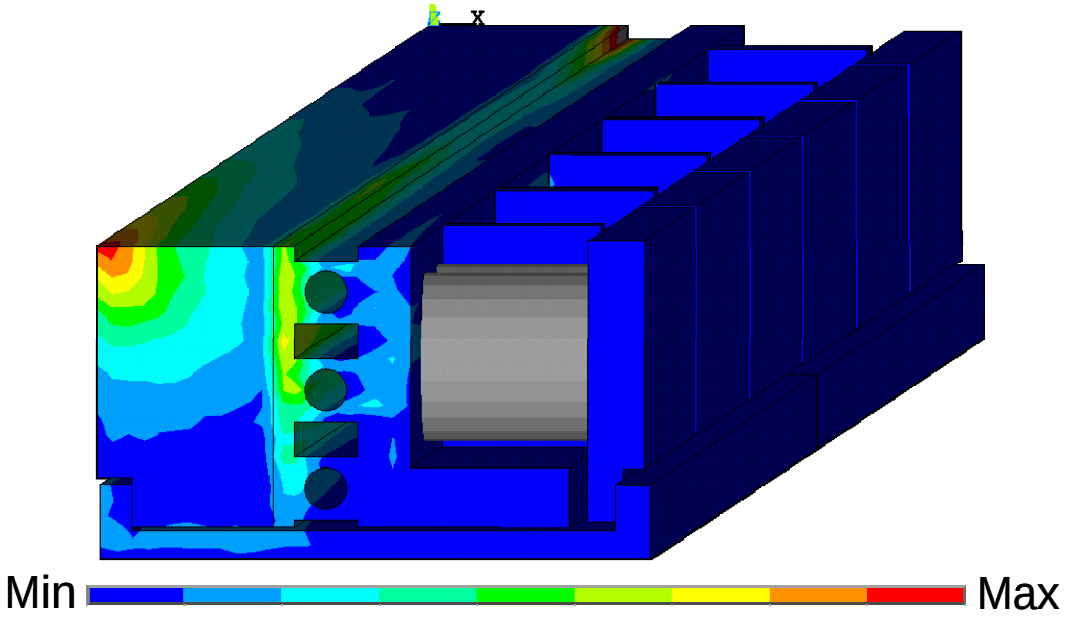

Figure 5.16: Energy rate distribution [W/m^3] on FEM model. Steady-state thermal load 6kW.

5.3.2 Slow transient thermal load

As discussed in chapter 4 a second nominal working condition for the LHC collimators foresees that, during steady-state normal operation, a problem in beam dynamics occurs so that beam life time decrease to 0.2 h; this situation leads to an increase of the energy rate deposition over a transient period of 10 s after which it is assumed that normal steady-state condition is recovered. As qualitatively shown in Figure 5.17 there is a transition between steady-state energy rate deposition and transient energy rate deposition; over 10s the power deposited on the jaw assembly grows up by a factor five leading to a thermal load of 30 kW. Figure 5.18 and Figure

5.19 show the energy rate distribution implemented in the FEM model of the jaw assembly.

Simulation of transient load case was implemented as a sequence of load steps: the results of steady-state analysis are used as initial condition followed by a series of transient load steps as indicated in Table 5.1. Integration time step must be carefully chosen in order to catch the correct thermo-structural behaviour of the collimator jaw assembly.

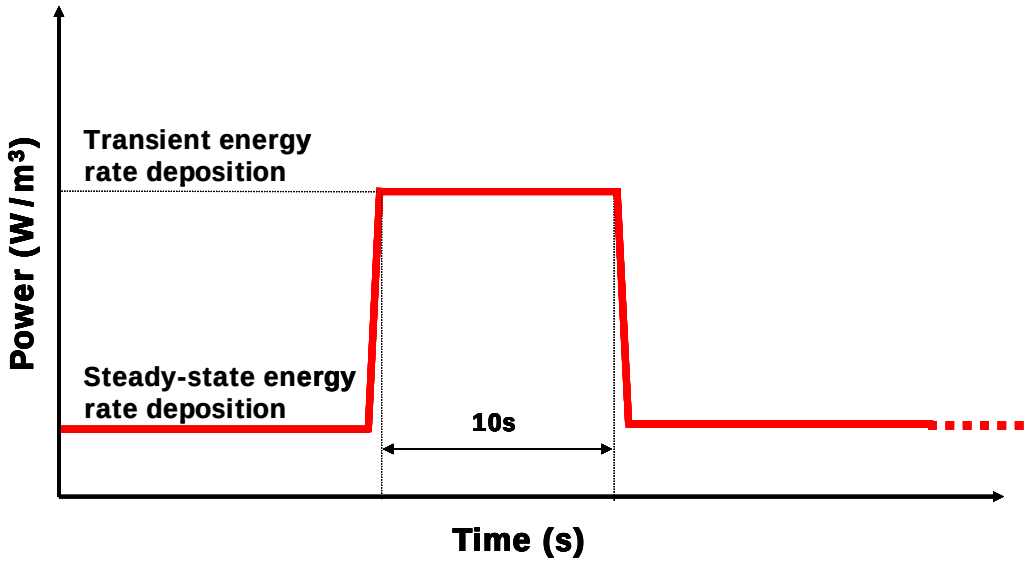

Figure 5.17: Qualitative curve of power deposition as a function of time. Slow transient thermal load.

Table 5.1: Load step sequence: steady-state thermal load is the initial condition for transient analysis that simulates the evolution over time as illustrated in Figure 5.17. Each load step has different duration thus a correct integration time-step Δt must be chosen.

Load step number	Analysis type	Heat load (proton/s)	t (s)	Δt (s)
1	Steady-state	$8e^{10}$	--	--
2	Transient	$8e^{10} \rightarrow 4e^{11}$ (ramped)	0.01	0.001
3	Transient	$4e^{11}$	10	1
4	Transient	$4e^{11} \rightarrow 8e^{10}$ (ramped)	0.01	0.001
5	Transient	$8e^{10}$	20	1
6	Steady-state	$8e^{10}$	--	--

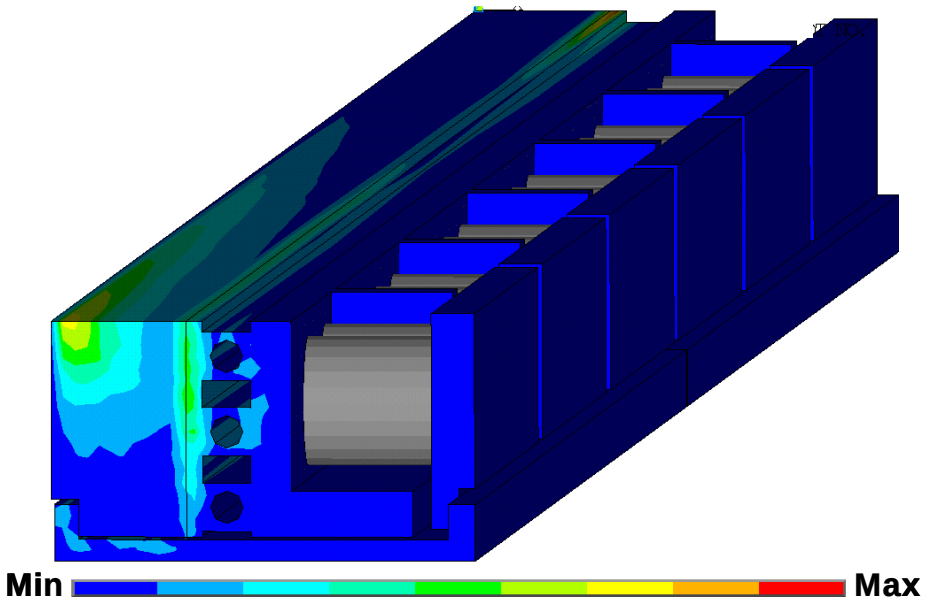

Figure 5.18: Energy rate distribution [W/m^3] on FEM model (front view). Slow transient thermal load 30kW over 10s.

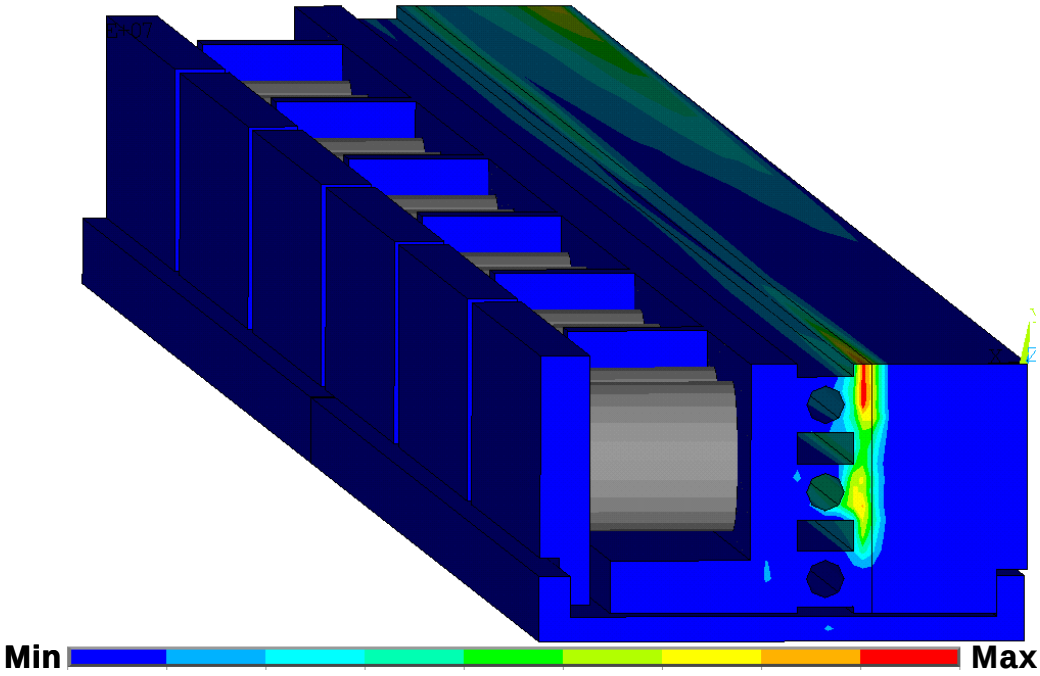

Figure 5.19: Energy rate distribution [W/m^3] on FEM model (rear view). Slow transient thermal load 30kW over 10s.

5.4 Simulation results

This paragraph shows the results of FEM simulation of the LHC collimator jaw assembly in nominal working conditions (steady-state and transient load cases).

Finite Element model used for these simulations corresponds to the final design adopted for the jaw assemblies (presently, the production of LHC collimators is going to finish). Nevertheless several solutions have been simulated and a brief description of design optimization will be presented in next paragraph 5.6

5.4.1 Steady-state analysis

During normal working condition LHC collimators are submitted to steady-state thermal load. Results of non-linear coupled thermo-mechanical analysis confirm that the jaw assemblies are compliant with very demanding functional requirements described in chapter 4.

Figure 5.20 shows that temperature distribution grows up to 50 °C only on a limited portion of the collimation jaw as required by design specification.

Figure 5.21 shows displacements of the carbon-carbon jaw provoked by thermal deformation. Maximum deflection of the jaw is lower than 30 μm as required by design specification concerning geometric stability.

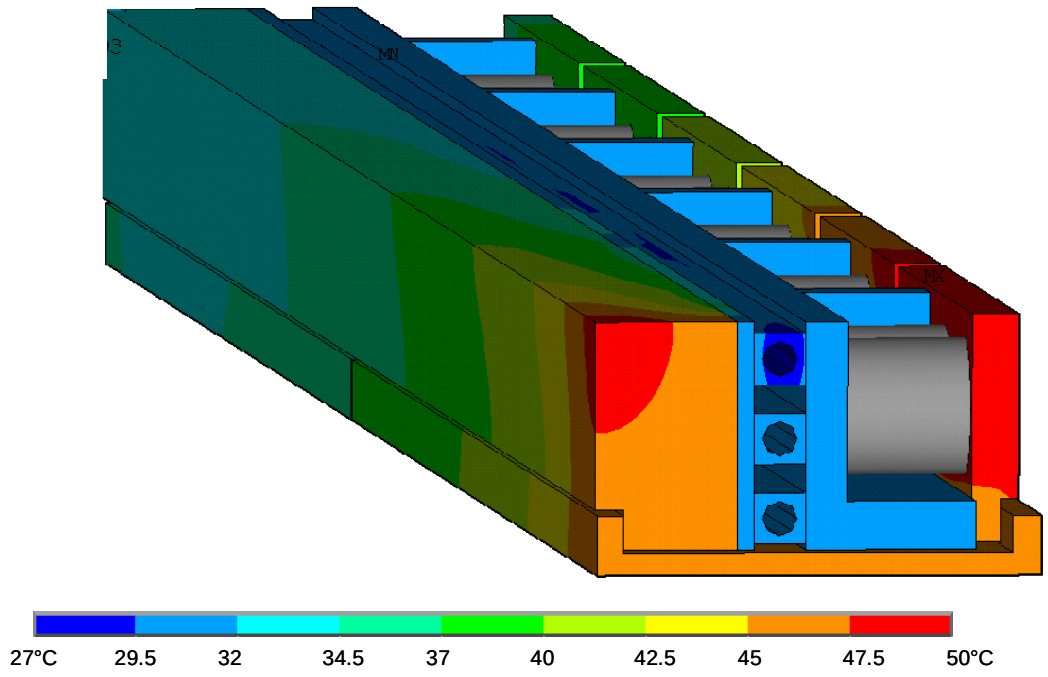

Figure 5.20: Steady-state analysis at $8e^{10}$(p/s) equivalent to 6kW. Temperature distribution on LHC collimator jaw assembly.

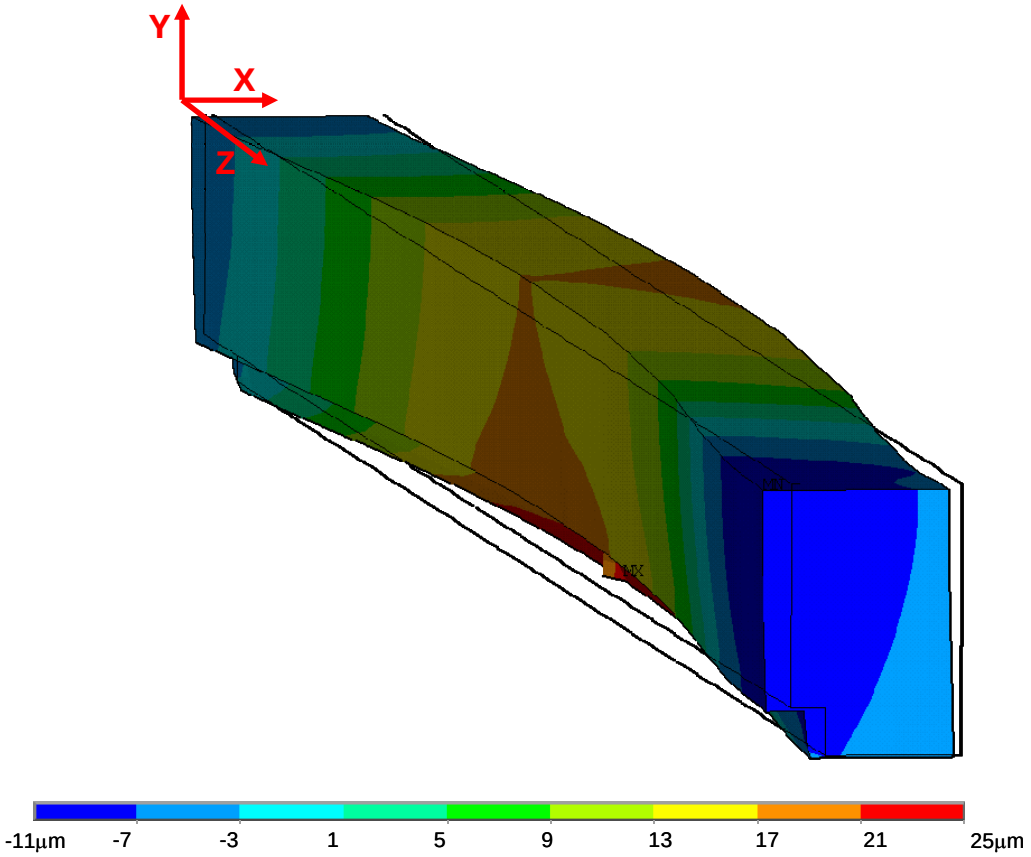

Figure 5.21: Steady-state analysis at $8e^{10}$(p/s) equivalent to 6kW. X – displacements of the collimator jaw; thermal deformation induces a deflection lower than 30µm.

Figure 5.22 shows contact pressure distribution at the interface between collimation jaw and copper plate of the cooling circuit; we can see that pressure is not constant over the surface. It is now evident the importance of having a contact algorithm including thermal conductance as a function of contact pressure. In this way it is possible to carefully simulate thermal fluxes and temperature distribution of the various components of the jaw assembly in order to obtain reliable and accurate results.

Figure 5.23 visualizes thermal fluxes inside the jaw assembly showing the heat load evacuated by cooling pipes.

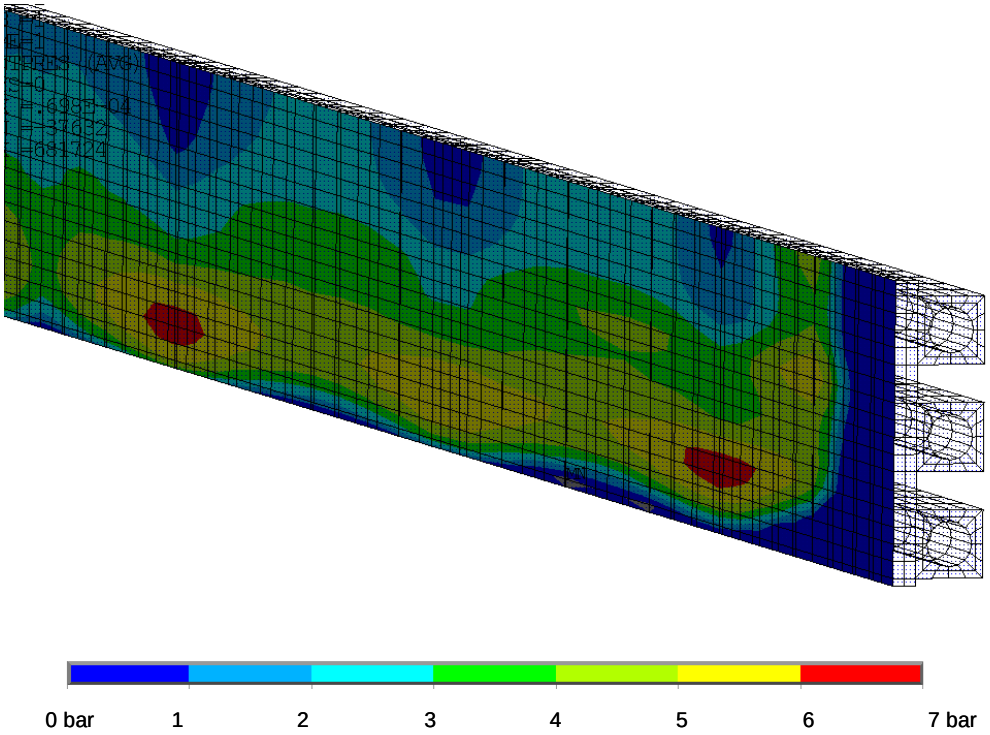

Figure 5.22: Contact pressure distribution at the interface between carbon-carbon jaw and copper plate.

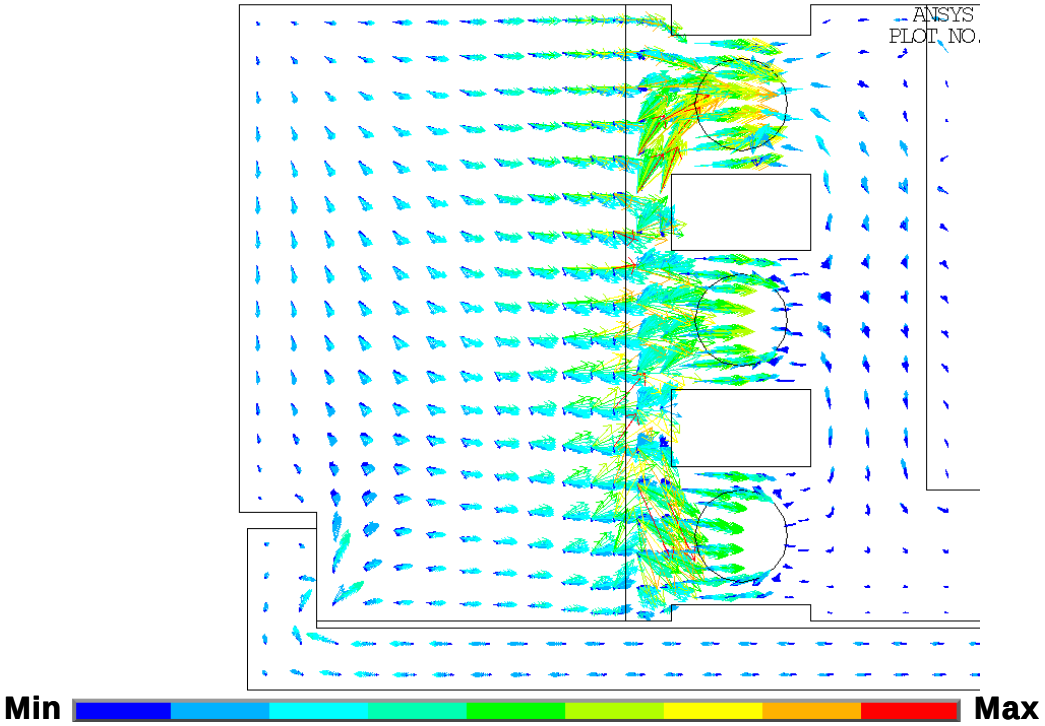

Figure 5.23: Visualization of thermal fluxes inside the collimator jaw assembly.

5.4.2 Transient analysis

Functional requirements foresee that during normal operation the beam loss rate could increase by a factor five over a transient period of 10s. This situation was simulated with the same Finite Element model used for steady-state analysis while the evolution over time of the system was caught by setting up a series of load steps as indicated in Table 5.1. As previously mentioned this load case does not entail dynamic response of the structure.

Figure 5.24 shows the evolution of temperature relative to the hottest point of the carbon-carbon jaw: starting from steady-state condition, temperature grows up during ten seconds of high energy rate deposition. Once normal operation is recovered, overheat is evacuated by cooling circuit and temperature comes back to lower level. Figure 5.25 shows temperature distribution on the jaw assembly at the end of the 10s of high energy rate deposition.

We can see in Figure 5.26 the evolution of X-displacement detected in the middle of the collimation jaw while Figure 5.27 visualizes the maximum jaw deflection. The values of temperature and deformation exceed the limits imposed by design requirements, nevertheless thermo-mechanical response of the structure was accepted considering that transient thermal load entails a temporarily situation that does not affect the correct functionality of the system.

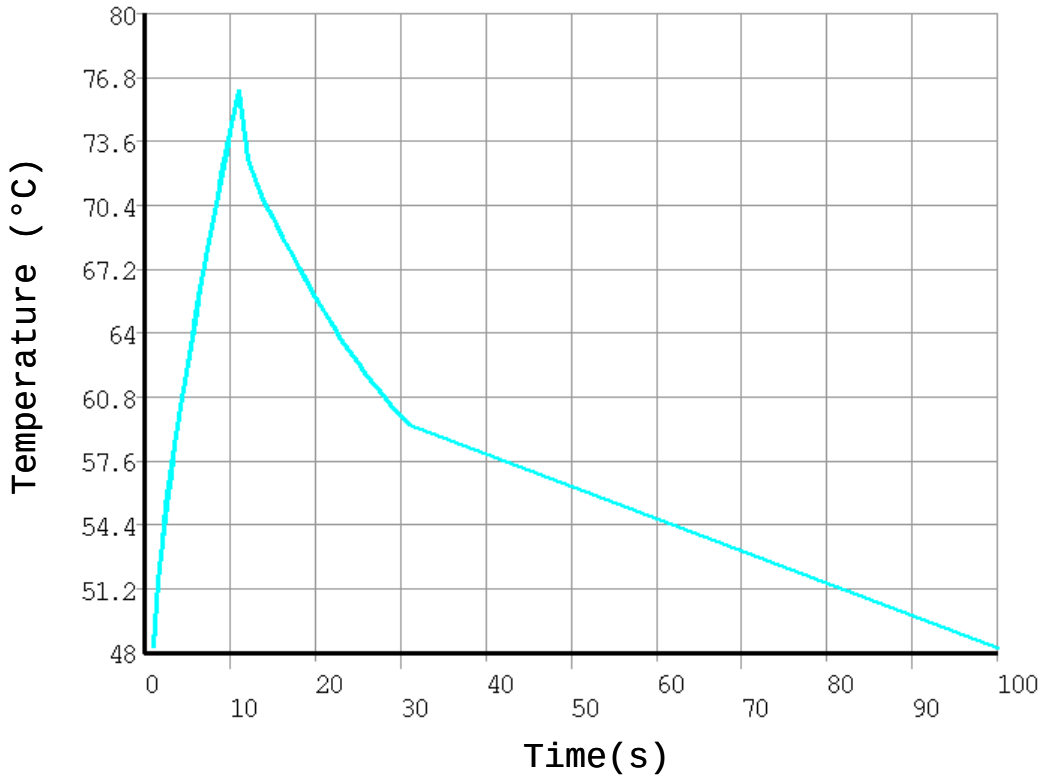

Figure 5.24: Transient analysis at $4e^{11}$(p/s) equivalent to 30kW. Temperature evolution over time on the hottest point of collimator jaw.

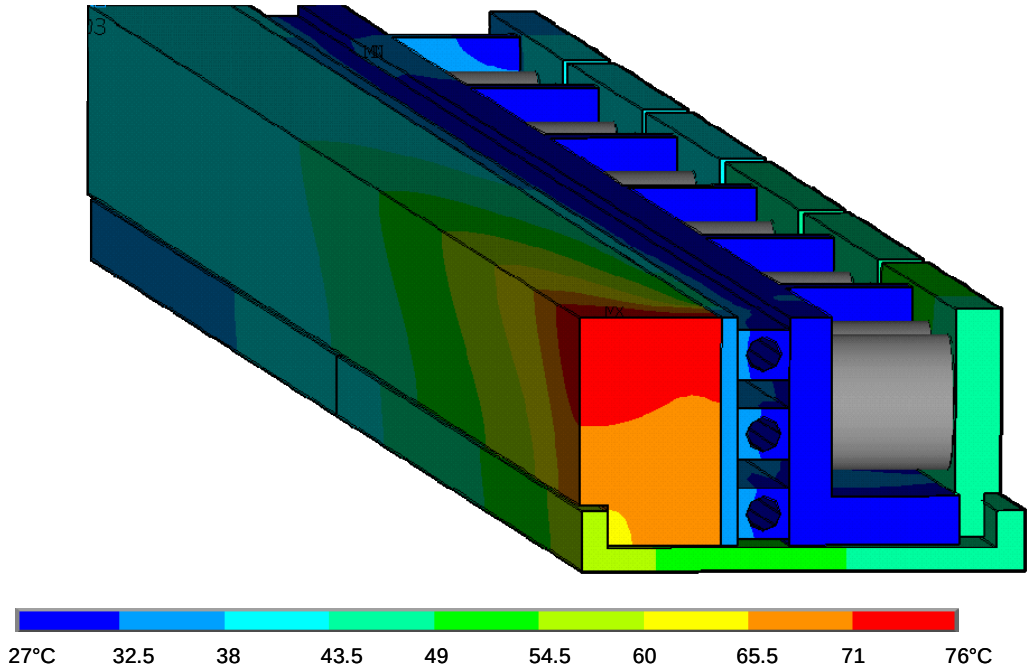

Figure 5.25: Transient analysis at $4e^{11}$(p/s) equivalent to 30kW. Temperature distribution on collimator jaw assembly after 10s of high energy rate deposition.

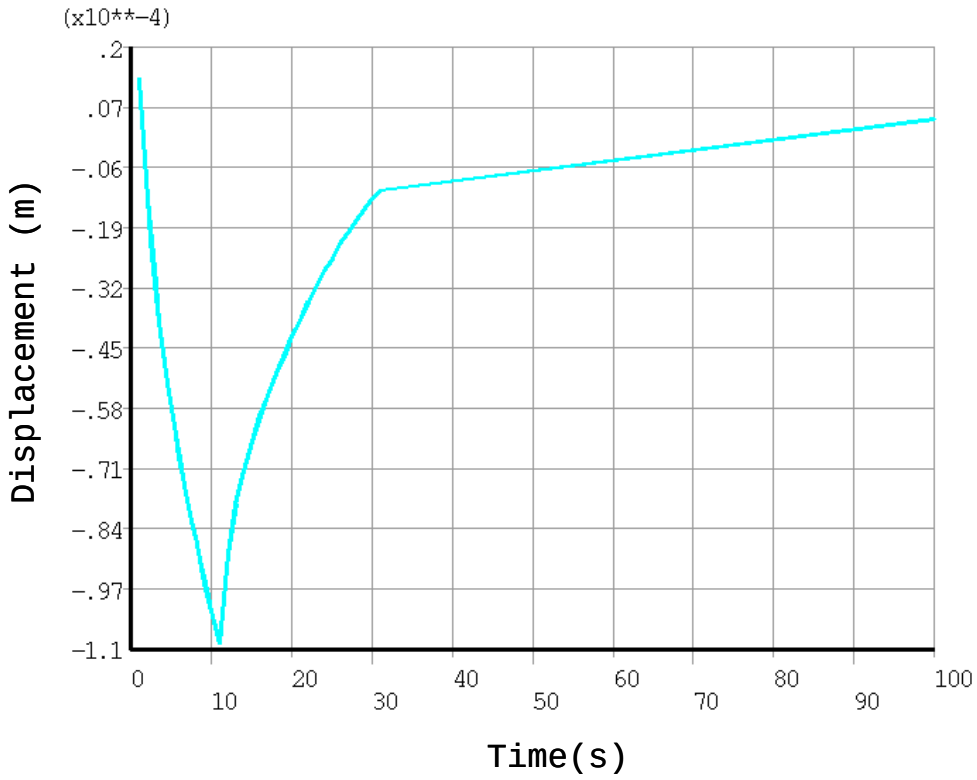

Figure 5.26: Transient analysis at $4e^{11}$(p/s) equivalent to 30kW. Evolution over time of X – displacement in the middle of collimator jaw; thermal deformation temporarily induces a deflection up to 110μm that is recovered as normal condition is re-established.

Finally we can observe in Figure 5.24 and Figure 5.26 that, at time t = 30 s, the response of the system abruptly changes; this is not a physical phenomenon but is due to the fact that last load step was solved as a steady-state problem (see Table 5.1). This choice was taken in order to minimize the time of calculation, anyhow thermo-structural behaviour of the jaw assembly is correctly simulated.

Some comments should be given on the evaluation of stresses: as already explained in the introduction of this chapter, steady-state and slow transient thermal loads do not entail dynamic response of the structure; the level of thermal stresses, as shown in Figure 5.28, plays a minor role compared to the demanding requirements imposed by design specification in terms of maximum allowed temperature and geometric stability.

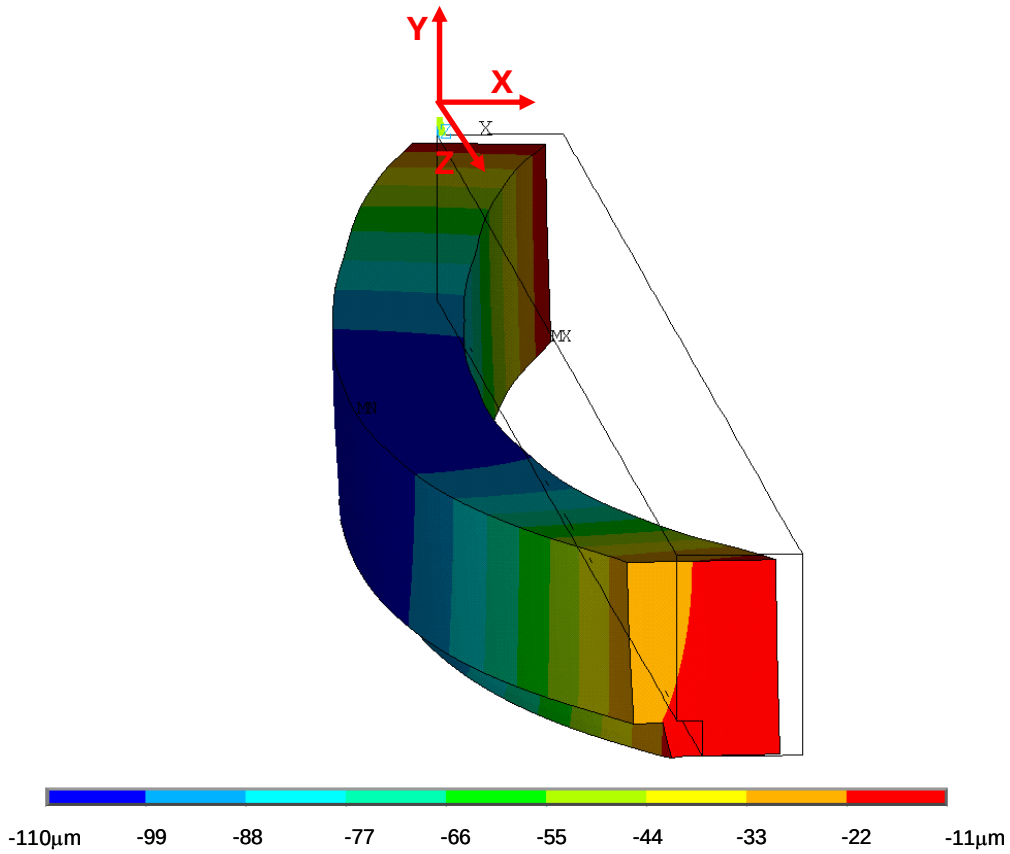

Figure 5.27: Transient analysis at $4e^{11}$(p/s) equivalent to 30kW. X – displacements of collimator jaw corresponding to maximum thermal deformation.

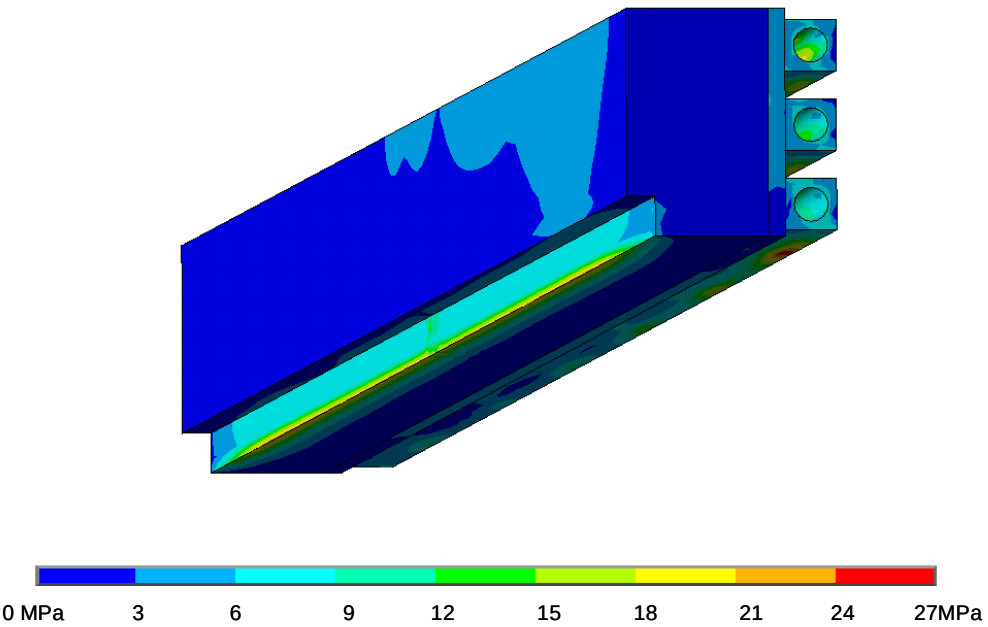

Figure 5.28: Stress intensity (Tresca) on collimator jaw assembly.

5.5 Experimental validation of thermo-mechanical contact algorithm

The organization of an experimental test reproducing real nominal conditions of collimators could not be realized; however, an equivalent structure was developed and an experimental setup was defined as described in [5.8]. Figure 5.30 shows a cross-section of the system developed for experimental measurements; the structure is equivalent to the collimator jaw assembly (see Figure 5.29): same materials have been used as well as the same clamping system. Experimental jaw assembly is equipped with a resistor that supplies the heat load to the carbon-carbon bloc. In this way, the nominal working condition of the LHC collimator submitted to steady-sate thermal load can be reproduced. Temperature can be measured at several locations thanks to the sensors installed in the experimental device (see Figure 5.30).

A FEM model based on the thermo-mechanical contact algorithm described above was developed in order to simulate the experimental set up. Figure 5.31 shows temperature distribution calculated via numerical steady-state simulation assuming a thermal load of 2.5 kW.

Experimental measurements and numerical results are in very good agreement; this confirms the validation of the numerical models developed.

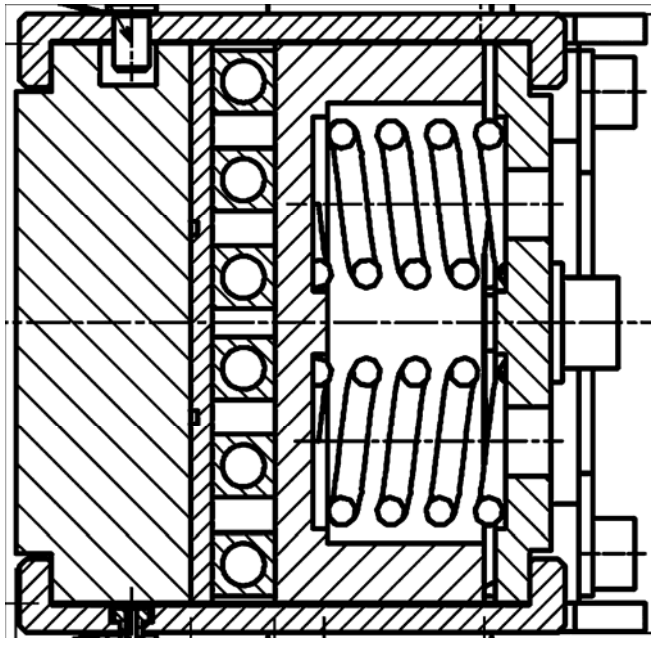

Figure 5.29: Cross-section of LHC collimator jaw assembly

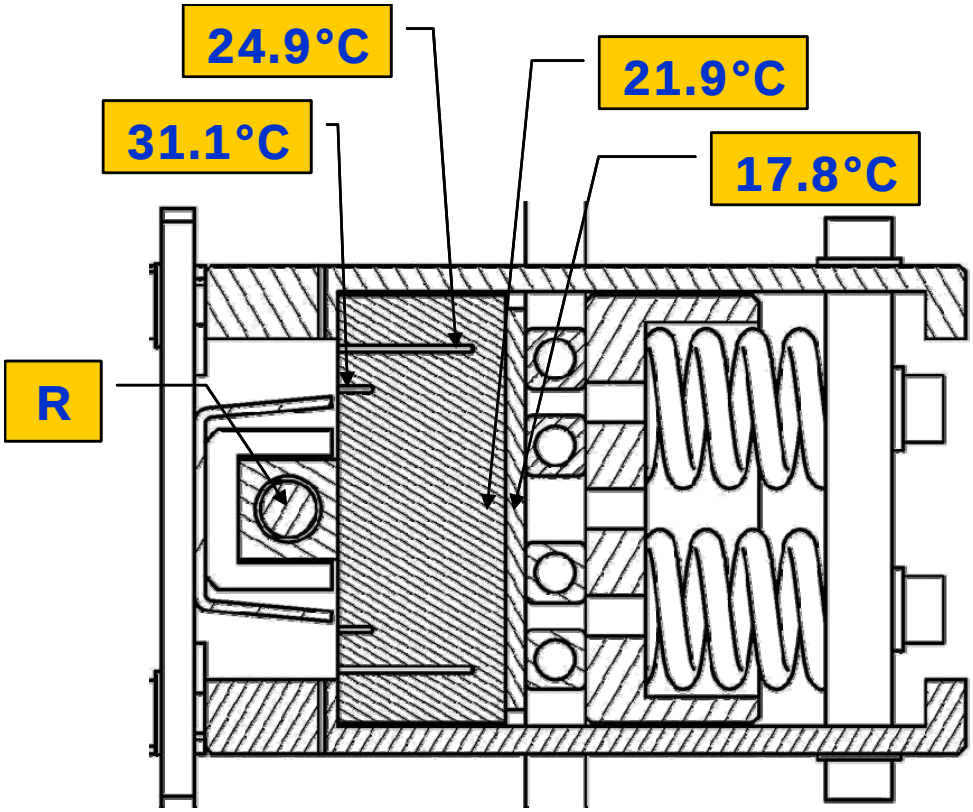

Figure 5.30: Experimental set up equivalent to collimator jaw assembly. A resistor R, placed on the carbon-carbon bloc, supplies the heat load (2.5 kW) thus reproducing the nominal working condition of LHC collimators. Thermal probes are installed as indicated by the arrows so the temperature is measured at several locations.

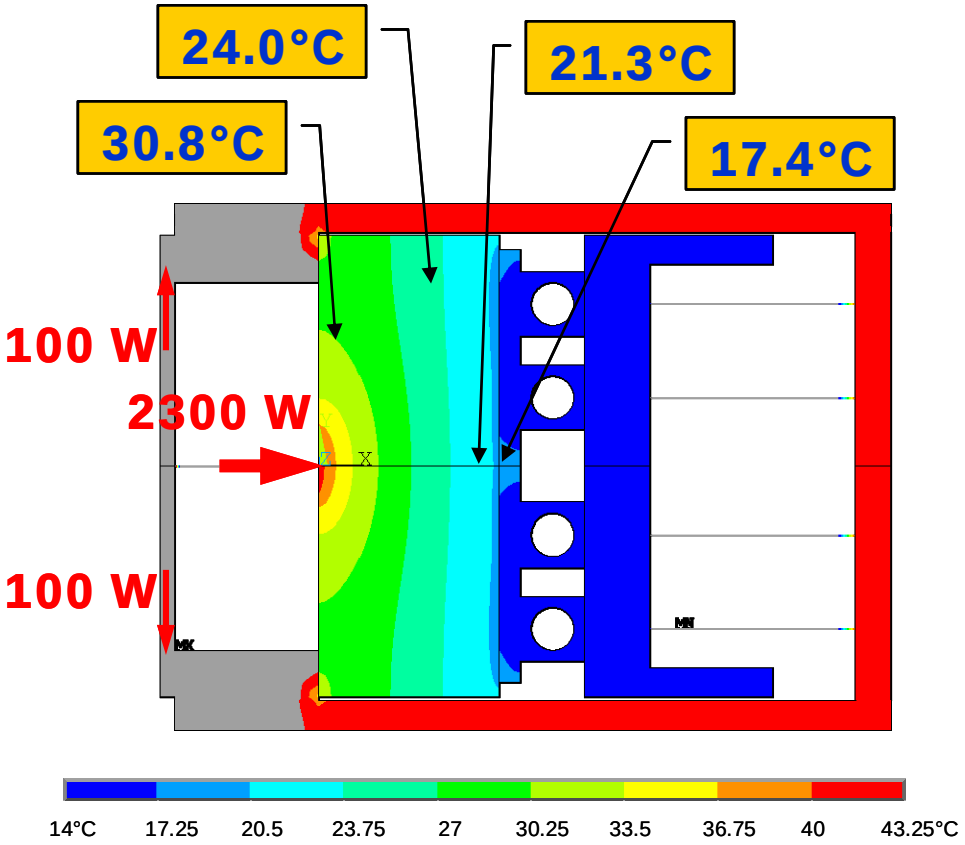

Figure 5.31: FEM model equivalent to the experimental system. Temperatures distribution.

5.6 Design Optimization

This paragraph contains a brief discussion on the design optimization performed for the LHC collimator jaw assembly based on the results obtained from numerical simulations. Several solutions have been tested before getting to the final design presented in chapter 4:

- A comparative analysis was carried out in order to choose the material for collimation jaw (isotropic graphite vs. 2D carbon-carbon composite). Thermo-mechanical response of the structure confirmed a better behaviour of the carbon-carbon composite especially concerning thermal shock robustness as will be discussed in the next chapter.
- Several analyses were performed in order to find the optimal preload for springs; higher preload entails better contact thus increasing the efficiency of cooling circuit, on the other hand geometric stability of the jaw assembly gets worse if spring preload increases. A good compromise was found using a spring preload that gives an average contact pressure of 3bar at the interface between contact plate and collimation jaw.
- An important aspect concerns the design of the clamping plates: starting from a solution with six clamps on each side of the jaw assembly, after several comparative analyses, the best performances in terms of geometrical stability were found with a unique clamping plate; this solution could not be adopted because of mechanical tolerance problems encountered during the manufacturing of such a long piece. Figure 5.32 shows the comparison between the final solution with two clamps and another configuration with four clamps. Figure 5.33 shows a design detail of clamping plates: on the left we can see the final solution adopted while on the right we can observe an old configuration with a larger gap between the clamping teeth.

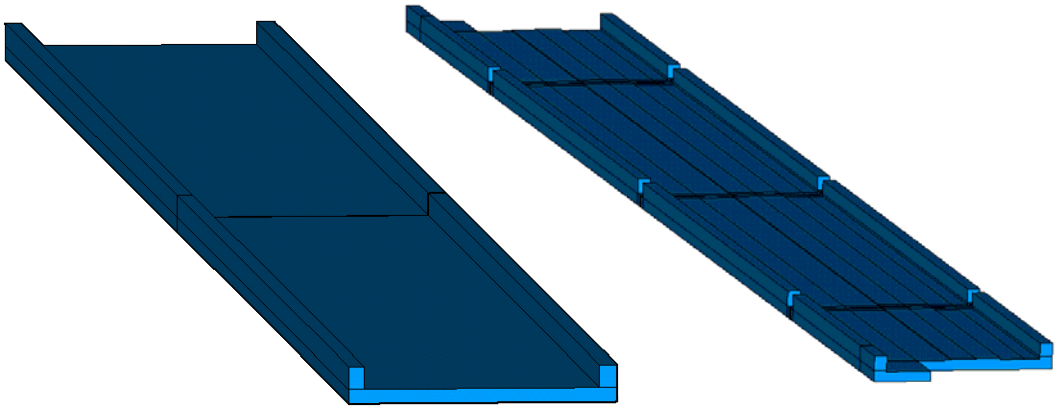

Figure 5.32: FEM model equivalent to the experimental system. Temperatures distribution.

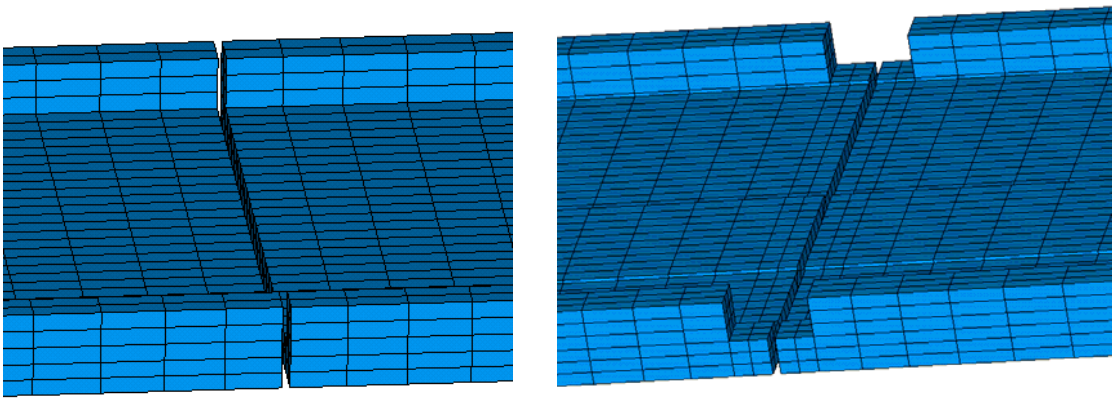

Figure 5.33: FEM model equivalent to the experimental system. Temperatures distribution.

5.7 Summary

Thermo-mechanical effects provoked by high energy particle beams have been studied in case of steady state and slow transient thermal loads not entailing dynamic response of the structure.

A numerical approach based on the Finite Element Method was developed focusing on the simulation of multi-component systems with contact interfaces. Particular attention was paid to the implementation of thermal contact algorithm showing the importance of a detailed model in order to obtain accurate results.

Thermal conductance as a function of contact pressure is described via an analytical model implemented into the FEM code. The problem of coupling between thermal and structural analyses was discussed and solved thanks to an existing algorithm included in the ANSYS code used for the simulations. Thermo-mechanical contact model has been experimentally validated: numerical results obtained from FEM simulations and measurements performed during the thermal test are in very good agreement. Material models include thermo-physical and mechanical properties depending on temperature; both isotropic and orthotropic models can be used within the linear elastic domain of materials.

The developed methods found direct application in the thermo-mechanical analysis of the LHC collimators providing useful results for the design optimization of the structure.

In conclusion, we may state that a numerical FEM approach leading to the solution of non-linear coupled thermo-mechanical problems has been completely developed; the method has been successfully applied to the analysis of the LHC collimators providing reliable and accurate results.

5.8 Nomenclature

$[K]$	Structural stiffness matrix
$\{u\}$	Displacement dof vector
$\{F_{pressure}\}$	Pressure nodal load vector
$\{F_{thermal}\}$	Thermal strain nodal load vector
$[C_{thermal}]$	Thermal specific heat matrix
$[k_{thermal}]$	Thermal conductivity matrix
$\{T\}$	Temperature dof vector
$\{\dot{T}\}$	Time derivative of temperature dof vector
$\{Q_{heatgen}\}$	Heat generation rate nodal load vector
$\{Q_{convection}\}$	Convection nodal load vector
$\{Q_{flux}\}$	Heat flux nodal load vector
k	Thermal conductivity
E	Young modulus
υ	Poisson's ratio
A_r	Rms surface roughness
m_r	Mean absolute asperity slope
h	Thermal contact conductance
p	Contact pressure

References

[5.1] ANSYS User's Manual for Revision 11.0, Swanson Analysis System Inc., Houston.

[5.2] A. Fassò, A. Ferrari, P.R. Sala, “Electron - photon transport in FLUKA status”, Proc. of the Monte Carlo 2000 Conference, Lisbon, (October 23-26 2000).

[5.3] B.A. Boley, J.H. Weiner, Theory of Thermal Stresses, pp 30-44, Dover Publications, New York, 1997.

[5.4] Bathe, K. J., Finite Element Procedures, Prentice-Hall, Englewood Cliffs (1996).

[5.5] E. Marotta, S. Mazzucca, J. Norley, Thermal Joint Conductance for Graphite Materials, Electronic Cooling, 8 (2003).

[5.6] J.J. fuller, E. Marotta, “Thermal Contact Conductance of Metal/Polymer Joints: An analytical and Experimental Investigation”, Journal of Thermophysics and Heat Transfer, 15 (2001).

[5.7] V. Vlachoudis et al., Energy Deposition Studies for the Betatron Cleaning Insertion, Proceedings of Particle Accelerator Conference, Knoxville (USA), 2005.

[5.8] S. Calatroni, W. Vollenberg, Thermal measurements on the LHC Collimator Model, CERN-TS Technical note, 2004.

Chapter 6

Thermo-structural effects due to rapid energy deposition: FEM approach

6.1 Introduction

In this chapter, thermo-structural effects provoked by particle beam impacts have been studied via numerical approach. As widely commented in the second part of the thesis, in case of rapid energy deposition a fast temperature increase occurs in the structure, thermal expansion is prevented by the inertia of the body and dynamic structural response takes place.

A numerical FEM approach, complementary to the analytical solutions, was developed in order to extend the study to the analysis of complex structures in the elastic-plastic domain of the materials.

The solution is based on three sequential steps:

- Once the heat load is known, thermal problem can be solved and temperature distribution can be calculated as a function of space and time.
- Results of temperature analysis are used as nodal loads for the structural analysis so that dynamic thermal stresses and displacements can be evaluated.
- A final quasi-static step is necessary in order to calculate potential permanent deformations of the structure once the dynamic response is vanished.

This approach, generally valid for structures submitted to rapid heat loads, has been successfully applied to the study of the LHC collimators. As described in chapter four, LHC collimators should withstand to accident scenarios entailing large amount of

energy very rapidly deposited. Collimator should resist to beam impacts without damages, maintaining its correct functionality (e.g. geometrical stability). Thus, two aspects must be evaluated: thermally induced vibrations on the short time-scale and permanent plastic deformation on the long time-scale.

Depending on these requirements, a finite element model based on an implicit algorithm of integration was adopted. The unusual choice of using an implicit scheme to solve a dynamic problem is due to the necessity of performing a static structural analysis to evaluate potential plastic deformations after the dynamic effect disappears; finally, the problem was completely solved exploiting the implicit code ANSYS [6.1] thus avoiding the use of different codes for dynamic and static analyses.

The numerical method proposed has been experimentally validated. Two experimental tests have been performed at CERN: in the first test a prototype of the LHC collimator was installed in the SPS ring and submitted to several full beam impacts, while the second test was carried out using an LHC collimator coming from series production. Comparison between simulations and experimental measurements confirmed the validity of the numerical solutions.

6.2 Energy deposition in case of particle beam impact

As discussed in previous chapter, a detailed energy deposition map is essential to correctly simulate thermal loads used as input for thermo-mechanical calculations of complex structures. Table 6.1 includes beam parameters for the case of abnormal beam losses; results coming from FLUKA simulations (see [6.3]) need to be processed via a dedicated algorithm, as illustrated in chapter 4, in order to obtain a correct input for the FEM code.

Figure 6.1 shows the energy deposition map on a longitudinal cross-section of collimator jaw assembly obtained from FLUKA. Figure 6.2 visualizes the heat load distribution implemented into the FEM model of the jaw assembly.

Table 6.1: Accident scenarios of LHC collimators: direct beam impacts entail that a large amount of energy is deposited on the structure very rapidly. This table collects parameters of heat load in case of abnormal beam losses.

Accident Case	Beam Energy [GeV]	Beam Intensity [protons]	Energy Deposit [MJ]	Impact duration [μs]
Injection Error	450	$3.2 \cdot 10^{13}$	2.073	7.2

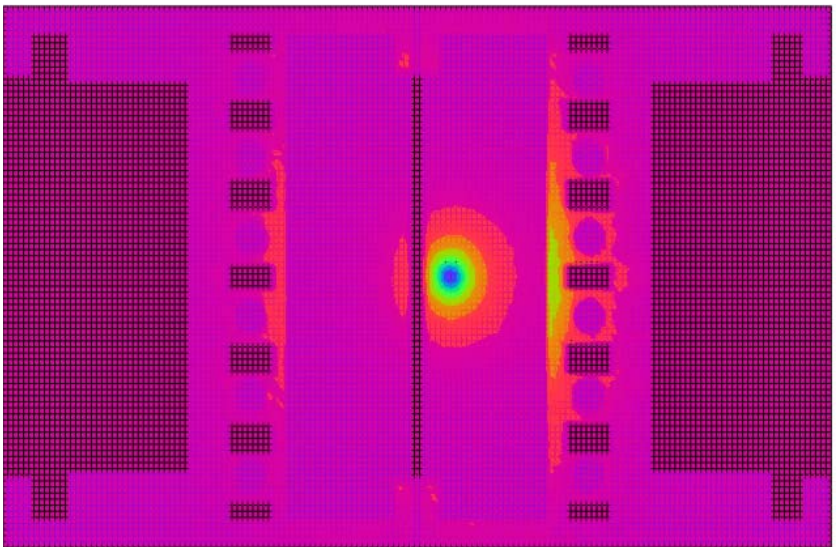

Figure 6.1: Energy distribution on LHC collimator jaw assemblies in case of particle beam impact (FLUKA results). Visualization of a 2D matrix corresponding to a longitudinal cross-section.

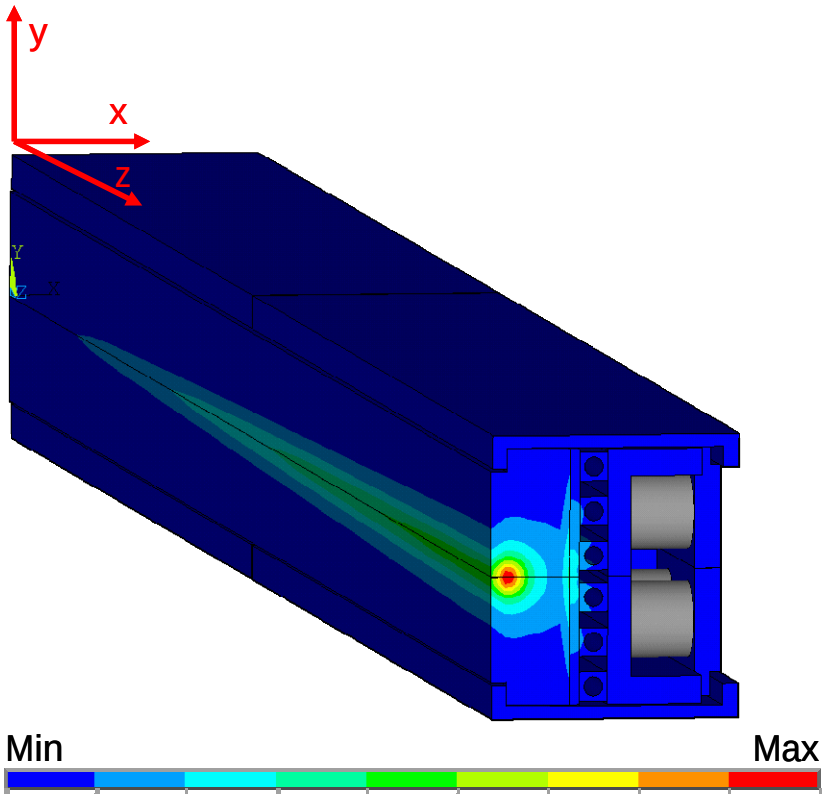

Figure 6.2: Power distribution [W/m^3] in case of particle beam impact implemented in the FEM model of the jaw assembly.

6.3 Finite element model for accident scenario

The system was simulated with a detailed 3D finite element model (same geometry presented in chapter 5) including all contact surfaces between the various components. Accident scenario foresees that high heat load is very rapidly deposited on the structure as described in previous paragraph.

Figure 6.3 shows the comparison between the real structure and the finite element model: on the left side is also visualized the energy distribution provoked by particle beam impact.

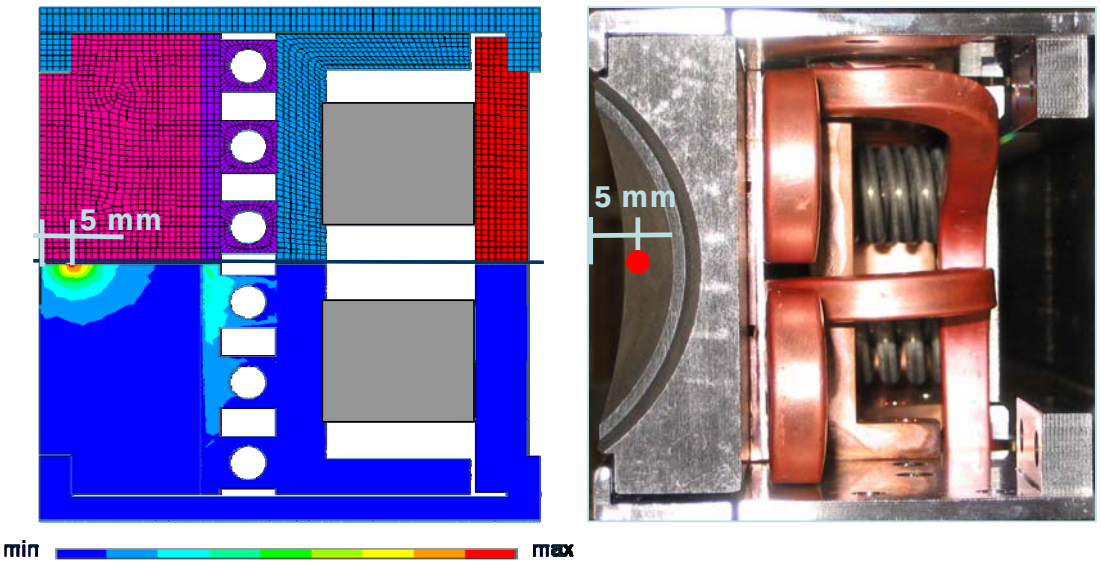

Figure 6.3: On the right side, picture of LHC collimator jaw assembly (front view). On the left side, FEM model: the image visualizes the mesh as well as the energy distribution with an impact parameter up to 5 mm as foreseen by functional requirements.

As discussed in previous chapter, the weak thermo-elastic coupling hypothesis can be assumed (see [5.3]), thus the influence of strain rate on temperature distribution can be neglected.

The jaw assembly can be considered as a beam with a rectangular cross-section simply supported at the extremities; thus, following the same analytical approach described in the second part of this dissertation, it is possible to obtain preliminary estimations of structural response of the system. This is useful in order to correctly setup the FEM model.

Following this approach it is important to evaluate the Boley's number of the collimator jaw assembly in order to assess the response of the structure. Thermal diffusion time of the jaw assembly (calculated with Eq 6.1) is the typical thermal response time of the system, while typical structural response time (e.g. first period of flexural oscillation of the jaw assembly) is calculated with Eq. 6.2 (M, L and I are respectively mass, length and cross-section inertia of the collimator jaw assembly while E is an equivalent Young modulus obtained as average value between the various materials of the jaw assembly). Boley's parameter B can be easily calculated via Eq. 6.3.

Given that τ_{diff_jaw} is of the order of 13 s while structural response time is almost 20 ms, we obtain $B \sim 25$; this value, as indicated in Figure 3.9, entails that a dynamic response of the structure in terms of thermally induced vibrations must be taken into account. Moreover, considering the heat load duration (τ = 10 μs), it is clear that thermal diffusion can be neglected within the time-range of interest given by typical structural response time.

$$\tau_{diff\_jaw} = \frac{l^2}{\kappa_{cc}} \qquad \text{Eq. 6.1}$$

$$t_{flex} = \frac{2}{\pi}\sqrt{\frac{ML^3}{EI}} \qquad \text{Eq. 6.2}$$

$$B = \sqrt{\frac{\tau_{diff\_jaw}}{t_{flex}}} \qquad \text{Eq. 6.3}$$

In conclusion, given the rapidity of the phenomenon, thermal conductivity does not play a relevant role on the short time-scale; as a consequence thermal conductance at the interfaces can be neglected thus avoiding the coupling between thermal and structural analyses. Upon these assumptions thermal and structural problems can be separated and sequentially solved. This is an important aspect for the choice of the numerical model that could be used.

Further, preliminary estimations can be performed for the evaluation of thermal stresses: once energy rate distribution is known (see Figure 6.2), maximum temperature at the end of heat load deposition can be easily calculated with Eq. 6.4. Temperature rapidly increases during the heat load deposition τ up to T_{max}; thermal

expansion is prevented by the inertia of the body and dynamic longitudinal response of the structure takes place.

$$T_{\max}(x,y,z) = \frac{W(x,y,z)\cdot\tau}{\rho\cdot c_p} \qquad \text{Eq. 6.4}$$

$$\Delta T = T_{\max}(x,y,z) - T_{ref} \qquad \text{Eq. 6.5}$$

Once temperature distribution is known, assuming that no longitudinal expansion occurs, it is possible to estimate the range of compressive stresses provoked by the thermal shock (see Eq. 6.6); this simple formula allows to foresee possible permanent damage in case of thermal stresses exceeding the yield limit of the materials σ_{lim}.

Eq. 6.7 shows how to calculate the threshold of energy rate deposition W_{lim} beyond which plastic stresses take place.

$$\sigma_z = \frac{E\alpha\Delta T}{(1-\upsilon)} \qquad \text{Eq. 6.6}$$

$$W_{\lim} = \frac{\sigma_{\lim}(1-\upsilon)\rho\cdot c_p}{E\alpha\tau} \qquad \text{Eq. 6.7}$$

This simplified approach was adopted for the preliminary analysis of collimation jaw assembly: Figure 6.4 shows the energy distribution on the metallic support including cooling pipes and contact plates; the highlighted region indicates where potential permanent deformation could appear due to the high heat load.

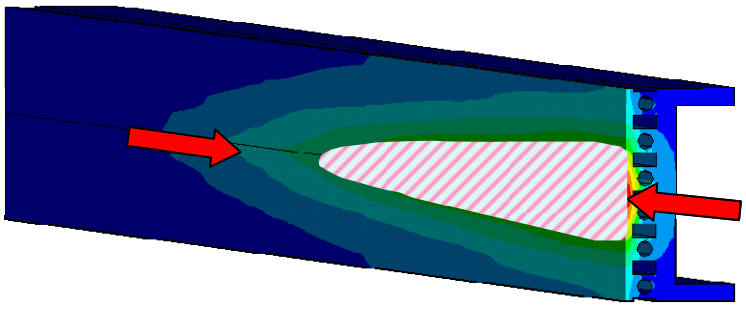

Figure 6.4: Energy distribution on metallic support of collimation jaw assembly. The highlighted region corresponds to a zone of possible permanent deformations due to the level of energy deposition.

Preliminary calculations, based on the analytical approach, gave an important contribution to the implementation of a proper finite element model. Following aspects were in particular clarified:

- Coupling between thermal and structural problem can be neglected
- Thermally induced vibrations should be considered.
- Potential permanent deformation should be taken into account using elastic-plastic material models.

As anticipated in the introduction of this chapter, the numerical method developed is based on three sequential steps that allows the evaluation of thermally induced vibrations on the short time-scale and permanent plastic deformation on the long time-scale.

Next paragraphs describe in details the models used for thermal analysis, dynamic structural analysis and quasi-static analysis.

6.3.1 Material models

Careful evaluation of permanent deformations provoked by high energy beam impacts needs accurate elastic-plastic material models.

On the basis of preliminary analytical predictions, it was assumed that metallic support including main beam, cooling pipes and contact plate are the critical components potentially affected by plastic strains. Stress-strain curve of GLIDCOP was experimentally characterized (see Figure 4.13); the elastic-plastic material curve was implemented into the FEM code as shown in Figure 6.5 using a multi-linear kinematic hardening model as explained in [6.4].

Cooling pipes are made up of Copper-Nickel alloy: material behavior was simulated with a simplified bilinear kinematic hardening model; Stress-strain curve of the material implemented in ANSYS is shown in Figure 6.6. The same thermo-physical material properties as well as the same carbon-carbon composite orthotropic model used for quasi-static simulation (as described in chapter five) were included in the numerical model devoted to beam impact simulation.

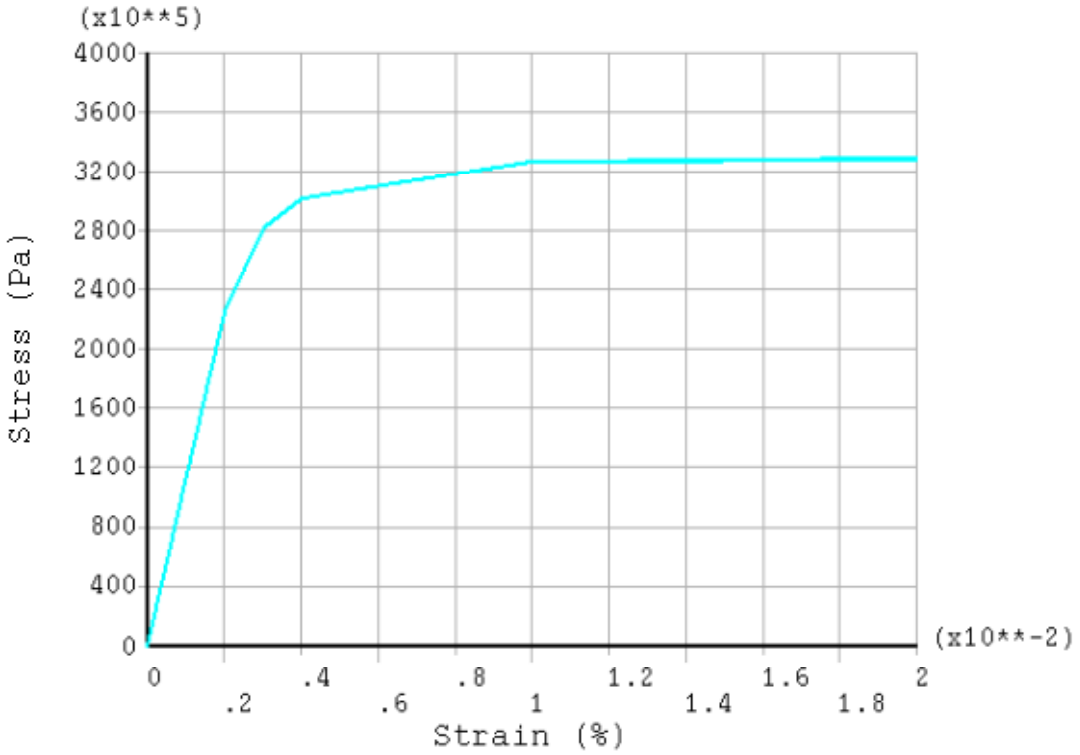

Figure 6.5: Stress-strain curve of GLIDCOP as it was implemented into the FEM model. Elastic-plastic behavior of material was experimentally measured.

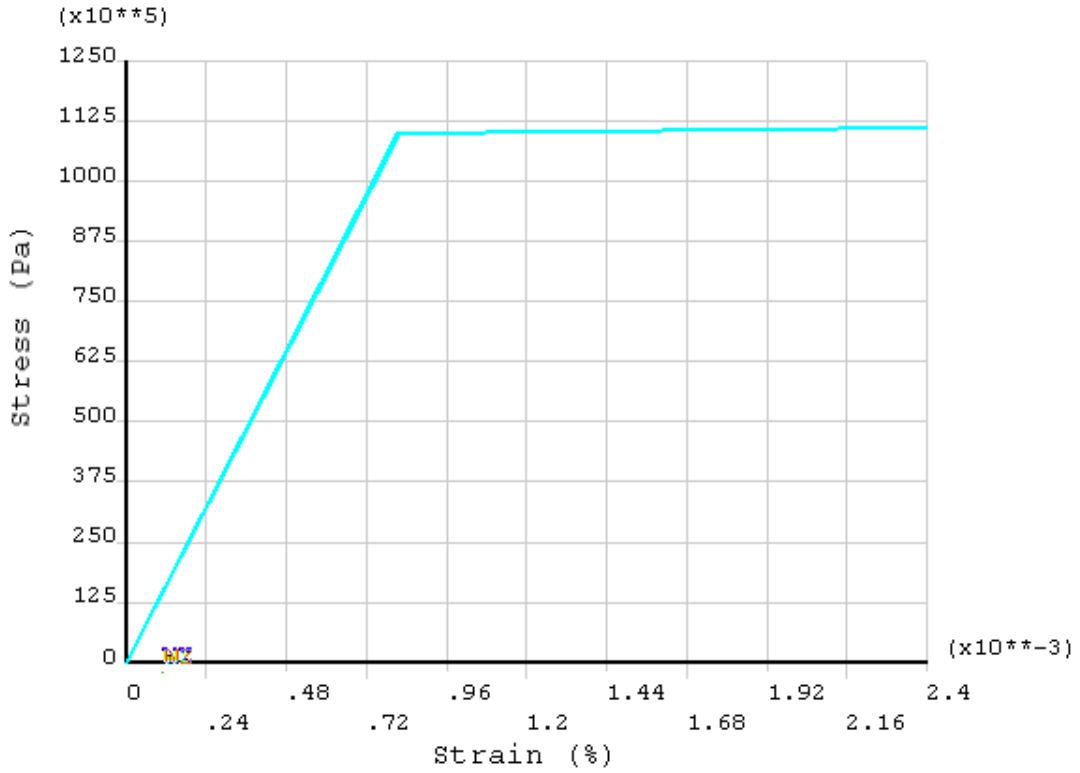

Figure 6.6: Stress-strain curve of Cu-Ni as it was implemented into the FEM model (simplified bi-linear kinematic hardening model. Data provided by material supplier.

6.3.2 Transient thermal analysis

The first step of solution is a transient thermal analysis: given the energy rate map it is possible to calculate temperature distribution and its evolution over time. This model was built using eight-node brick finite elements with only temperature degree of freedom.

Thermal boundary conditions include convection on internal surface of cooling pipes (same value as used for steady-state analysis) and thermal fluxes between component interfaces.

Thermal fluxes were calculated considering an average value of thermal conductance: as already explained, thermal conduction can be ignored on the short time-scale, thus thermal fluxes at contact interfaces are negligible (see Figure 6.7) and no coupling between thermal and structural problems should be taken into account.

Eq. 6.9 written in matrix form, show thermal problem that must be solved.

$$[C_{thermal}]\{\dot{T}\}+[k_{thermal}]\{T\}=\{Q_{heatgen}\}+\{Q_{convection}\}+\{Q_{flux}\} \qquad \text{Eq. 6.8}$$

Table 6.2 includes load step sequence used for thermal analysis; temperature evolution was simulated until 120 ms according to the typical response time of the structure (20 ms) in order to catch all dynamic phenomena.

Figure 6.8 and Figure 6.9 show temperature distribution at the end of energy deposition 7.2 μs and after 60 ms.

Table 6.2: Load step sequence used for FEM thermal analysis.

Load step number	Time at the end of load step [ms]	Integration time step Δt [μs]	Heat load
1	$7.2\cdot10^{-3}$	1	450GeV Injection Error
2	0.1	2.5	-
3	2	20	-
4	20	200	-
5	60	500	-
6	120	500	-

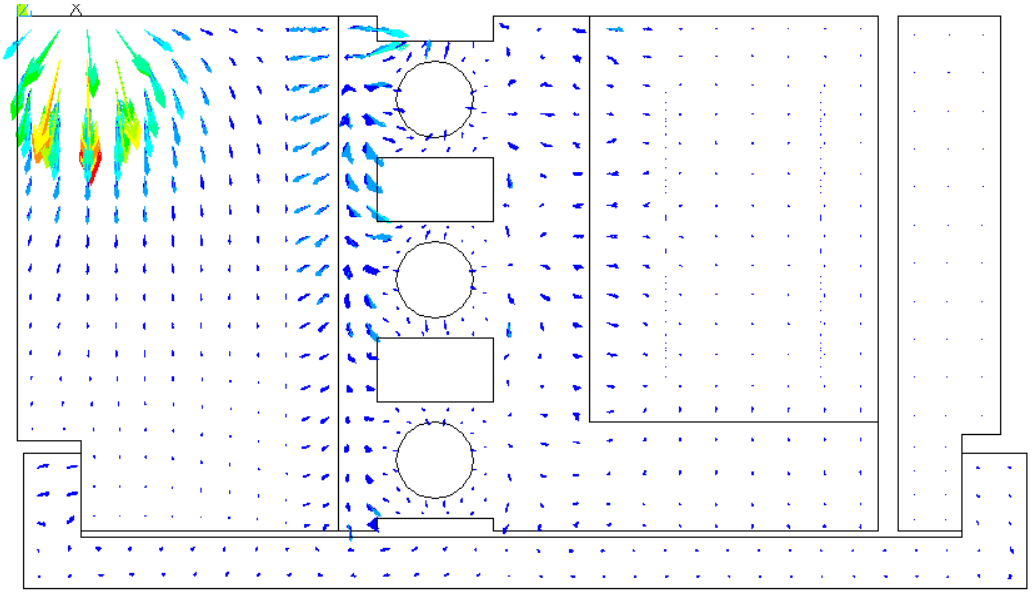

Figure 6.7: Visualization of thermal fluxes inside the collimator jaw assembly relative to thermal analysis for beam impact accident case.

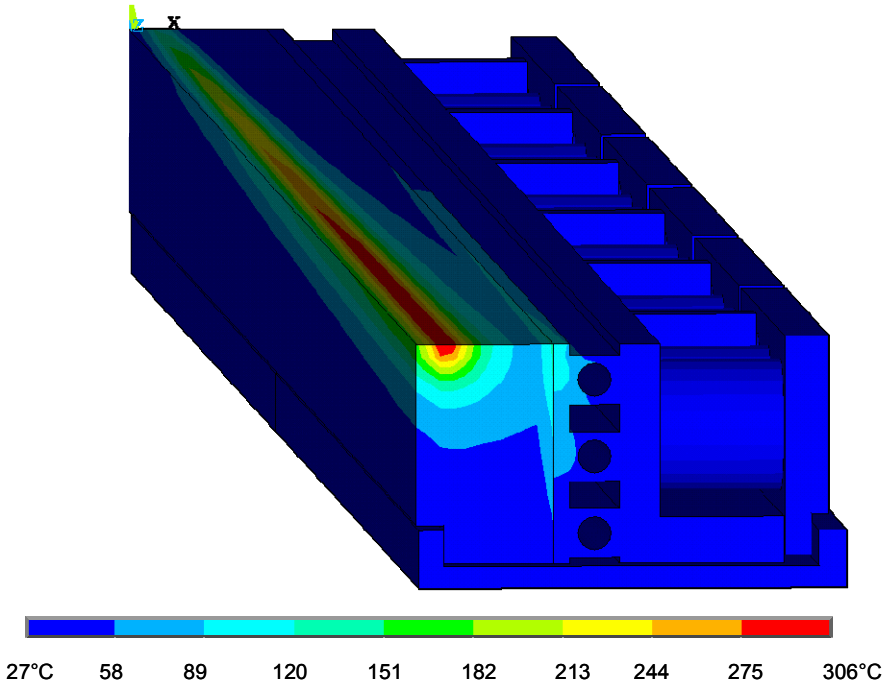

Figure 6.8: Temperature distribution provoked by beam impact at 7.2 μs.

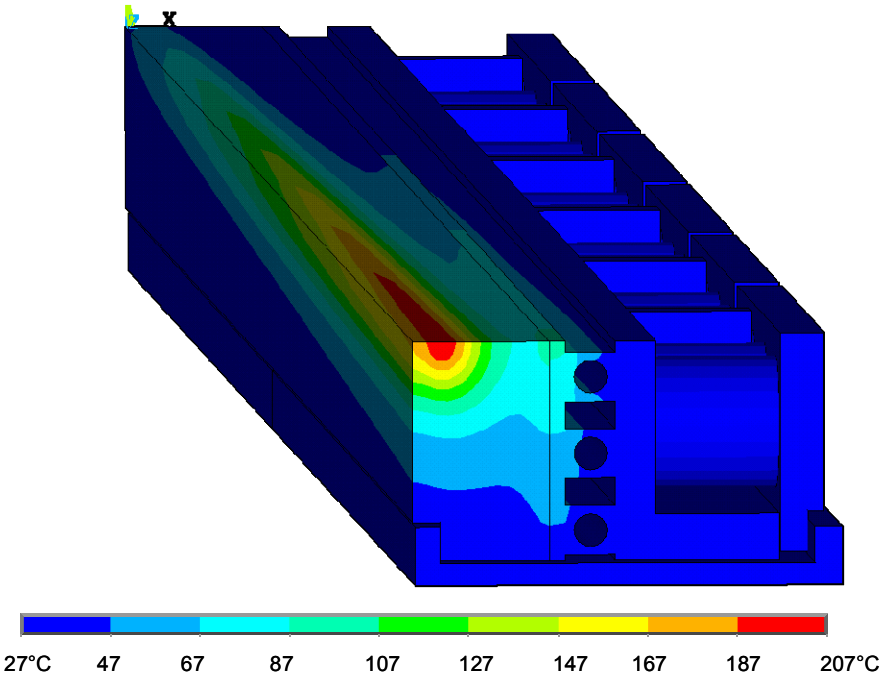

Figure 6.9: Temperature distribution provoked by beam impact at 60 ms.

6.3.3 Dynamic structural analysis

Dynamic structural analysis was performed using a model made up of eight-node brick finite elements including only displacement *dof*.

The same geometry and mesh employed for thermal analysis have been used so that temperature distribution as a function of time, obtained from thermal analysis, could be applied as nodal load at different time steps to the structural calculation. Eq. 6.9, written in matrix form, shows the structural problem that should be solved. Collimator jaw assembly is simply supported at its extremities, furthermore the effect of internal pressure on cooling pipes was considered; contact interfaces were modeled as it was described in previous chapter but no thermal fluxes are taken into account in the structural analysis.

Integration time steps and mesh size have been carefully chosen on the base of the preliminary analytical estimation: rapid temperature increase provokes dynamic response of the structure in terms of longitudinal and flexural vibrations as well as propagation of thermal stress waves. Frequency range of these phenomena starts from about 50 Hz (first period of flexural oscillation of the jaw assembly) up to 35 kHz (higher modes of longitudinal and transverse vibrations).

This wide range of interest entails that simulation should have a duration of the order of 100 ms compared with an integration time step of the order of 1 μs so that all the phenomena could be correctly caught.

Integration time step also depends on the mesh size as shown in Eq. 6.10 that represents the Courant criterion (see [6.5]) for the solution of structural dynamic problems; minimum time step was fixed to 0.1 μs.

The simulation was solved with a sequence of several load steps as indicated in Table 6.3; in order to avoid an excessive CPU time of calculation the integration time step was progressively incremented so that higher frequency phenomena are correctly caught on the very short time-scale.

$$[M]\{\ddot{u}\}+[K]\{u\}=\{F_{pressure}\}+\{F_{thermal}\} \qquad \text{Eq. 6.9}$$

$$\Delta t \le \frac{0.9 \cdot L_{mesh}}{c} \qquad \text{Eq. 6.10}$$

Table 6.3: Load step sequence used for FEM dynamic structural analysis.

Load step number	Time at the end of load step [ms]	Integration time step Δt [μs]	**Thermal load**: nodal temperature extracted from results of thermal analysis at different time [ms]
1	$7.2 \cdot 10^{-3}$	0.1	$7.2 \cdot 10^{-3}$
2	0.1	0.25	0.1
3	2	0.5	2
4	20	1	20
5	60	1	60
6	120	1	120

6.3.4 Quasi-static structural analysis

Study of thermo-mechanical effects provoked by particle beam impacts includes also the evaluation of potential permanent deformation of the hit structure once dynamic response of the system is vanished. This last step of calculation was performed using the same FEM model described in previous paragraph: equilibrium between plastic deformations (obtained from dynamic structural analysis) and elastic forces was simply calculated solving a quasi-static structural problem.

6.4 Simulation results

Two different models have been used for simulations: one has the contact plate (part of the cooling system) made up of OFE Copper, the other includes a plate made up of GLIDCOP. This comparative analysis showed similar behavior in terms of dynamic structural response but different performance concerning residual plastic deformation of the jaw assembly. In fact OFE Copper has a lower elastic limit (about 50 MPa) compared to the one of GLIDCOP (see Figure 6.5).

Results of the simulations were confirmed by experimental tests as it will be shown in next paragraph 6.5.

6.4.1 Dynamic structural response

Numerical results presented in this section were obtained with a FEM model that includes GLIDCOP contact plate. Dynamic response of the collimator jaw assembly was calculated: thermally induced vibrations and thermal stress waves were observed.

As discussed in the second part of this dissertation, in case of particle beam impact, temperature increases accordingly to the rapid energy deposition; thermal expansion is prevented by the inertia of the hit body and dynamic structural response occurs.

Following the same approach used for the analytical solution, we may consider the effect of temperature distribution shown in Figure 6.8, as two equivalent dynamic thermal loads (axial force and bending moment). This interpretation helps to explain longitudinal and flexural vibrations as well as dynamic thermal stresses obtained from FEM analysis.

Analytical predictions have been confirmed by FEM calculations: the jaw assembly, hit by high energy particle beam, shows a dynamic flexural response with a main frequency of about 45 Hz (see Figure 6.10). Thermal stresses on carbon-carbon jaw stay within the limit of the material; a pick of stress of 25 MPa can be observed in correspondence to the maximum of flexural oscillation as shown in Figure 6.10.

Higher stresses can be found on metallic support: as shown in Figure 6.8 there is a temperature increase of about 70 °C on the contact plate, this leads to dynamic longitudinal stresses up to 140 MPa. Figure 6.11 shows dynamic stresses on GLIDCOP plate; the stress remains within the range limit of the material.

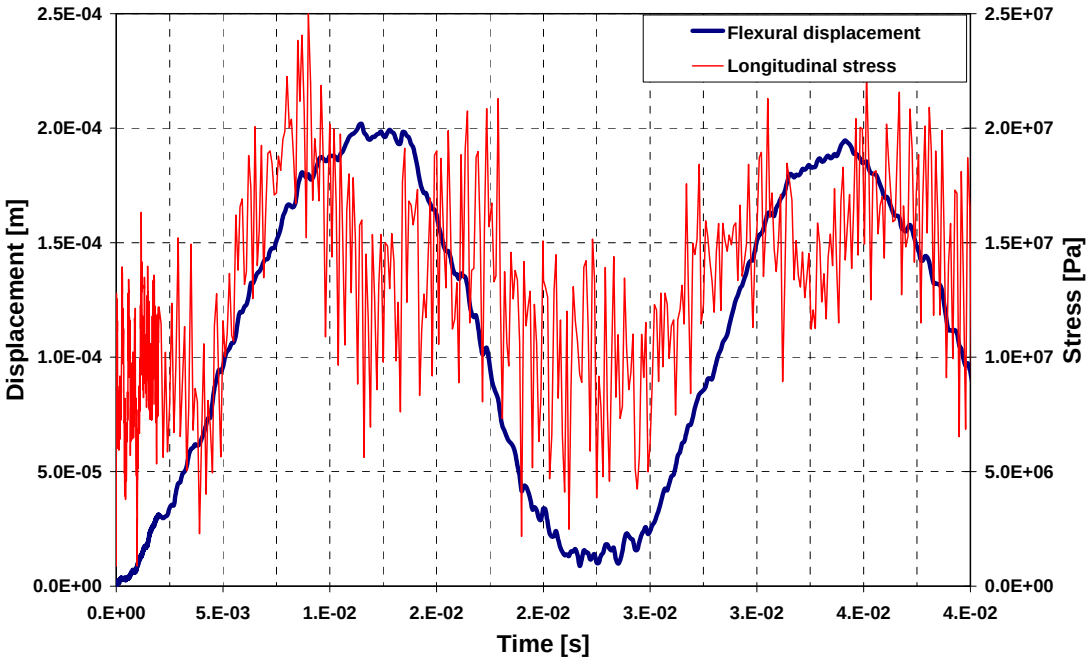

Figure 6.10: Dynamic flexural displacement and dynamic longitudinal stress detected on collimator jaw at z=650mm.

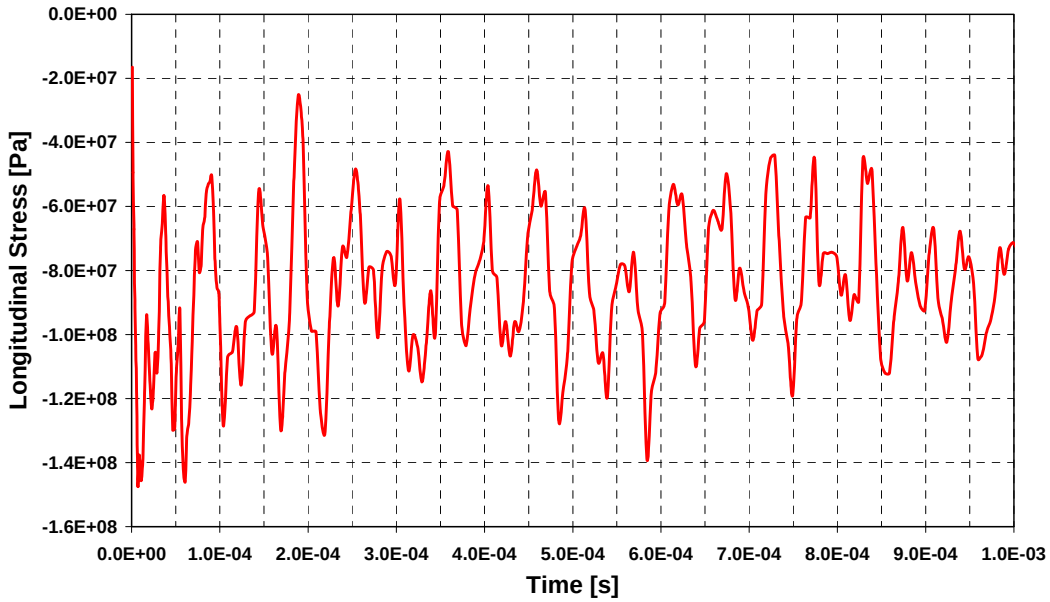

Figure 6.11: Dynamic longitudinal stress detected on GLIDCOP contact plate at z=900mm.

6.4.2 Permanent deformation

Simulation results obtained with the two models having the contact plate made up of different materials (OFE Copper and GLIDCOP) are compared in this section.

Plastic strains due to dynamic longitudinal stresses were found on the metallic support of the collimator jaw assembly. OFE Copper has a low elastic limit and a wide region of permanent deformations was detected on the contact plate as shown in Figure 6.12. Better results were obtained using GLIDCOP; in this case no plastic strains are found on the contact plate and permanent deformation is limited to a small region on the cooling pipes (see Figure 6.13).

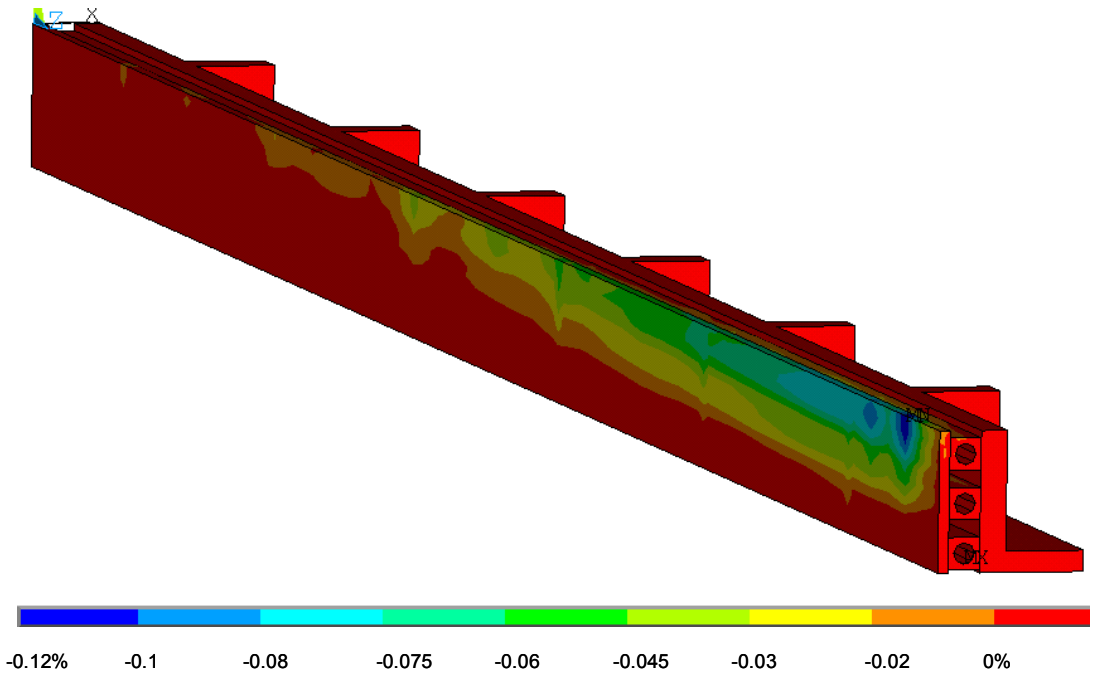

Figure 6.12: Plastic longitudinal strains on OFE copper contact plate due to particle beam impact. Results of FEM simulation.

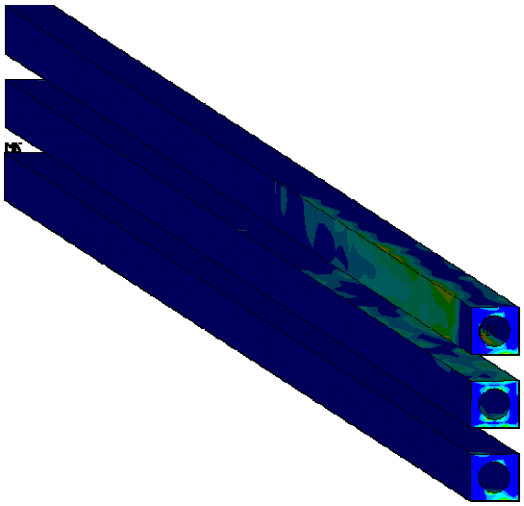

Figure 6.13: Equivalent plastic strains on Cu-Ni cooling pipes after beam impact (GLIDCOP contact plate). Results of FEM simulation.

Compressive residual strains on contact plate or cooling pipes are eccentric with respect to the neutral axis of the metal support; this leads to a permanent deflection of the collimator jaw assembly.

Figure 6.14 shows permanent deformation of the metallic support in case of OFE Copper contact plate; this result states that the collimator looses its functionality after the particle beam collision. In fact, permanent deflection of the order of 350 μm does not respect specification requirements in terms of geometrical stability (maximum acceptable deflection is about 40 μm as explained in chapter four).

FEM model including GLIDCOP plate shows better results; residual plastic strains were detected on a limited region and permanent deflection of collimator jaw assembly stays within acceptable values. As it is shown in Figure 6.15 and Figure 6.16 an high geometric stability is maintained: permanent deflection after beam impact is about 15 μm.

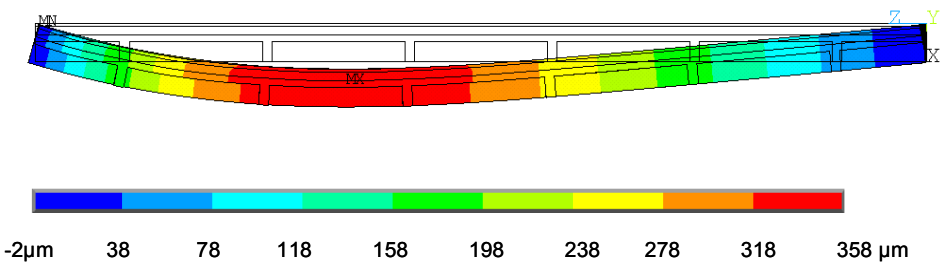

Figure 6.14: Permanent deflection of metallic support after beam impact (OFE copper contact plate). Results of FEM simulation

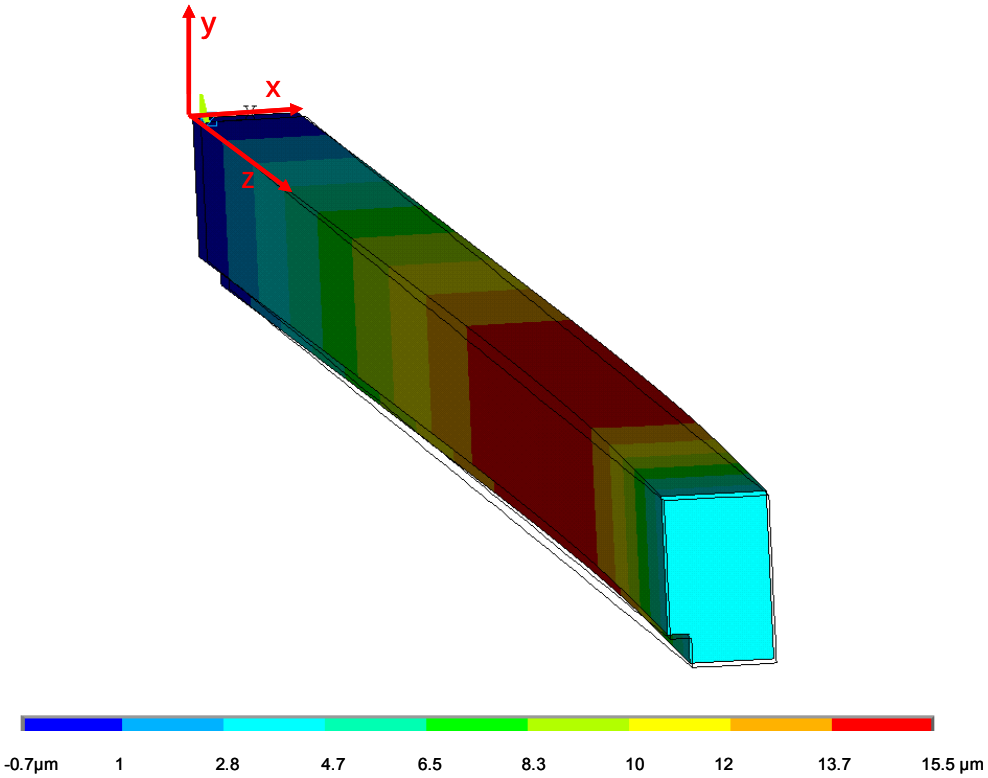

Figure 6.15: Permanent deflection of collimation jaw after beam impact (GLIDCOP contact plate). Results of FEM simulation.

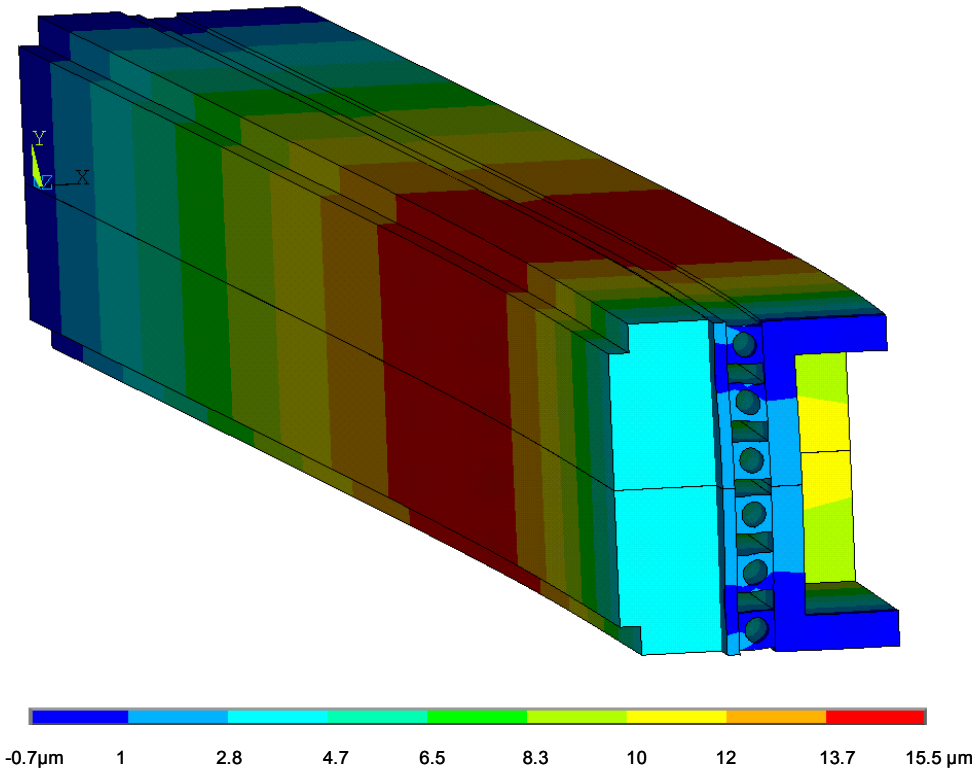

Figure 6.16: Permanent deflection of collimator jaw assembly after beam impact (GLIDCOP contact plate). Results of FEM simulation.

6.5 Experimental validation

Two experimental tests were performed at CERN: the first using a prototype of the LHC collimator, the second using an LHC collimator coming from series production. The main difference between the two structures is the material of contact plate, OFE Copper for the prototype and GLIDCOP for jaw assembly coming from series production.

In both tests the collimators were installed in the SPS ring (as explained in [6.6]) and submitted to several beam impacts (Injection Error Accident case) in order to verify the robustness of the structure. No sign of mechanical damage was detected on the carbon-carbon jaws after the tests (see Figure 6.17); this means that thermal stresses provoked by thermal shock remained within the strength limit of the material. Jaw flatness was unaffected in both tests performed thus confirming the results obtained from FEM calculations.

Accurate measurements were performed on the jaw assemblies as described in [6.7] and [6.8]. Permanent deflection of 300 μm were detected on the metallic support of the collimator prototype: this measurement is in very good agreement with the results obtained by FEM simulation (see Figure 6.14).

In the same way, the test carried out on series production collimator confirmed the numerical prediction: a very small permanent deflection of 10 μm was measured on the jaw assembly, very close to the FEM results shown in Figure 6.16.

Figure 6.17: Picture of the carbon-carbon jaw of collimator prototype taken after the robustness test. No sign of mechanical damage was detected.

The experimental equipment used to test the series production collimator included the measurements of thermally induced vibrations; this is important to obtain full validation of the numerical approach.

Following the method developed by Wilfinger [6.9], a Laser Doppler Vibrometer (LDV) was installed in the SPS ring to catch dynamic structural response provoked by particle beam impacts.

LDV was placed orthogonally to the collimation jaw surface in order to measure transverse velocity of the jaw assembly; velocity signal can be integrated thus obtaining flexural vibrations. A scheme of the experimental setup is shown in Figure 6.18.

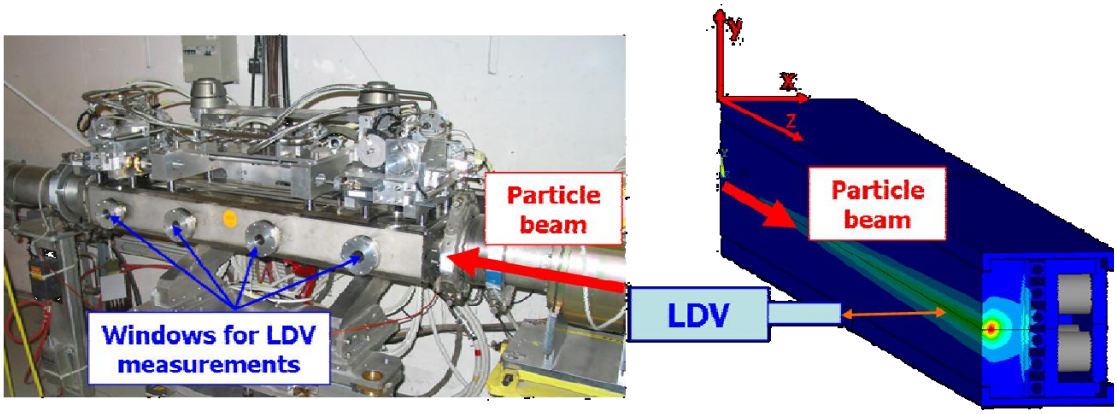

Figure 6.18: On the left side there is a picture of the LHC collimator tank equipped with four windows through which the velocity signal on the surface of the carbon-carbon jaw can be captured by LDV. On the right side there is a scheme that visualizes how the experimental setup was used in order to catch thermally induced flexural vibrations.

Comparison between experimental measurements and FEM results is shown in Figure 6.19: the main frequency of flexural oscillation is quite correctly predicted by numerical simulation while a certain difference is found in the amplitude of the dynamic response.

This is mainly due to the fact that no internal damping of materials was considered into the FEM model. Another potential source of error can be also attributed to the uncertainty in the definition of friction coefficients between contact surfaces; this have a certain influence on the dynamic response of a multi-component clamped structure like the collimator jaw assembly.

Furthermore, the energy deposition map obtained with FLUKA, is always affected by a certain error.

As it was showed in Chapter 3, dynamic deflection provoked by particle beam impact is two times larger than the static one; we can see in Figure 6.19 that the jaw assembly vibrates around its quasi-static deflected position.

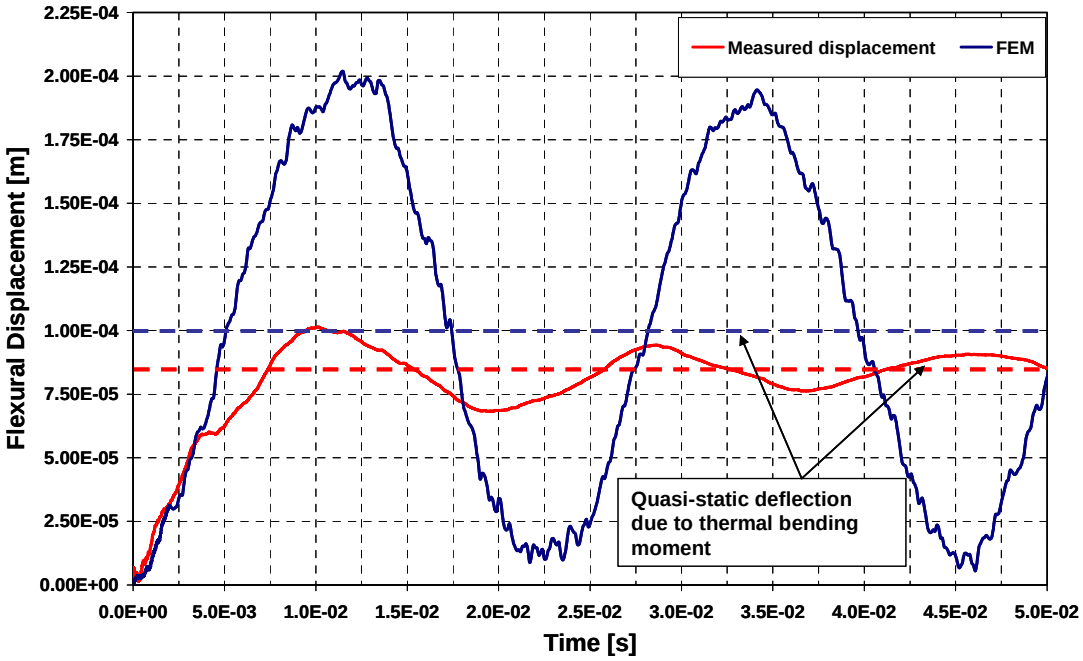

Figure 6.19: Dynamic flexural displacement of collimation jaw at z=650mm. Comparison between FEM simulation and experimental measurements.

6.6 Summary

Thermo-mechanical phenomena induced by rapid energy deposition have been studied with Finite Element Method.

Numerical approach developed allows the analysis of complex structure and multi-component system with contact interfaces within the elastic-plastic domain of materials.

Proved that thermal and structural problems can be solved separately, the analysis was organized according to three sequential steps: transient thermal analysis and dynamic structural analysis. Once thermally induced vibration and dynamic thermal

stresses had been calculated, a final static structural analysis was performed in order to catch possible permanent deformation of the structure. This aspect is very important when it is necessary to evaluate permanent damage provoked by thermal shocks.

This approach was successfully applied to the study of LHC collimators in case of abnormal beam losses. Moreover, collimator jaw assemblies were experimentally tested to verify their robustness in case of particle beam impacts. Numerical results obtained with FEM simulations, and experimental measurements are in good agreement. This confirmed the validity of the numerical approach with which reliable and accurate results can be obtained.

6.7 Nomenclature

$[K]$	Structural stiffness matrix
$[M]$	Mass matrixc
$\{u\}$	Displacement dof vector
$\{\ddot{u}\}$	Second derivative of displacement dof vector
$\{F_{pressure}\}$	Pressure nodal load vector
$\{F_{thermal}\}$	Thermal strain nodal load vector
$[C_{thermal}]$	Thermal specific heat matrix
$[k_{thermal}]$	Thermal conductivity matrix
$\{T\}$	Temperature dof vector
$\{\dot{T}\}$	Time derivative of temperature dof vector
$\{Q_{heatgen}\}$	Heat generation rate nodal load vector
$\{Q_{convection}\}$	Convection nodal load vector
$\{Q_{flux}\}$	Heat flux nodal load vector

K	Thermal conductivity
ρ	Mass density
c_p	Specific heat
$\kappa = \frac{K}{\rho \cdot c_p}$	Thermal diffusivity
α	Thermal expansion coefficient
E	Young modulus
υ	Poisson's ratio
l	Typical dimension of the structure
$\tau_{diff} = \frac{l^2}{\kappa}$	Thermal diffusion time referred to a typical dimension
t_{flex}	First period of flexural vibration
τ	Duration of energy deposition
$W(x, y, z)$	Energy rate distribution
T_{ref}	Reference temperature
σ_z	Longitudinal stress
L_{mesh}	Typical mesh size
$c = \sqrt{\frac{E}{\rho}}$	Speed of sound in a given material

References

[6.1] ANSYS User's Manual for Revision 11.0, Swanson Analysis System Inc., Houston..

[6.2] V. Vlachoudis et al: Energy Deposition Studies for the Betatron Cleaning Insertion. Proceedings of the Particle Accelerator Conference PAC05, Knoxville, 2005.

[6.3] M. Magistris, M. Santana-Leitner, Private Communications, CERN, 2005.

[6.4] Owen, R. J., Prakash, A., and Zienkiewicz, O. C., "Finite Element Analysis of Non-Linear Composite Materials by Use of Overlay Sytems", Computers and Structures, Pergamon Press, Vol. 4, pp. 1251-1267, 1974.

[6.5] R. Courant, K. Friedrichs and H. Lewy, On the partial difference equations of mathematical physics, IBM Journal, pp. 215-234, 1967.

[6.6] R. Assmann, LHC Collimation: Design and Results from Prototyping and Beam Tests, PAC05 Knoxville, 2005.

[6.7] O. Aberle, LHC Flatness of collimator (TT40) after robustness test at the SPS, Proceedings of the Collimation Working Group, 12th September 2005, CERN, Geneva.

[6.8] R. Chamizo et al., TT40 collimator – Deformation measurement after beam test, Proceedings of the Workshop on Materials for Collimators and Beam Absorbers, CERN, Geneva, 2007.

[6.9] R. Wilfinger, Proton-Induced Thermal Stress-wave Measurements for ISOLDE and CNGS, PhD Thesis, Vienna University of Technology, Atominstitut of the Austrian Universities, Vienna, and CERN, Geneva, 2005.

[6.10] H. Richter, Private Communications, CERN, Geneva, 2007.

Chapter 7

Conclusions

Recent advances in high-energy particle physics require particle accelerators reaching unprecedented energies. In particular, the Large Hadron Collider at the European Organization for Nuclear Research, stores 360 MJ for each of the two circulating beams, extending the present state of the art by 2-3 orders of magnitude. A tiny fraction of this energy is sufficient to cause destructive damages to sensitive components. Therefore, the design of accelerator equipments is strongly influenced by thermo-mechanical issues.

This research work focuses on thermo-structural effects induced in solids by high energy particle beams with the aim of providing reliable methods to be profitably used for the design of accelerator devices. Main results of the thesis can be summarized as follows:

- The problem of rapid internal heating of beam-like structures, was completely solved with an analytical approach. The proposed method allows to quickly evaluate temperature field, quasi-static and dynamic thermal stresses as well as thermally induce vibrations provoked by particle beam impacts. Comparison with experimental measurements confirmed the validity of the analytical solutions and proved the accuracy of the results obtained.
- The complex phenomenon of thermally induced vibrations was synthetically described in terms of fundamental parameters: duration of the energy deposition, characteristic thermal response time and characteristic structural response time. It was demonstrated that, once these quantities identified, the type of structural response of the system can be preliminary estimated. This gives a clear advantage for the design of structures submitted to particle beam impacts.

- In order to extend the study to systems with more complex geometry, a numerical approach based on the Finite Element Method was defined. Analytical solutions were used as a benchmark to qualify numerical tools and to identify their limit of applicability: commercial code ANSYS was found compliant with the scope of the work.
- Several FEM models have been studied, leading to a systematic approach to thermo-mechanical problems. Particular attention was paid to multi-component systems with contact interfaces: a dedicated thermo-mechanical contact algorithm was implemented for the case of steady-state and slow transient energy deposition. The study of thermally induced vibrations, treated numerically, was extended to the material elastic-plastic domain; in this way potential permanent deformations provoked by particle beam impacts were evaluated.
- FEM approach found direct application for the thermo-mechanical analysis of the LHC collimators. Experimental validation of numerical methods was successfully completed thus confirming the reliability and the accuracy of the models developed.

Future works that could extend the applicability of the methods presented in this thesis, should focus on the simulation of thermo-mechanical phenomena involving material phase-change (melting and vaporization), shock waves and deformations at high strain-rate provoked by particle beam impacts in particular conditions. In this case thermal stresses cannot be assessed applying the equations of thermo-elastoplasticity. Material models should be defined via an equation-of-state providing the relation between the deposited energy, the specific volume and the increase of pressure. This type of problems could be faced using hydrodynamic explicit codes that include Arbitrary Lagrangian-Eulerian (ALE) formulation as well as Smoothed Particle Hydrodynamics solver (SPH).